Dissertation zur Erlangung des Doktorgrades
der Fakultät für Mathematik und Physik
der Albert-Ludwigs-Universität Freiburg im Breisgau

Numerical Simulations of Granular Flow and Filling

Claas Sven Bierwisch

27. April 2009

Dekan:	Prof. Dr. Kay Königsmann
Erstgutachter:	Prof. Dr. Michael Moseler
Zweitgutachter:	Prof. Dr. Christian Elsässer
Tag der Disputation:	27. April 2009

Peer-reviewed publications concerning the contents of this thesis:

- C. Bierwisch, T. Kraft, H. Riedel, and M. Moseler. Three-dimensional discrete element models for the granular statics and dynamics of powders in cavity filling. *Journal of the Mechanics and Physics of Solids*, 57:10–31, 2009.

- C. Bierwisch, T. Kraft, H. Riedel, and M. Moseler. Die filling optimization via three-dimensional discrete element modeling. *Submitted to Powder Technology.*

- C. Bierwisch and M. Moseler. Compressible kinematic modeling of granular flow. *Manuscript in preparation.*

Patents concerning the contents of this thesis:

- C. Bierwisch, T. Kraft, H. Riedel, and M. Moseler. Verfahren zur Homogenisierung einer Pulverschüttung bei der Herstellung von Pulverpresslingen. *Pending patent application.*

Conference proceeding papers concerning the contents of this thesis:

- C. Bierwisch, B. Henrich, T. Kraft, M. Moseler, and H. Riedel. 3D-Modelling of die filling. In *Proceedings of the EURO PM 2005, Volume 3, Prague, Czech Republic*, pages 331–337, Shrewsbury, UK, 2005. European Powder Metallurgy Association.

- C. Bierwisch, T. Kraft, H. Riedel, and M. Moseler. Predicting density distributions in die filling. In *Proceedings of the EURO PM 2007, Volume 3, Toulouse, France*, pages 305–310, Shrewsbury, UK, 2007. European Powder Metallurgy Association.

- H. Riedel, A. Wonisch, C. Bierwisch, T. Kraft, and M. Moseler. Simulationen von Prozessfolgen mit der Diskrete-Elemente-Methode. In H. Kolaska, editor. *Pulvermetallurgie — Kompetenz und Perspektive*, pages 153–175, Düsseldorf, Germany, 2007. VDI-Gesellschaft Werkstofftechnik.

- C. Bierwisch, T. Kraft, M. Moseler, and H. Riedel. Simulation of die filling in 3D with special emphasis on vibration supported filling. In *Advances in powder metallurgy & particulate materials 2008, Part 1*, pages 130–138, Princeton, USA, 2008. Metal Powder Industries Federation.

- C. Bierwisch, B. Weber, R. Kübler, M. Moseler, and G. Kleer. Contact regimes in the wire sawing process: Explicit 3D modeling of PEG/SiC slurry. In *Proceedings of 23rd European Photovoltaic Solar Energy Conference, Valencia, Spain*, pages 1104–1108, Munich, Germany, 2008. WIP-Renewable Energies.

- T. Kraft, C. Bierwisch, and H. Riedel. New advances in modeling powder metallurgical processing steps. In L. S. Sigl, P. Rödhammer, and H. Wildner, editors. *Proceedings of the 17th Plansee Seminar 2009*, Reutte, Austria, 2009. Plansee Group.

Conference talks concerning the contents of this thesis:

- C. Bierwisch, B. Henrich, and M. Moseler. Particle methods in powder technology. *The second Russian-German Advanced Research Workshop on Computational Science and High Performance Computing*, Stuttgart, Germany, March 14–16, 2005.

- C. Bierwisch, T. Kraft, M. Moseler, and H. Riedel. 3D-Modeling of Powder Flow and Application to Gravity Die Filling. *DPG Spring Meeting of the Condensed Matter Division*, Dresden, Germany, March 26–31, 2006.

- C. Bierwisch, T. Kraft, M. Moseler, and H. Riedel. Static-dynamic transitions: Role of grain shape and coarse graining. *DPG Spring Meeting of the Condensed Matter Division*, Regensburg, Germany, March 26–30, 2007.

- C. Bierwisch and M. Moseler. Grain coarsening effects in granular statics and dynamics. *DPG Spring Meeting of the Condensed Matter Division*, Berlin, Germany, February 25–29, 2008.

Contents

How do we know that the creations of worlds
are not determined by falling grains of sand?

Victor Hugo — Les Miserables

Abstract

Flow and filling behavior of granular matter was investigated within the framework of the discrete element method (DEM) in this work. The large number of individual grains in many systems prevents a one-to-one mapping between experiments and numerical simulations even on parallel computing clusters. Based on the conservation of local energy density a novel coarse graining scheme was developed which allows for the representation of a given system using artificially enlarged grains. Thereby, a dimensional analysis yielded scaling rules for the DEM force laws.

In comparison with experiments, grain models of different mechanical and morphological complexity were assessed with respect to their ability to reproduce and predict statical properties (angle of repose) as well as dynamical properties (flow rates, filling behavior) of an iron powder. It was found that an adequate modeling of the grain shape is of particular importance in addition to the consideration of inter-granular friction and cohesion.

A reliable grain model was used to analyze kinematics of hopper discharge (compare Fig. 0.1) and density inhomogeneities in cavity filling (compare Fig. 0.2). An existing continuum model for the velocity field inside a hopper was improved by taking the influence of the local volume fraction into account. Another contribution to the theoretical description of granular matter was made by deriving an analytic expression for the mass discharge through a slit orifice from a moving shoe. Process variations for cavity filling were developed which yield a considerable homogenization of the density distribution.

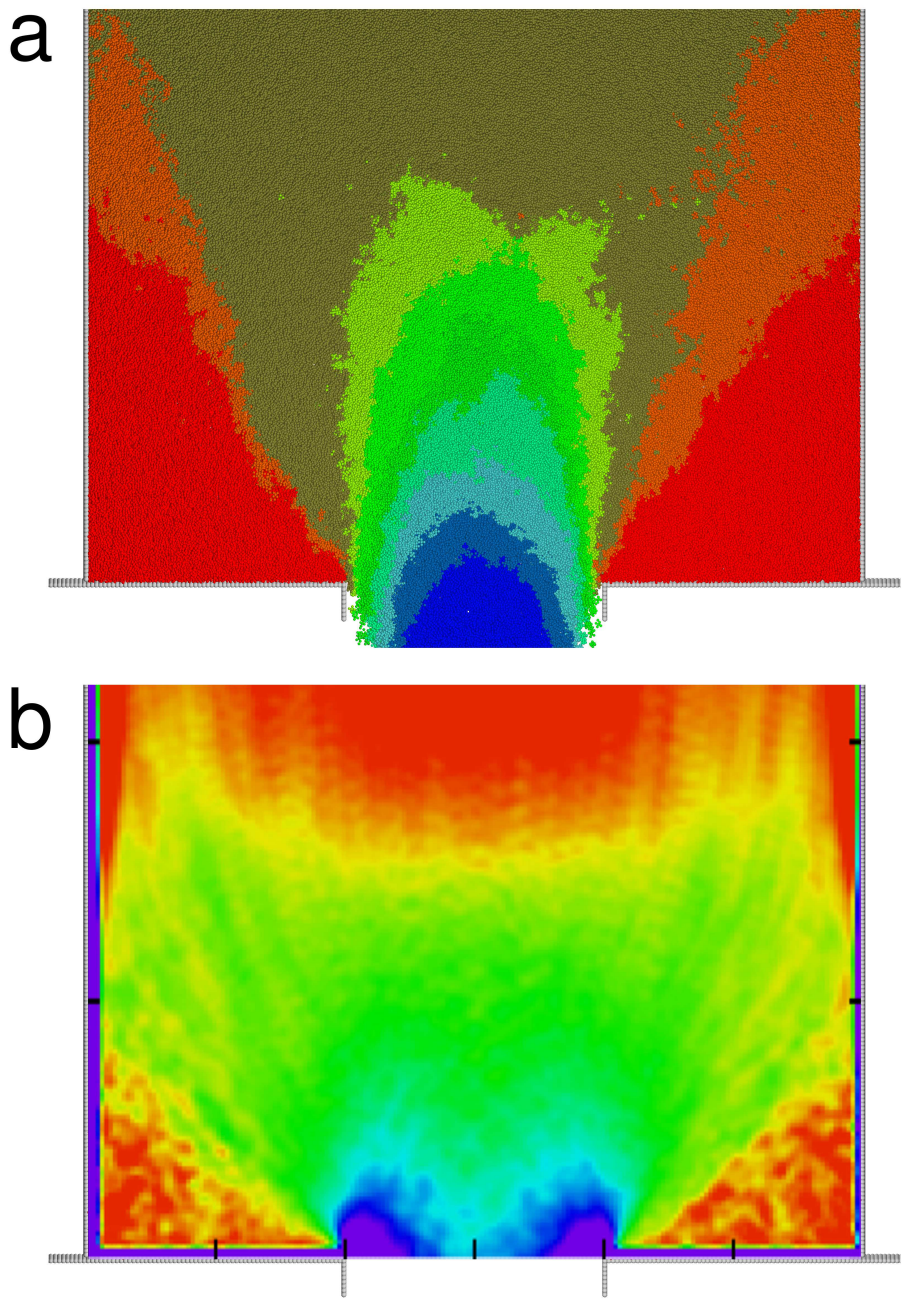

Figure 0.1: DEM simulation of granular discharge from a hopper. (a): Color coded snapshot of velocity magnitude where blue means fast and red means slow; (b): color coded averaged volume fraction where blue means dilute and red means dense. The discovery of a relationship between these two quantities is presented in Chapter 5.

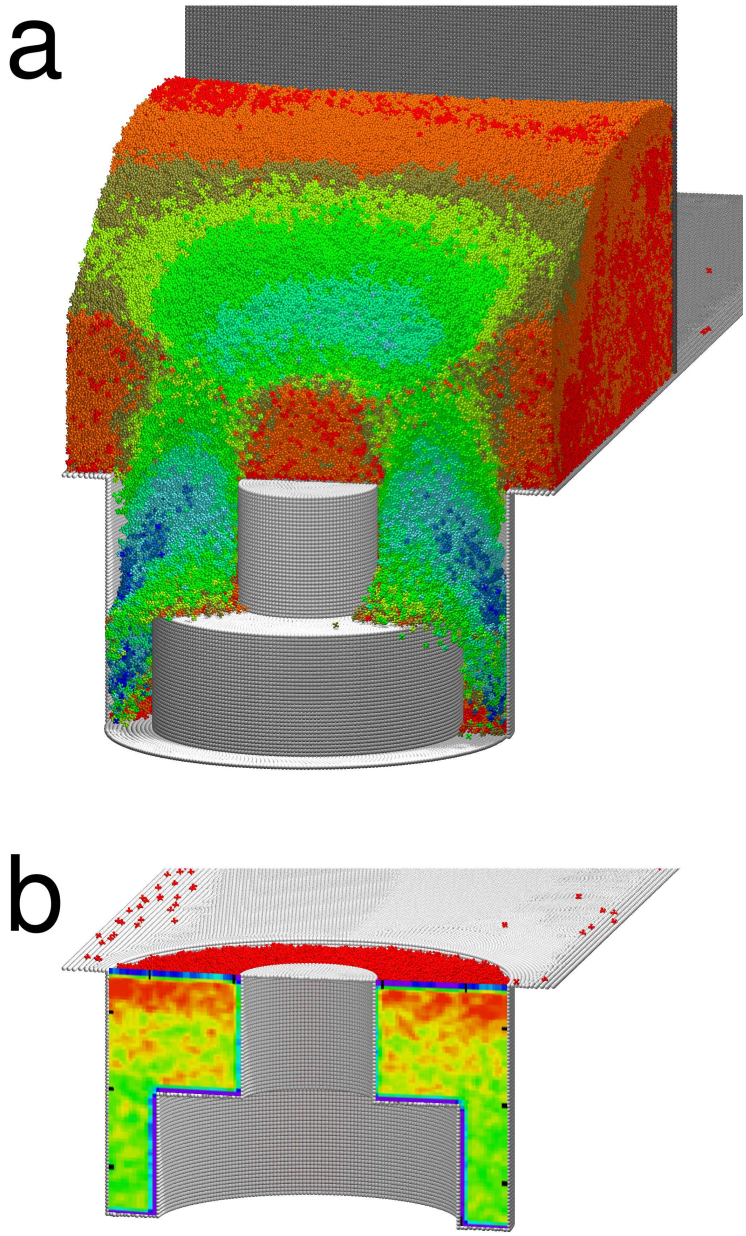

Figure 0.2: DEM simulation of cavity filling using a feeding shoe. (a): Snapshot of the filling process; (b): final density distribution. Parts of the cavity and the shoe are not displayed for clarity. Color coding is same as in Fig. 0.1. The influence of shoe movement and other process parameters on the density distribution is investigated in Chapter 6.

Kurzzusammenfassung

In dieser Arbeit wurden Fließ- und Füllvorgänge granularer Medien mit der Diskrete-Elemente-Methode (DEM) numerisch untersucht. Die Anzahl der einzelnen Körner ist in vielen granularen Systemen so enorm groß, dass eine Eins-zu-eins-Abbildung zwischen Experiment und numerischer Simulation selbst auf parallelen Rechenclustern derzeit nicht möglich ist. Basierend auf der Erhaltung der lokalen Energiedichte wurde ein neuartiges *coarse graining*-Schema entwickelt, welches die Darstellung eines gegebenen Systems unter Verwendung künstlich vergrößerter Körner erlaubt. Eine Dimensionsanalyse führte dabei auf Skalierungsregeln für die DEM-Kraftgesetze.

Im Vergleich mit Experimenten wurden Kornmodelle unterschiedlicher mechanischer und morphologischer Komplexität hinsichtlich ihrer Fähigkeit zur Reproduktion bzw. Vorhersage sowohl statischer Eigenschaften (Böschungswinkel) als auch dynamischer Eigenschaften (Flussraten, Füllverhalten) eines Eisenpulvers untersucht. Hierbei zeigte sich, dass neben der Abbildung inter-granularer Reibung und Kohäsion insbesondere eine adäquate Modellierung der Kornform erforderlich ist.

Ein belastbares Kornmodell wurde zur Analyse der Kinematik des Siloausflusses (vgl. Abb. 0.1) sowie von Dichteinhomogenitäten beim Matrizenfüllen (vgl. Abb. 0.2) verwendet. Für den Siloausfluss wurde ein bestehendes Kontinuumsmodell für das Geschwindigkeitsfeld unter Berücksichtigung des Einflusses des lokalen granularen Volumenanteils erweitert und dadurch in seiner Präzision verbessert. Ein weiterer Beitrag zur theoretischen Beschreibung granularer Materie wurde durch die Herleitung eines analytischen Ausdrucks für den Massenfluss durch eine Schlitzblende aus einem bewegten Container geleistet. Für das Matrizenfüllen wurden Variationen in der Prozessführung erarbeitet, die zu einer deutlichen Homogenisierung der Dichteverteilung führen.

1 Introduction

Granular matter is ubiquitous [1]. A common pantry contains several granular products, e.g. flour, mixed herbs, cereal, nuts, maybe a pile of oranges. The food industry is concerned with packing, mixing or segregation, and transportation of such goods [2, 3]. Pharmaceutical agents are often produced as powders which are compacted into tablets [4]. Difficulties in the handling of bulk goods motivated studies on the optimal design of hoppers and silos [5, 6]. Powder metallurgy exceeds traditional casting in the cost-efficient mass production of geometrically complex parts [7, 8]. Shot peening is used to modify mechanical properties of metal surfaces via plastic deformations [9]. Wafers are separated from a silicon ingot by wire sawing using a slurry with abrasive grains [10].

The term *granular matter* denominates particulate materials with grain diameters larger than $1\,\mu$m [11]. Thus, Brownian motion is negligible. Characteristic interaction properties of grains are the inelasticity of collisions and static friction [12, 13]. The forms of appearance of granular matter resemble the three classical states of aggregation. A bed of silica grains in a sandbox can support large weights placed upon. Yet, in an hourglass the same material seems to flow like a liquid. A granular gas emerges if a container filled with these grains is agitated by vertical vibrations with an acceleration amplitude larger than the acceleration of gravity.

The differences between granular and traditional states of aggregation become clear upon closer examination. Unlike using a solid state body, it is not possible to build a freestanding block out of pourable granular matter. In fact, a heap with a material-specific maximum angle of repose will form [14]. The support of a weight in a sandbox is realized due to the formation of a force chain network among the grains [15]. Thereby, the load is transmitted to the surrounding walls. The volume fraction of a granular bulk is strongly dependent on its formation history. A fine-grained, cohesive material can have a porosity of more than 80% when piled up carefully [16]. Via tapping [17] or compaction under external load [18, 19] the volume fraction can be increased substantially.

If an hourglass was filled with a liquid, the markings would have to be redrawn. A fluid obeys Torricelli's law: The mass flow rate at the bottleneck would decrease continuously. In contrast, Beverloo found a constant mass flow rate when analyzing granular hopper outflow [20]. The stress exerted on the grains is also independent of the filling level upon reaching a threshold value. The weight of additional grains is transferred from the granular force chains via friction onto the walls [21].

Owing the dissipative collisions, a granular gas would eventually come to rest without external agitation. Furthermore, the energy scale $k_{\mathrm{B}}T$ is irrelevant for the system and classical thermodynamics cannot be applied for a description [12].

A comprehensive theoretical framework for the description of granular matter is not found yet. However, experimentally verified formalisms exist for certain regimes: Quasistatic plastic deformations in compacted granular materials can be described in a continuum picture using an appropriate yield criterion [22, 23]. The velocity field of grains rapidly flowing down an inclined plane can be calculated by incorporating a recently discovered constitutive law [24, 25] into the Navier-Stokes equations. A statistical approach to granular packings explains how vibrations shift a system through its phase space [26, 27, 28]. Thereby, energy is replaced by volume and ordinary temperature by the newly introduced compactivity of the material. This list is not exhaustive.

Powder metallurgical part production provides a motivation of this thesis. The standard processing route consists of three steps [29, 7]. It starts with the filling of the die (a cavity with the negative shape of the part): the powder is poured from a reservoir hopper through a hose into a moveable container (feeding shoe) and then the shoe passes the die one or more times thereby delivering powder into it (compare Fig. 0.2). This first step is followed by uniaxial compaction with punches resulting in a so-called green body with a very brittle consistency. The green body is ejected from the cavity and placed in a furnace for the final sintering step: thermal activation below the melting point leads to the formation and growth of necks between adjacent grains and eventually to a fully dense structure [30]. Generally, the filling of the die and the subsequent compaction lead to inhomogeneous distributions of the powder in the green body [31, 32]. Inhomogeneous green densities[1] lead to inhomogeneous shrinkage during sintering and therefore to distortions of the sintered part. Thus, it is desirable to identify mechanisms leading to density inhomogeneities during the cavity filling step [33]. This knowledge can then be used to improve the overall filling homogeneity by appropriate process parameter adjustment. The objectives of fill density prediction and homogenization as well as the discovery of universal laws of powder flow and filling behavior establish goals of the present study. In this regard a numerical approach is beneficial in two ways. First, density information is accessible at the grain scale and any temporal resolution. Second, variations of process parameters can be tested and analyzed with comparably little effort.

The particulate nature of powders suggests to use a particle based method for a numerical description. Especially for the investigation of flow phenomena with large rearrangements and of transitions between static and dynamic regimes no alternatives exist due to the lack of appropriate continuum models. Hence, the *time-*

[1] In this work the term *density* is used instead of *volume fraction* in the context of powder technological processes because of its widespread usage within the community.

driven discrete element method (DEM) is employed which describes the motion of an ensemble of particles by time integration of Newton's equations of motion. The particles interact via explicitly defined force laws and they can be affected by external forces such as gravity. A detailed illustration of the method is given in Chapter 2. Pioneering work on the description of powders and grains using this approach was done by Cundall [34], Campbell [35], Walton [36], Haff [37], and Herrmann [38]. DEM is currently developing into a versatile simulation method for particulate materials such as rocks, sand, and powders [39].

Generally, one real world grain is represented by one DEM grain. Powder metallurgical parts have typical dimensions in the range of centimeters. Thus, they are formed by large numbers of grains ranging from 10^7–10^8 for 100 μm diameter to 10^{13}–10^{14} when using fine powders with a diameter of 1 μm. Current computer clusters allow for DEM simulations of up to 10^8 particles. However, using 10^6 particles is rather reasonable for an extensive parameter space exploration. This gap can be bridged by using a *coarse graining* approach, i.e. the investigation of a given system at a coarsened resolution. In other words, degrees of freedom are neglected below a certain scale. In the present case, the term coarse graining is to be taken literally: The grain diameters in the simulations are scaled up with respect to the real world grain size. Of course, meaningful coarse grained simulations require that all system properties of interest are unaffected by the scaling. In Chapter 3 a coarse graining scheme for DEM simulations is derived. It is based on the conservation of energy density in granular collisions. Tests in various setups validate the applicability of the scheme.

The identification and adjustment of an appropriate DEM grain model for granular simulations of static and dynamic regimes are presented in Chapter 4. Benchmarking experiments are conducted using an industrial powder with irregular shaped grains. Spherical models are often used in simulations for the sake of numerical simplicity. Yet, several studies point out the importance of an adequate description of the grain morphology due to its influence on heap shapes [40], flow properties [41], and packing density [42]. This work opposes spherical to complex shaped grain models with regard to their ability of describing both flow rates through an orifice and the angle of repose of a real powder. The model calibration is thereby carried out via adjustment of suitable DEM force law parameters. Similarities and differences of the models are highlighted by analyzing velocity distributions and volume fractions. The predictive power of each model is evaluated in a cavity filling setup. A model with pronounced non-spherical morphology is identified to represent the real powder best.

Improvements of theoretical models for granular outflow are exposed in Chapter 5. First, the velocity field within a discharging hopper is studied using DEM simulations (compare Fig. 0.1). A common, though not very accurate, continuum approach to describe the velocity field is given by *kinematic modeling* [43]. This method is refined by considering volume fraction variations within the flowing ma-

terial. A relationship between the volume fraction and the coupling of horizontal and vertical velocity component is identified. Considerable increase in accuracy is demonstrated by using this relationship in the proposed *compressible* kinematic modeling. Second, an analytic expression for granular mass flow from a moving shoe through a slit orifice is derived and validated in simulations and experiments. This equation is based on a transient generalization of Beverloo's law for hopper discharge.

A thorough numerical analysis of cavity filling by means of a feeding shoe is presented in Chapter 6. The simulations utilize a coarsened, complex shaped grain model thereby making use of aforementioned findings of this work. The quality of the numerical description is assessed via comparisons with experimentally measured density distributions [31]. Good agreement between simulation and experiment allows for further investigations revealing origins of density inhomogeneities. Based upon these insights recommendations for density homogenization are derived and successfully tested.

The usefulness of granular simulations for regenerative energy generation is demonstrated in Appendix A. The costs of photovoltaic electricity production need to decrease in order to achieve grid parity, i.e. equal costs of electric energy from alternative and conventional sources. Thus, there is a strong demand for lowered production costs of solar panels, which can be met by an increased yield of wafers per silicon ingot. The wire sawing process for wafer separation is investigated with regard to this requirement. The abrasive slurry is thereby modeled via coupling a DEM grain representation with a particle based fluid description, namely dissipative particle dynamics [44].

2 Numerical methods

The granular simulations in this thesis were carried out using the *time-driven* discrete element method, which is described in Section 2.1. Continuous fields like velocity profiles or volume fraction distributions were obtained from DEM simulations by a tessellation and averaging method as introduced in Section 2.2.

2.1 Discrete element method

From a technical point of view, DEM simulations are essentially the same as molecular dynamics (MD) simulations [45, 46]. Yet, the term DEM was established within the engineering community and later also among physicists if macroscopic grains instead of microscopic molecules are modeled.

Newton's equations of motion,

$$m_i \, \dot{\mathbf{v}}_i = \mathbf{f}_i, \quad \dot{\mathbf{r}}_i = \mathbf{v}_i, \tag{2.1a}$$

$$\underline{I_i} \, \dot{\boldsymbol{\omega}}_i = \mathbf{t}_i, \tag{2.1b}$$

have to be solved for an ensemble $i = 1, \ldots, N$ of N particles with masses m_i, center of mass positions $\mathbf{r}_i$, velocities $\mathbf{v}_i$, inertia tensors $\underline{I_i}$, angular velocities $\boldsymbol{\omega}_i$, forces $\mathbf{f}_i$, and torques $\mathbf{t}_i$. This is achieved by explicit time integration using a velocity Verlet scheme [45] with fixed timestep Δt,

$$\mathbf{r}_i(t + \Delta t) = \mathbf{r}_i(t) + \mathbf{v}_i(t)\Delta t + \frac{\mathbf{f}_i(t)\Delta t^2}{2\, m_i}, \tag{2.2a}$$

$$\mathbf{v}_i(t + \Delta t) = \mathbf{v}_i(t) + \frac{(\mathbf{f}_i(t) + \mathbf{f}_i(t + \Delta t))\, \Delta t}{2\, m_i}, \tag{2.2b}$$

$$\boldsymbol{\omega}_i(t + \Delta t) = \boldsymbol{\omega}_i(t) + \frac{\underline{I_i}^{-1} \, (\mathbf{t}_i(t) + \mathbf{t}_i(t + \Delta t))\, \Delta t}{2}. \tag{2.2c}$$

An alternative particle based approach, namely the *event-driven* discrete element method [47], is not suitable for the scope of this work. The latter scheme uses an adaptive integration timestep which becomes infinitely small when describing static granular ensembles [48]. From now on the term DEM is used synonymously with *time-driven* DEM.

Grain interactions were limited to contact forces for the scope of this work. The forces describe four basic collision mechanisms: repulsion, cohesion, damping, and

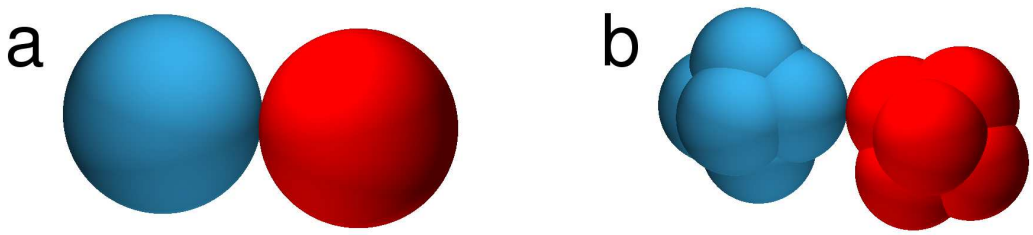

Figure 2.1: Contact of grains each consisting of (a) just a single sphere or (b) an agglomerate of spheres.

friction. These properties are characteristic for granular collisions in general although the relative importance of each one depends on the actual system setup and the used material. Long-range interactions which play a role for electrostatically charged or magnetic grains were not considered. Overviews of DEM force schemes are given in Refs. [49, 50, 51, 52].

In the most simple case spheres were used to approximate the grain geometry (see Fig. 2.1a). Irregular shape was taken into account by rigidly connecting spheres to form composed grains (see Fig. 2.1b). Granular models of different physical and morphological complexity were used. Their common force laws will be described first. The differences are introduced in detail in the following paragraphs.

2.1.1 Force Laws

The deformation of two spherical particles i and j is described by the difference between the sum of their radii and the distance of their centers, $h_{ij} = R_i + R_j - |\mathbf{r}_{ij}|, \mathbf{r}_{ij} = \mathbf{r}_i - \mathbf{r}_j$. Exclusively, contact forces are used, which means that they are only applied on the particles if $h_{ij} > 0$.

Repulsion

Normal to the contact area of touching spheres acts an elastic force as introduced by Hertz [53],

$$\mathbf{f}_{ij}^{\mathrm{e}} = \left(\frac{2}{3} \tilde{E} \sqrt{R_{\mathrm{eff}}} h_{ij}^{3/2} \right) \hat{\mathbf{r}}_{ij}. \tag{2.3}$$

$\tilde{E} = E/(1-\nu^2)$, where E is Young's modulus and ν is Poisson's ratio. $R_{\mathrm{eff}} = R_i R_j/(R_i + R_j)$ is an effective particle radius and $\hat{\mathbf{r}}_{ij} = \mathbf{r}_{ij}/|\mathbf{r}_{ij}|$ is the normal vector of the contact plane.

Cohesion

Cohesion is included using the Johnson-Kendall-Roberts (JKR) model [54], which extends the Hertzian contact law by introducing the work of adhesion per unit contact area w (the surface energy is $w/2$),

$$\mathbf{f}_{ij}^{\mathrm{coh}} = -\left(\sqrt{4\pi w \tilde{E}}\, R_{\mathrm{eff}}^{3/4} h_{ij}^{3/4}\right) \hat{\mathbf{r}}_{ij}. \tag{2.4}$$

Besides Van der Waals forces, cohesion can be caused by powder additives, e.g. lubricants or binders, or by air humidity. The JKR model is used here to represent the influence of various cohesive effects in a simplified way. Thus, the quantity w should be interpreted as a generalized cohesive energy per unit contact area.

The minimum of the combined repulsive and cohesive force is

$$\left(\mathbf{f}_{ij}^{\mathrm{e}} + \mathbf{f}_{ij}^{\mathrm{coh}}\right)\left(h_{ij}^{\min}\right) = -\frac{3}{2}\pi w R_{\mathrm{eff}} \hat{\mathbf{r}}_{ij}, \quad h_{ij}^{\min} = \left(\frac{9}{4}\pi \frac{w}{\tilde{E}} \sqrt{R_{\mathrm{eff}}}\right)^{2/3}. \tag{2.5}$$

A negative external load with an absolute magnitude larger than $3\pi w R_{\mathrm{eff}}/2$ will separate the spheres. The cohesive contact is modelled symmetric for loading and unloading, i.e. decohesion occurs at $h_{ij} = 0$.

Powders used in this work have grain diameters of around $100\,\mu$m. Van der Waals forces become negligible already at significantly smaller separation distances [55]. Thus, modeling cohesion as pure contact force is a reasonable approximation.

Dissipation

Collisions of grains are inelastic in most cases [56]. On the one hand, kinetic energy is absorbed due to viscous or plastic deformations of the grains. On the other hand, kinetic energy is lost due to sound production. The inelasticity of particle collisions is described by means of a viscous normal force [57],

$$\mathbf{f}_{ij}^{\mathrm{v}} = -\left(\gamma_{\mathrm{n}} \sqrt{R_{\mathrm{eff}}\, h_{ij}}\, (\mathbf{v}_i - \mathbf{v}_j) \cdot \hat{\mathbf{r}}_{ij}\right) \hat{\mathbf{r}}_{ij}, \tag{2.6}$$

where γ_{n} is an empirical damping parameter with the physical unit of a viscosity.

Friction

Static and sliding friction are described in a tangential spring scheme as introduced by Cundall *et al.* [34]. When two particles collide, an imaginary spring is attached to the initial contact points. During the finite collision time the elongation $\boldsymbol{\xi}_{ij}$ of the spring is tracked and a force is applied at each contact point in the direction

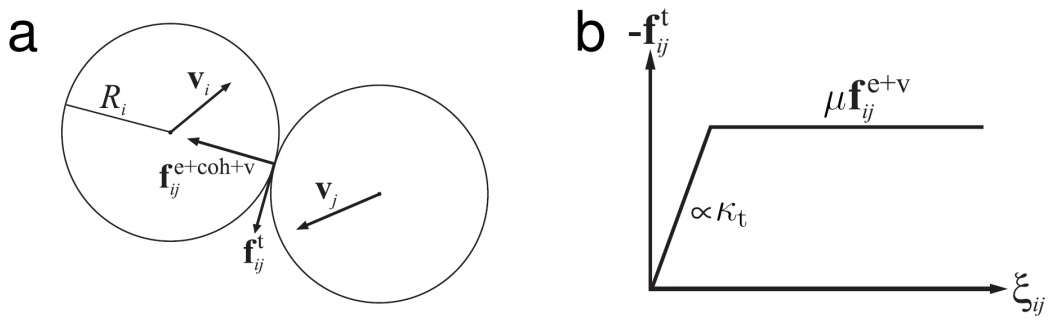

Figure 2.2: (a): Contact forces between two particles. (b): Tangential force law for Coulomb friction.

of the spring. The magnitude of this force is limited by the product of the current normal force at the contact and a Coulomb like friction coefficient μ,

$$\mathbf{f}_{ij}^{\mathrm{t}} = -\min\left[\kappa_{\mathrm{t}}\sqrt{\frac{h_{ij}}{R_{\mathrm{eff}}}}\left|\boldsymbol{\xi}_{ij}\right|, \mu\left|\mathbf{f}_{ij}^{\mathrm{e}}+\mathbf{f}_{ij}^{\mathrm{v}}\right|\right]\boldsymbol{\xi}_{ij}/\left|\boldsymbol{\xi}_{ij}\right|, \tag{2.7}$$

where κ_{t} is a tangential spring constant. A schematic overview of two particles in contact including the corresponding forces is given in Fig. 2.2a and the frictional force law is depicted in Fig. 2.2b.

Non-contact forces

In addition to the contact forces, gravitational acceleration g in z-direction (unit vector $\hat{\mathbf{z}}$),

$$\mathbf{f}_i^{\mathrm{grav}} = -m_i\, g\, \hat{\mathbf{z}}, \tag{2.8}$$

and Stokes damping due to air viscosity μ_{a},

$$\mathbf{f}_i^{\mathrm{stokes}} = -6\pi\mu_{\mathrm{a}} R_i \mathbf{v}_i. \tag{2.9}$$

are taken into account. Note that for typical grain velocities in the studied flow regimes (i.e. up to 1 m/s) the influence of air drag is extremely small compared to all other forces.

2.1.2 Non-rotational spheres

A basic model to describe a granular medium consists just of spheres without rotational degrees of freedom. The forces as described in Section 2.1.1 act on the centres of mass while torques are neglected. Although this may seem to be unphysical, both, realistic flow and static phenomena like finite angles of repose, can be reproduced by this basic model as shown in Chapter 4.

2.1.3 Rolling spheres

When introducing rotational degrees of freedom to the particles, changes of their angular velocity occur due to the canonical torque that results from the tangential forces

$$\mathbf{t}_{ij}^{\mathrm{t}} = R_i \, \mathbf{f}_{ij}^{\mathrm{t}} \times \hat{\mathbf{r}}_{ij}. \tag{2.10}$$

Spherical particles then cannot form stable angles of repose any longer and behave fluid-like in that sense, because no torques exist which oppose their rotational movement. However, static behavior can be restored to some extent by incorporating a Coulomb-like rolling friction torque [58],

$$\mathbf{t}_{ij}^{\mathrm{r}} = -\mu_{\mathrm{r}} \left| \mathbf{f}_{ij}^{\mathrm{e}} + \mathbf{f}_{ij}^{\mathrm{v}} \right| \boldsymbol{\omega}_i / \left| \boldsymbol{\omega}_i \right|, \tag{2.11}$$

with rolling friction coefficient μ_{r}. The rolling friction torque restrains even minimal rolling movement of a sphere proportional to the normal force at each contact and is oriented antiparallel to the particle's angular velocity. This torque stabilizes a granular heap considerably. However note that this dynamic rolling friction torque still allows for significant long-term relaxations (see Section 4.1.4). Thus, a stable equilibrium granular heap can only be achieved by a corresponding static rolling friction torque, a concept which was not considered further in the present work.

2.1.4 Complex grains

Even without employing rolling friction concepts it is possible to reproduce static heaps by using complex shaped particles consisting of an agglomerate of spheres (or circles in two dimensions [40]). Figure 2.1b shows two geometrically complex grains in contact. In order to investigate the influence of grain shape a rigid body motion solver [59] was implemented. Each rigid body with label k consists of a set of spheres with labels $i \in S_k$. The mass of a rigid body k is given by $m_k = \sum_{i \in S_k} m_i$ and its three principal moments of inertia are $I_{k,x}$, $I_{k,y}$ and $I_{k,z}$. The principal axes of the rigid body form a coordinate system which will be referred to as body frame in contrast to the fixed laboratory frame. The center of mass positions and velocities in the laboratory frame are denoted by $\mathbf{r}_k$ and $\mathbf{v}_k$, respectively. The rotation of the rigid body within the laboratory frame is represented by a quaternion $\mathbf{q}_k = (\xi_k, \eta_k, \zeta_k, \chi_k)$. The components of $\mathbf{q}_k$ are related to the Euler angles of

rotation, θ_k, ϕ_k and ψ_k [60] by

$$\xi_k = \sin\left(\frac{\theta_k}{2}\right)\sin\left(\frac{\psi_k - \phi_k}{2}\right), \tag{2.12a}$$

$$\eta_k = \sin\left(\frac{\theta_k}{2}\right)\cos\left(\frac{\psi_k - \phi_k}{2}\right), \tag{2.12b}$$

$$\zeta_k = \cos\left(\frac{\theta_k}{2}\right)\sin\left(\frac{\psi_k + \phi_k}{2}\right), \tag{2.12c}$$

$$\chi_k = \cos\left(\frac{\theta_k}{2}\right)\cos\left(\frac{\psi_k + \phi_k}{2}\right), \tag{2.12d}$$

which implies the constraint $\mathbf{q}_k^2 = 1$ [61]. The angular velocity of the rigid body is given by $\boldsymbol{\omega}_k$ in the laboratory frame and by $\boldsymbol{\Omega}_k = (\Omega_{k,x}, \Omega_{k,y}, \Omega_{k,z})$ in the body frame. The rotation matrix,

$$A_k(\mathbf{q}_k) = \begin{pmatrix} -\xi_k^2 + \eta_k^2 - \zeta_k^2 + \chi_k^2 & 2(\zeta_k\chi_k - \xi_k\eta_k) & 2(\eta_k\zeta_k + \xi_k\chi_k) \\ -2(\xi_k\eta_k + \zeta_k\chi_k) & \xi_k^2 - \eta_k^2 - \zeta_k^2 + \chi_k^2 & 2(\eta_k\chi_k - \xi_k\zeta_k) \\ 2(\eta_k\zeta_k - \xi_k\chi_k) & -2(\xi_k\zeta_k + \eta_k\chi_k) & -\xi_k^2 - \eta_k^2 + \zeta_k^2 + \chi_k^2 \end{pmatrix}, \tag{2.13}$$

is used for transformation between the body frame and the laboratory frame,

$$\boldsymbol{\omega}_k = A_k^{\mathrm{T}}(\mathbf{q}_k)\,\boldsymbol{\Omega}_k, \tag{2.14}$$

where A_k^{T} is the transposed of A_k. The relative positions of the centers of the spheres with respect to $\mathbf{r}_k$ are given by the vectors $\mathbf{b}_i$ in the laboratory frame and $\mathbf{B}_i$ in the body frame, $\mathbf{b}_i = A_k^{\mathrm{T}}\mathbf{B}_i$. By definition, the $\mathbf{B}_i$ are constant.

The constituent spheres of touching rigid bodies interact with each other due to the force laws described in Section 2.1.1 resulting in total forces $\mathbf{f}_i$. The force acting on the rigid body k is then given by

$$\mathbf{f}_k = \sum_{i \in S_k} \mathbf{f}_i, \tag{2.15}$$

while the according torque is

$$\mathbf{t}_k = \sum_{i \in S_k} \mathbf{b}_i \times \mathbf{f}_i \tag{2.16}$$

in the laboratory frame and

$$\mathbf{T}_k = A_k(\mathbf{q}_k)\,\mathbf{t}_k \tag{2.17}$$

in the body frame.

The time propagation of the center of mass positions and velocities is analogous to Eqs. (2.2a) and (2.2b),

$$\mathbf{r}_k(t+\Delta t) = \mathbf{r}_k(t) + \mathbf{v}_k(t)\Delta t + \frac{\mathbf{f}_k(t)\Delta t^2}{2\,m_k}, \tag{2.18a}$$

$$\mathbf{v}_k(t+\Delta t) = \mathbf{v}_k(t) + \frac{(\mathbf{f}_k(t) + \mathbf{f}_k(t+\Delta t))\,\Delta t}{2\,m_k}. \tag{2.18b}$$

The integration step for $\mathbf{q}_k$ is given by

$$\mathbf{q}_k(t+\Delta t) = \mathbf{q}_k(t) + \dot{\mathbf{q}}_k(t)\Delta t + \frac{1}{2}\ddot{\mathbf{q}}_k(t)\Delta t^2 - \lambda_k(t)\mathbf{q}_k(t)\Delta t^2, \tag{2.19}$$

where $\lambda_k(t)$ is a Lagrangian multiplier which satisfies $\mathbf{q}_k^2(t+\Delta t) = 1$,

$$\begin{aligned}\lambda_k(t) = \frac{1}{\Delta t^2}\Bigg(1 - \frac{1}{2}\dot{\mathbf{q}}_k^2(t)\Delta t^2 \\ - \sqrt{1 - \dot{\mathbf{q}}_k^2(t)\Delta t^2 - \dot{\mathbf{q}}_k(t)\cdot\ddot{\mathbf{q}}_k(t)\Delta t^3 - \frac{1}{4}(\ddot{\mathbf{q}}_k^2(t) - \dot{\mathbf{q}}_k^4(t))\Delta t^4}\Bigg).\end{aligned} \tag{2.20}$$

The first derivative of $\mathbf{q}_k$ is

$$\dot{\mathbf{q}}_k(t) = \frac{1}{2}Q(\mathbf{q}_k(t))\boldsymbol{\Omega}_k(t) \tag{2.21}$$

and the second derivative is

$$\ddot{\mathbf{q}}_k(t) = \frac{1}{2}Q(\mathbf{q}_k(t))\dot{\boldsymbol{\Omega}}_k(t) - \mathbf{q}_k(t)\dot{\mathbf{q}}_k^2(t), \tag{2.22}$$

with

$$Q\left(\mathbf{q}_k\right) = \begin{pmatrix} -\zeta_k & -\chi_k & \eta_k \\ \chi_k & -\zeta_k & -\xi_k \\ \xi_k & \eta_k & \chi_k \\ -\eta_k & \xi_k & -\zeta_k \end{pmatrix} \tag{2.23}$$

and the angular acceleration

$$\dot{\Omega}_{k,\alpha}(t) = \frac{T_{k,\alpha}(t) + (I_{k,\beta} - I_{k,\gamma})\Omega_{k,\beta}(t)\Omega_{k,\gamma}(t)}{I_{k,\alpha}} \tag{2.24}$$

where (α, β, γ) represent every cyclic permutation of (x, y, z).

The coupled Euler equations for the integration of the angular velocity are solved by an iterative scheme with iteration counter j,

$$\begin{aligned}\Omega_{k,\alpha}^{(j)}(t+\Delta t) = \Omega_{k,\alpha}(t) + \frac{\Delta t}{2I_{k,\alpha}}\Bigg(T_{k,\alpha}(t) + T_{k,\alpha}(t+\Delta t) + (I_{k,\beta} - I_{k,\gamma}) \\ \times \left(\Omega_{k,\beta}(t)\Omega_{k,\gamma}(t) + \Omega_{k,\beta}^{(j-1)}(t+\Delta t)\Omega_{k,\gamma}^{(j-1)}(t+\Delta t)\right)\Bigg).\end{aligned} \tag{2.25}$$

A useful approximation to start with is $\mathbf{\Omega}_k^{(0)}(t+\Delta t) = \mathbf{\Omega}_k(t)$ and three iterations proved to be sufficient.

The new positions and velocities of the constituent spheres are given by

$$\mathbf{r}_i(t+\Delta t) = \mathbf{r}_k(t+\Delta t) + \mathbf{b}_i(t+\Delta t), \tag{2.26a}$$
$$\mathbf{v}_i(t+\Delta t) = \mathbf{v}_k(t+\Delta t) + \boldsymbol{\omega}_k(t+\Delta t) \times \mathbf{b}_i(t+\Delta t). \tag{2.26b}$$

2.1.5 Boundary conditions

The confining geometries, i.e. cavity or container walls and the walls of a feeding shoe, are composed of overlapping spheres positioned on a grid. In this way arbitrary geometries can be defined easily or even imported from CAD programs. The typical grid spacing is about 80% of the sphere diameter. The wall particles interact with the powder particles via the same force laws acting in the powder. The only difference is that forces on wall particles are not used for their propagation, as the mass of both cavity and shoe can be considered infinite in comparison to the powder. The feeding shoe movement is defined by applying a constant displacement per time to all wall particles forming the shoe. Oscillations of feeding shoe or cavity are applied analogously.

The parameters for the powder-wall interaction are equal to those for interactions between two powder particles except for the surface energy, which has been set to zero, and the wall friction coefficient, μ_w, which replaces μ. Influences of the actual choice of μ_w and the wall sphere diameter are described in Section 4.2.4.

2.1.6 Initial conditions

To generate the starting configuration the powder particles are first put on a simple cubic lattice with lattice constants of at least 1.2 grain diameters. Every grain is displaced from its lattice node by a small random offset and given a random angular velocity. Then the simulation is started letting the particles settle under gravity (compare Fig. 2.3). This procedure was chosen in order to mimic powder transfer into the container or feeding shoe to some extend. The container orifice is opened or the shoe movement starts, respectively, after the grains have come to a rest. Alternatively an initial distribution with predefined volume fraction could be used as described in Ref. [62].

2.1.7 Summary of model parameters

Equations (2.3)–(2.11) constitute an effective medium whose properties can be adjusted by variation of the parameters R, w, μ, μ_r, $\tilde{E}$, γ_n, and κ_t. The influence of R is discussed thoroughly within the coarse graining analysis in Chapter 3. The parameters w, μ, and μ_r have a strong influence on static and dynamic properties

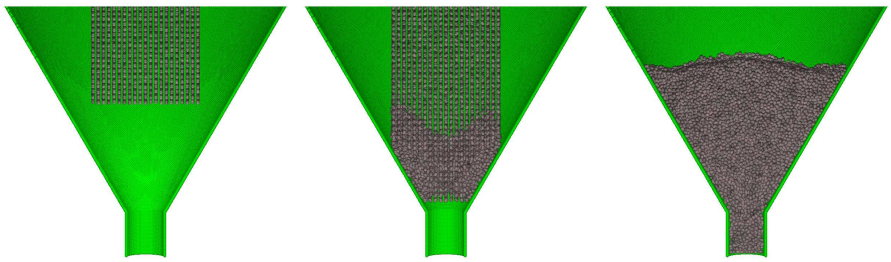

Figure 2.3: Settling of grains in a hopper under gravity.

of the effective medium and were used to model a real powder as described in Section 4.1. Effects of the actual choice of $\tilde{E}$, γ_n, and κ_t are dealt with in Section 4.2.

Simulations were carried out with four geometrically and mechanically different grain models (see Fig. 2.4): Spheres without and with rotational degrees of freedom (models A and B), composed particles consisting of six spheres positioned at the corners of an octahedron with diameters equal to the distance between the furthest corners (model C), and composed particles consisting of a central sphere and six spheres positioned at the corners of an octahedron touching the central one (model D). The sizes of the composed grains were chosen such that their volumes are equal to the volumes of the simple spheres in models A and B.

Throughout this work the following convention is used to refer to the grain size. R denotes the sphere radius for models A and B and the radius of the constituent spheres for models C and D. Let $d = 2R$ for models A and B while d represents the maximum diameter of the composed grains in models C and D (C: $d = 4R$; D: $d = 6R$).

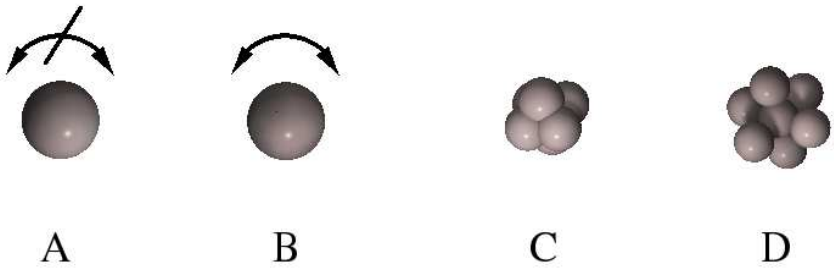

Figure 2.4: Different DEM grain types used in the simulations. Spheres without (i.e. model A) or with (model B) rotational degrees of freedom and agglomerate grains. Note, the spheres in model C have an overlap while they are non-overlapping in model D.

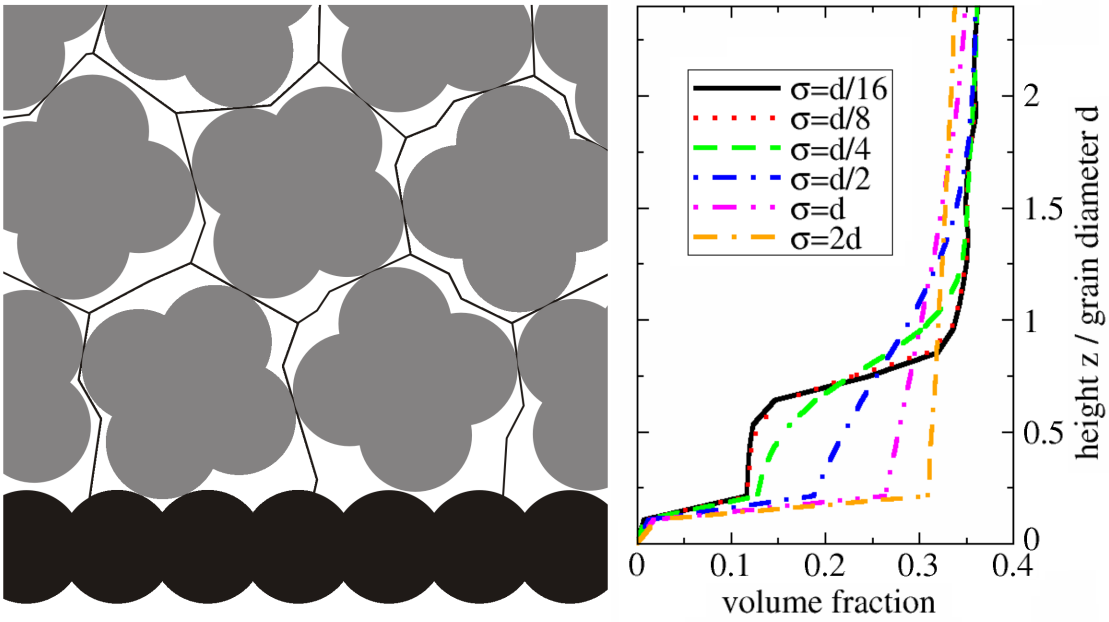

Figure 2.5: Left: Schematic of Voronoï space tessellation for volume fraction computation. Grey particles are powder grains and black particles form a wall. Straight lines separate the Voronoï cells. Note that the Voronoï cell boundaries between wall particles and grains are defined by the surface of the wall particles. Right: Calculated volume fractions for varied values of the standard deviation σ in the Gaussian weighting of local grain volume fractions. Data from a 3D simulation similar to the schematic on the left is used for the volume fraction calculation.

2.2 Volume fraction computation

Volume fraction distributions are determined in the simulations by Voronoï tessellation [63, 64, 65]. The Voronoï cell of a grain is given by the set of all points in space which are closer to that grain than to any other (see Fig. 2.5 for details). A local volume fraction at the position of a grain with label k is defined by the fraction of grain volume and Voronoï cell volume, $\rho_k = V_k/V_{\mathrm{cell},k}$. This approach was also used in a granular flow study by Rycroft *et al.* [66]. Continuous, smooth fields are derived by averaging over grain volume fractions using Gaussian distance weighting,

$$\rho(\mathbf{r}) = \frac{\sum_{k=1}^{N} \rho_k \exp\left(-\frac{(\mathbf{r}-\mathbf{r}_k)^2}{2\sigma^2}\right)}{\sum_{k=1}^{N} \exp\left(-\frac{(\mathbf{r}-\mathbf{r}_k)^2}{2\sigma^2}\right)}. \tag{2.27}$$

The effect of the choice of the standard deviation σ in relation to the grain diameter d is displayed on the right hand side of Fig. 2.5. For $\sigma/d \leq 1/4$ volume fraction variations are resolved at grain level, which is particularly important for surface and boundary phenomena. Using larger values of σ/d yield smoothing of the calculated volume fraction distribution. In order to reduce statistical variations volume fractions are averaged over several timesteps during steady state regimes if possible. Velocity distributions are obtained similar to volume fraction distributions by replacing ρ_k in Eq. (2.27) with the velocity $\mathbf{v}_k$ or its magnitude $|\mathbf{v}_k|$, respectively.

3 A coarse graining scheme for discrete element modeling

Due to limitations in computational power, the number of model grains in a DEM simulation cannot be chosen arbitrarily large. Thus, it is not yet possible to simulate any given real system on a one-to-one grain level, especially if the system has a large ratio of outer length scale to typical grain diameter. Representing a number of real grains by a single, larger model grain is a way to cope with this challenge. This chapter describes a critical inspection of such a coarse graining. The motivation for these investigations is twofold. On the one hand, it is important to assess the errors that are related with the applied coarse graining level. On the other hand, it is helpful to know whether or not even bigger model grains can be used to save computational time. Both aspects lead to the more general question under which circumstances the absolute grain size is relevant for the powder properties or if an adequate scaling of its mechanical parameters with respect to the grain diameter yields unchanged macroscopic properties. Notably, no attempts of establishing and assessing a coarse graining method for DEM simulations are found in the literature.

3.1 Force scaling

A coarse graining scheme is proposed that is based on an appropriate adjustment of the interaction laws given by Eqs. (2.3)–(2.7). The main idea is to construct an effective medium with scaled grain size which incorporates the same energy density and evolution of energy density as the original system with unscaled grains. The density of gravitational potential energy is independent of grain radius R, if solid density, ρ, and volume fraction of the grains are constant. Thus,

$$\rho = \rho' \tag{3.1}$$

is required. The prime shall from now on denote quantities in a scaled system while the quantities without prime describe the system with original grain radii. It will be shown later that volume fractions are indeed unaffected by the proposed coarse graining scheme. In order to preserve the kinetic energy density, scaling must not affect grain velocities. Gain of kinetic energy density is given due to gravitational acceleration or feeding shoe movement/acceleration. Both contributions are per se independent of grain size. Loss of kinetic energy density occurs due to inelastic

collisions between the grains. The dissipated energy in a binary collision of grains i and j with reduced mass $m_{\text{eff}} = m_i m_j/(m_i + m_j)$ is

$$\Delta E_{\text{kin}} = \frac{m_{\text{eff}}}{2}\left(\left(\dot{h}_{ij}^{\text{b}}\right)^2 - \left(\dot{h}_{ij}^{\text{a}}\right)^2\right), \tag{3.2}$$

where $\dot{h}_{ij}^{\text{b}}$ and $\dot{h}_{ij}^{\text{a}}$ are the normal components of the relative velocity before and after the collision, respectively. The number of collisions per volume and time scales with $(R/R')^3$ and the reduced mass with $(R'/R)^3$ when going from the original system into the scaled system. The energy dissipation per volume and time is then preserved, if the coefficient of restitution, i.e. the quotient of relative velocities after and before a collision, is unaffected by coarse graining.

The differential equations for normal and tangential movement during a binary collision are

$$m_{\text{eff}}\ddot{h}_{ij} = \frac{2}{3}\tilde{E}\sqrt{R_{\text{eff}}}h_{ij}^{3/2} - \sqrt{4\pi w\tilde{E}}R_{\text{eff}}^{3/4}h_{ij}^{3/4} - \gamma_{\text{n}}\sqrt{R_{\text{eff}}h_{ij}}\dot{h}_{ij} \tag{3.3a}$$

and

$$\begin{aligned} m_{\text{eff}}\ddot{\xi}_{ij} = & -\min\left[\kappa_{\text{t}}\sqrt{\frac{h_{ij}}{R_{\text{eff}}}}\left|\xi_{ij}\right|, \mu\left|\frac{2}{3}\tilde{E}\sqrt{R_{\text{eff}}}h_{ij}^{3/2} - \gamma_{\text{n}}\sqrt{R_{\text{eff}}h_{ij}}\dot{h}_{ij}\right|\right] \\ & \times \operatorname{sgn}\left(\xi_{ij}\right), \end{aligned} \tag{3.3b}$$

where rotational motion is neglected for simplicity. A dimensional analysis [67] of Eqs. (3.3a) and (3.3b) yields three dimensionless numbers,

$$\Pi_1 = \frac{w}{R_{\text{eff}}\tilde{E}}, \tag{3.4a}$$

$$\Pi_2 = \frac{\gamma_{\text{n}}}{R_{\text{eff}}\sqrt{\rho\tilde{E}}}, \tag{3.4b}$$

$$\Pi_3 = \frac{\kappa_{\text{t}}}{R_{\text{eff}}\tilde{E}}. \tag{3.4c}$$

A reference velocity can be expressed as

$$v_0 = \sqrt{\frac{\tilde{E}}{\rho}}. \tag{3.5}$$

Due to the similarity of the trajectories it is ensured that energy density dissipation rates are unaffected by coarse graining, if Π_1, Π_2, Π_3, and v_0 are kept constant.

These requirements yield in combination with Eq. (3.1) the scaling rules

$$\tilde{E} = \tilde{E}', \tag{3.6a}$$

$$\frac{w}{R_{\text{eff}}} = \frac{w'}{R'_{\text{eff}}}, \tag{3.6b}$$

$$\frac{\gamma_{\text{n}}}{R_{\text{eff}}} = \frac{\gamma'_{\text{n}}}{R'_{\text{eff}}}, \tag{3.6c}$$

$$\frac{\kappa_{\text{t}}}{R_{\text{eff}}} = \frac{\kappa'_{\text{t}}}{R'_{\text{eff}}}, \tag{3.6d}$$

and thus

$$w \propto R, \tag{3.7a}$$

$$\gamma_{\text{n}} \propto R, \tag{3.7b}$$

$$\kappa_{\text{t}} \propto R. \tag{3.7c}$$

Equations (3.7a)–(3.7c) imply that the respective forces scale with R^2 when coarse graining is applied. Note however that the dependencies of the forces on R and h_{ij} are not affected on a certain scale. Only when carrying out the same simulation with bigger (or smaller) grains, the magnitudes of the forces are adjusted in order to obtain unchanged energy densities. Thus, by scaling the forces an effective medium with larger grains is obtained that exhibits the same properties as the medium with the original grain size. This substitutional medium might have no counterpart in reality, i.e. a granular medium with such a grain size and properties might not exist. Nevertheless, it can be used to study properties of the original system with considerable less computational effort. The Stokes drag force, Eq. (2.9), can also be scaled according to the above analysis. The scaling rule for the air viscosity is $\mu_{\text{a}} \propto R$.

The scaling scheme should be distinguished from a reduction of the number of grains based on scaling down all external length scales. The latter would require a dimensional analysis of the complete system and it would be hard to obtain a definite result on how to vary all relevant scales without changing the details of granular flow or filling behavior. Of course, the scaling breaks down for effects that depend intrinsically on grain size. Therefore, this possibility must be checked for each property of interest.

The scaling rules were tested in a collision of two model D grains with a relative velocity of 0.2 m/s (see Fig. 3.1a). The simulation parameters are listed in Table C.1. The evolution of the contact energy density is shown in Fig. 3.1b. Indeed, if scaling according to Eqs. (3.7a)–(3.7c) is applied, the energy density evolution of the contact is independent of the grain diameter d. For all other cases dependencies on d exist. The evolution of the relative contact deformation, h_{ij}/d, is shown in

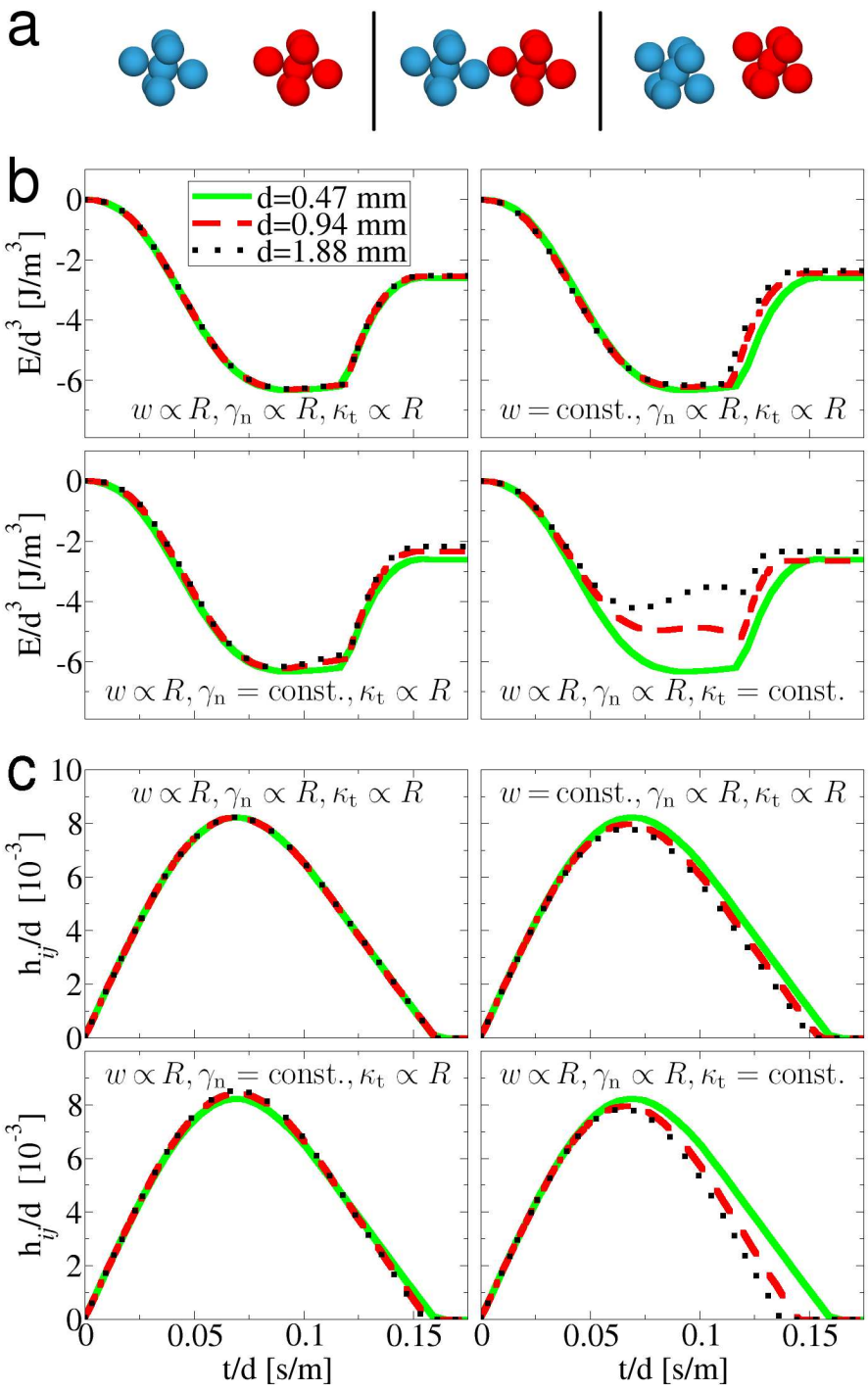

Figure 3.1: (a): Grains before, during and after the collision. Evolution of (b) energy density and (c) contact deformation during the collision with various scaling laws.

Fig. 3.1c. A collapse is only observed for the proposed scaling rules. Thus, only in this case the trajectories are self-similar for varied grain diameter.

The scaling could also be based on stresses instead of energy densities. As consequence of the proposed force scaling the stresses in the system remain unchanged. The stress tensor of a grain i is given by

$$\sigma_i = \frac{-1}{V_i}\left[m_i\left(\mathbf{v}_i - \langle\mathbf{v}\rangle\right)\otimes\left(\mathbf{v}_i - \langle\mathbf{v}\rangle\right) + \sum_j \mathbf{f}_{ij}\otimes\hat{\mathbf{r}}_{ij}\left(R - \frac{h_{ij}}{2}\right)\right], \tag{3.8}$$

where $\langle\mathbf{v}\rangle$ is the local mean velocity. It follows directly from the discussion above that the stress tensor is independent of R provided that the forces scale with R^2.

The cohesive tensile strength of the powder shall be discussed as a specific example. Johnson *et al.* [54] derived the expression $F = -3\pi wR/4$ for the load required to separate two spheres with radius R which are initially in contact. When choosing $w \propto R$ the contribution of the cohesion to the tensile strength of the powder bulk, given by F/R^2, thus becomes independent of the actual grain diameter.

The derivation of the force scaling was shown to be valid for a dilute granular system where only binary collisions occur and for a dense system via the stress tensor. It is not clear that the scaling is also valid in intermediate dense regimes and for multiple grain collisions. Thus, further tests of the scaling rules in relevant setups are presented in the following section.

3.2 Coarse graining tests

The coarse graining scheme was verified using grain models A and D. Bulk properties, flow rates and angles of repose were studied. In these setups both static and dynamic properties of the grain models can be monitored.

3.2.1 Bulk properties

As a first test, the scaling behavior of particle deformations h_{ij}, coordination numbers and the height-dependence of the volume fraction was considered. A slab consisting of model D powder with an initial volume fraction of 0.1 is set up. Periodic boundary conditions in x and y were applied and the powder is allowed to settle and relax under gravity on a ground plate (see Fig. 3.2). The plate consists of an array of fixed overlapping spheres which are scaled according to the grains. Two sets of parameters were tested using the proposed adequate parameter scaling. One set includes no cohesion and medium friction while the other one includes cohesion and high friction (see Table C.2 for details).

Figures 3.3a–c show histograms of h_{ij}/d and coordination numbers as well as the spatial variation of volume fractions for grain diameters varying from $d = 470\,\mu$m to 1.88 mm. All diagrams collapse for both sets of parameters. Thus, no effect of coarse graining can be observed. The particle deformation has a maximum at $2\cdot10^{-4}d$ for the non-cohesive and at $8\cdot10^{-4}d$ for the cohesive grains. The collapse of the curves for h_{ij}/d confirms that the applied force scaling yields self-similarity of the contact details, i.e. the contact deformation scales linearly with the grain size. The average coordination number of 5 of the non-cohesive grains is significantly higher than the coordination number of about 4.5 for the cohesive case. Also the volume fractions are independent of grain size apart from regions close to the ground at $z = 0$ and close to the top.

Close to a boundary, the volume fraction is significantly reduced due to grain confinement (see Fig. 3.3d). It can be clearly seen that the volume fraction converges to the bulk value about $1\,d$ away from the boundary in agreement with experimental observations [68]. In the vicinity of the boundary the volume fraction drops to values as low as 0.18 followed by a second drop to zero when the boundary is reached. This behavior is considered an artifact arising from the boundary consisting of overlapping spheres which are centered at $z = 0$ with a radius $d/6$. These spheres were excluded from the volume fraction calculations. Therefore, the volume fraction starts to decrease at the highest surface points of the boundary spheres and finally vanishes when the boundary spheres completely overlap in the xy-plane (compare also Fig. 2.5).

For comparison, the same bulk formation simulations were carried out using inadequate scaling of the force constants, i.e. without satisfying Eqs. (3.7a)–(3.7c). Three sets of parameters were used. First, the damping parameter, γ_n, was set

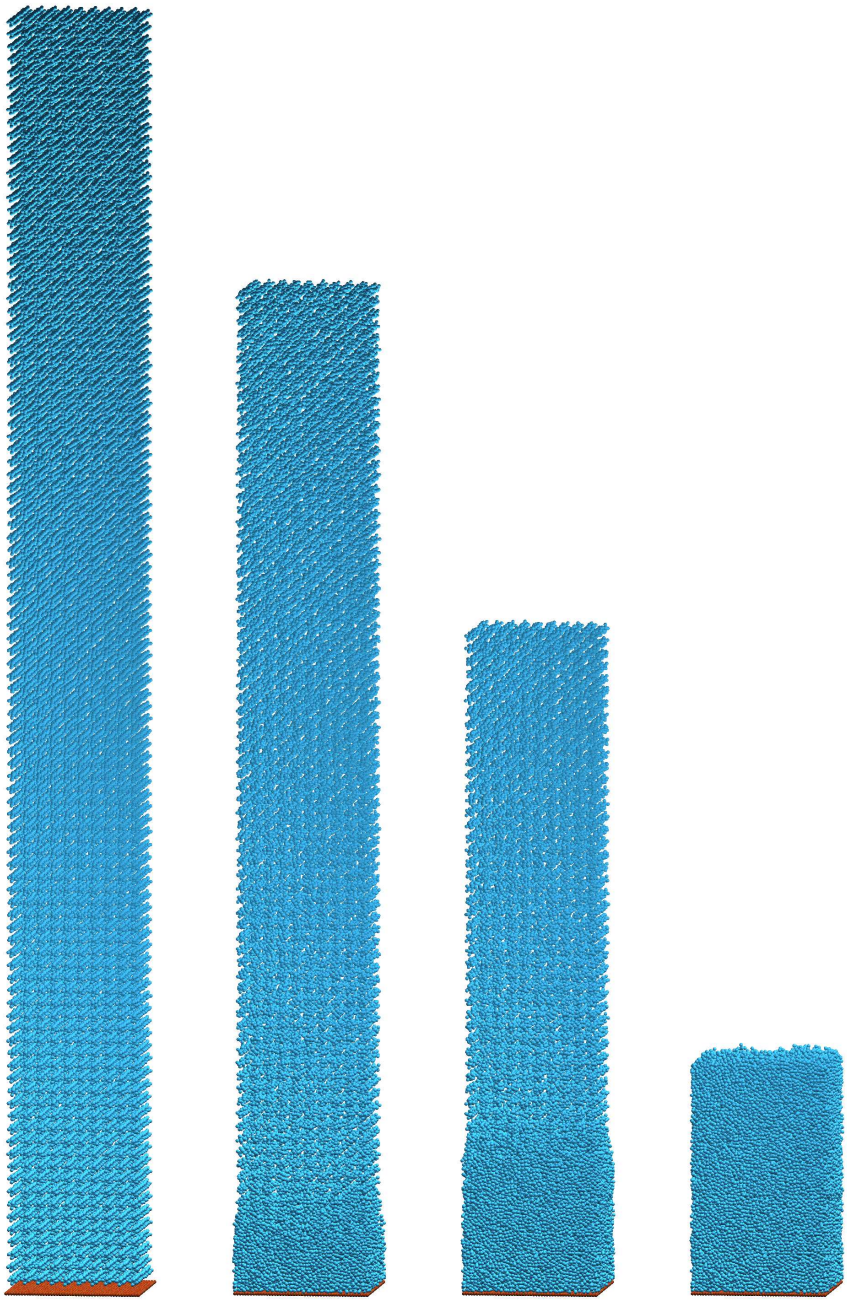

Figure 3.2: From left to right: Formation of a granular bulk under gravity on a fixed ground plate.

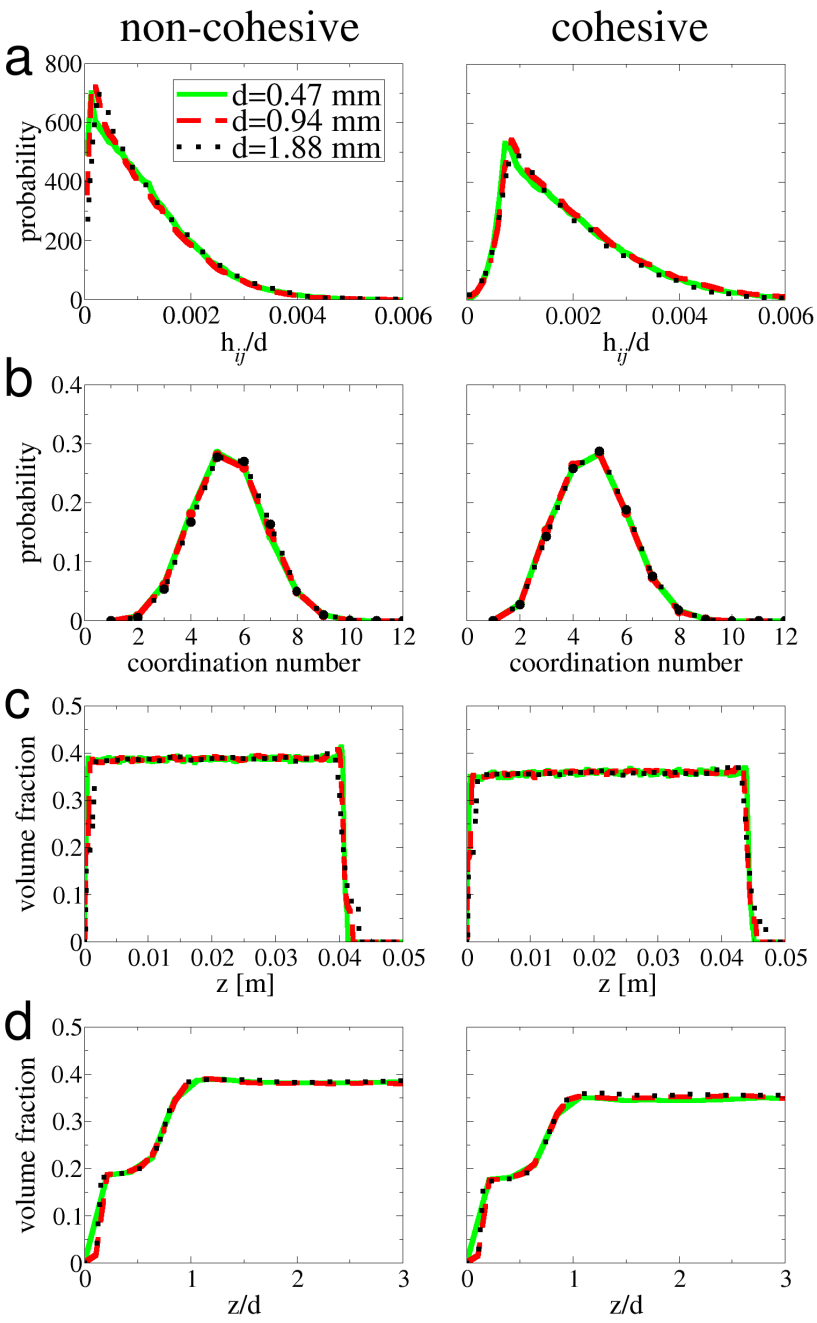

Figure 3.3: Analyses of the coarse graining method for bulk formation: Histograms of (a) particle deformation and (b) coordination number as well as the height dependence of the volume fractions (panels c and d) for non-cohesive and cohesive model D grains.

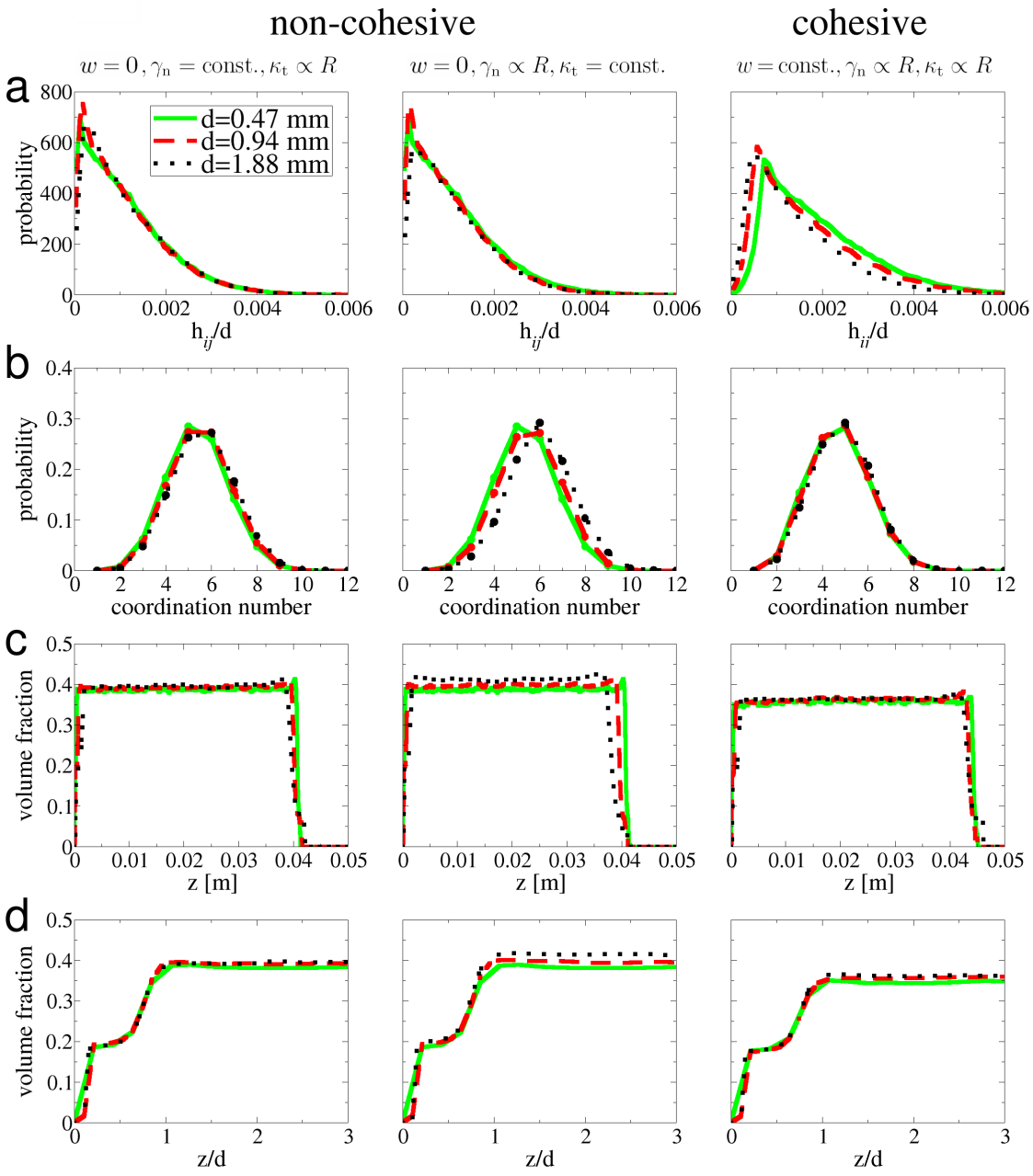

Figure 3.4: Same as Fig. 3.3 but for inadequate force scaling with γ_n, κ_t or w, respectively, kept constant.

to a constant value for all grain diameters tested. Second, the tangential spring constant, κ_t, was kept constant during coarse graining. In both cases all other parameters were the same as in the non-cohesive parameter set used above. Third, the cohesive parameter set was modified by keeping the adhesion per unit contact area, w, constant. An overview of all parameters used is given in Table C.2. Note, the parameter sets for *inadequate* scaling were chosen in such a way that they coincide with the parameter sets for *adequate* scaling for the smallest grain diameter, i.e. $d = 470\,\mu$m.

Figure 3.4 shows the resulting bulk properties for inadequate force scaling. For $\gamma_n = \text{const.}$ or $\kappa_t = \text{const.}$ the particle deformation histograms still collapse. However, coordination numbers are shifting to higher values and the volume fractions increase with increasing grain size. Both effects are more pronounced for fixed κ_t. In the cohesive case with fixed w the relative particle deformation is larger for smaller grains. Coordination numbers and volume fractions increase slightly with increasing grain size. In summary, it was found that the tested bulk properties are independent of the actual grain size only if the proposed force scaling is applied.

3.2.2 Slit flow

Next, the influence of coarse graining on flow properties was examined. Discharge rates (i.e. steady state flow rates through a slit opening during a feeding shoe passage at constant velocity) were considered a suitable measure for evaluating scaling effects. The setup is depicted in Fig. 3.5a. In general, discharge rates decrease for bigger particles since boundary effects become more prominent, i.e. the particles *see* an effective smaller opening. This phenomenon was already observed by Beverloo *et al.* [20] in hopper discharge experiments.

Figures 3.5b–d show normalized flow rates $\tilde{W} = W_p V_p / b^{sim}$ as a function of slit size D for different grain diameters and models. The according simulation parameter sets are listed in Table C.3. Here W_p denotes the grain discharge rate, V_p the grain volume and b^{sim} the y-periodicity of the simulation box. The curves collapse when the flow rate is plotted against an effective slit size $D - 1.4d$. This procedure and also the value 1.4 were already proposed by Beverloo *et al.* for hopper outflow. Note however that the curves are less smooth for bigger grains (see inset in Fig. 3.5b).

The collapse for the cohesive model D powder is only obtained when the cohesive energy per contact area is scaled with R: $w/R = 128\,\text{J/m}^3$. For constant w, flow rates are too high for larger grains and too low for smaller grains with respect to $d = 470\,\mu$m, where the parameter sets of adequate and inadequate scaling coincide (see Fig. 3.5d). Clearly, in the latter case the powder shows a decrease of cohesive strength with increasing grain size since the cohesive energy per volume diminishes with R.

In Fig. 3.6 color coded velocity and volume fraction fields are displayed for dif-

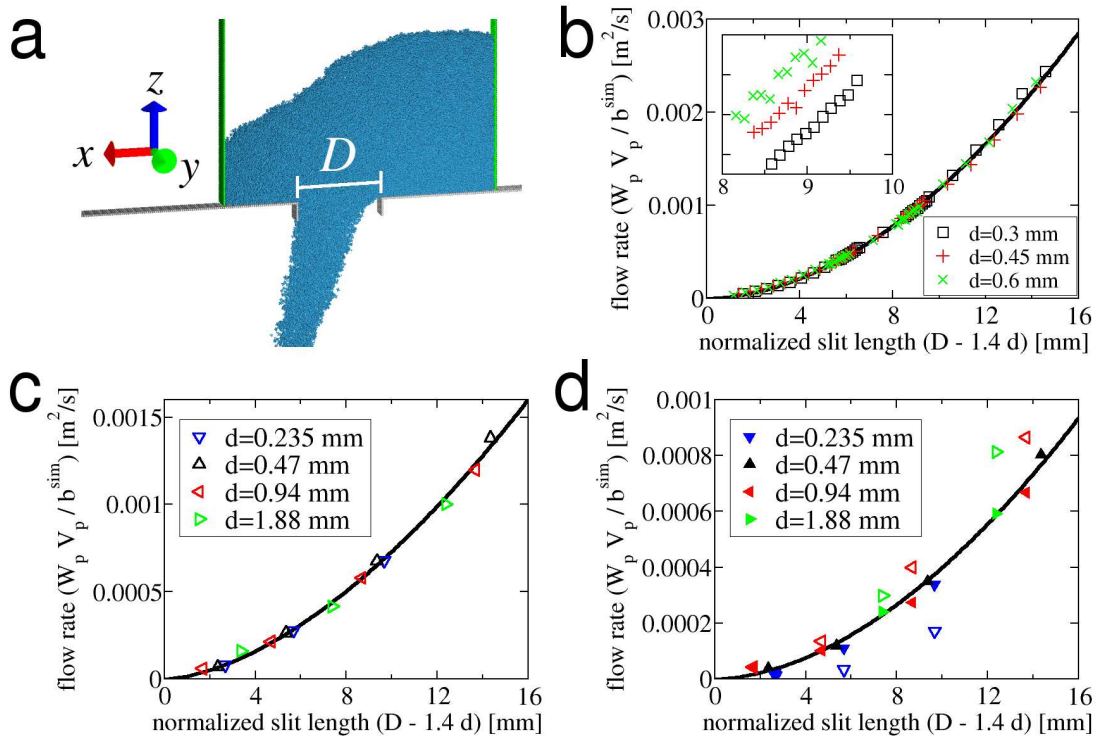

Figure 3.5: (a): Simulation snapshot of granular outflow from a feeding shoe (green) moving in $+x$-direction through a slit in the ground (gray). (b–d): Flow rate as a function of slit size D at shoe velocity $v_s = 0.18\,\mathrm{m/s}$ for different particle sizes. (b): Model A without cohesion; inset: blow up of the main panel with $d = 450\,\mu\mathrm{m}$ and $d = 600\,\mu\mathrm{m}$ shifted up for clarity. (c): Model D without cohesion. (d): Model D with cohesion; closed symbols: $w \propto R$, open symbols: $w = \mathrm{const}$.

ferent grain sizes of a cohesive model D powder ($w/R = 1920\,\mathrm{J/m^3}$, $\mu = 1.0$, all other parameters as listed in Table C.3) flowing through a $D = 10\,\mathrm{mm}$ slit at $v_s = 0.18\,\mathrm{m/s}$. The velocity fields are similar except for areas of low velocity behind the slit. Here the flow is more pronounced for larger grains. The wall particles have constant size and grid spacing and therefore the coarser powders experience a reduced roughness resulting in a reduced effective wall friction. More details on this effect are given in Section 4.2.4. The volume fraction fields are also alike, only slightly noisier for larger grains.

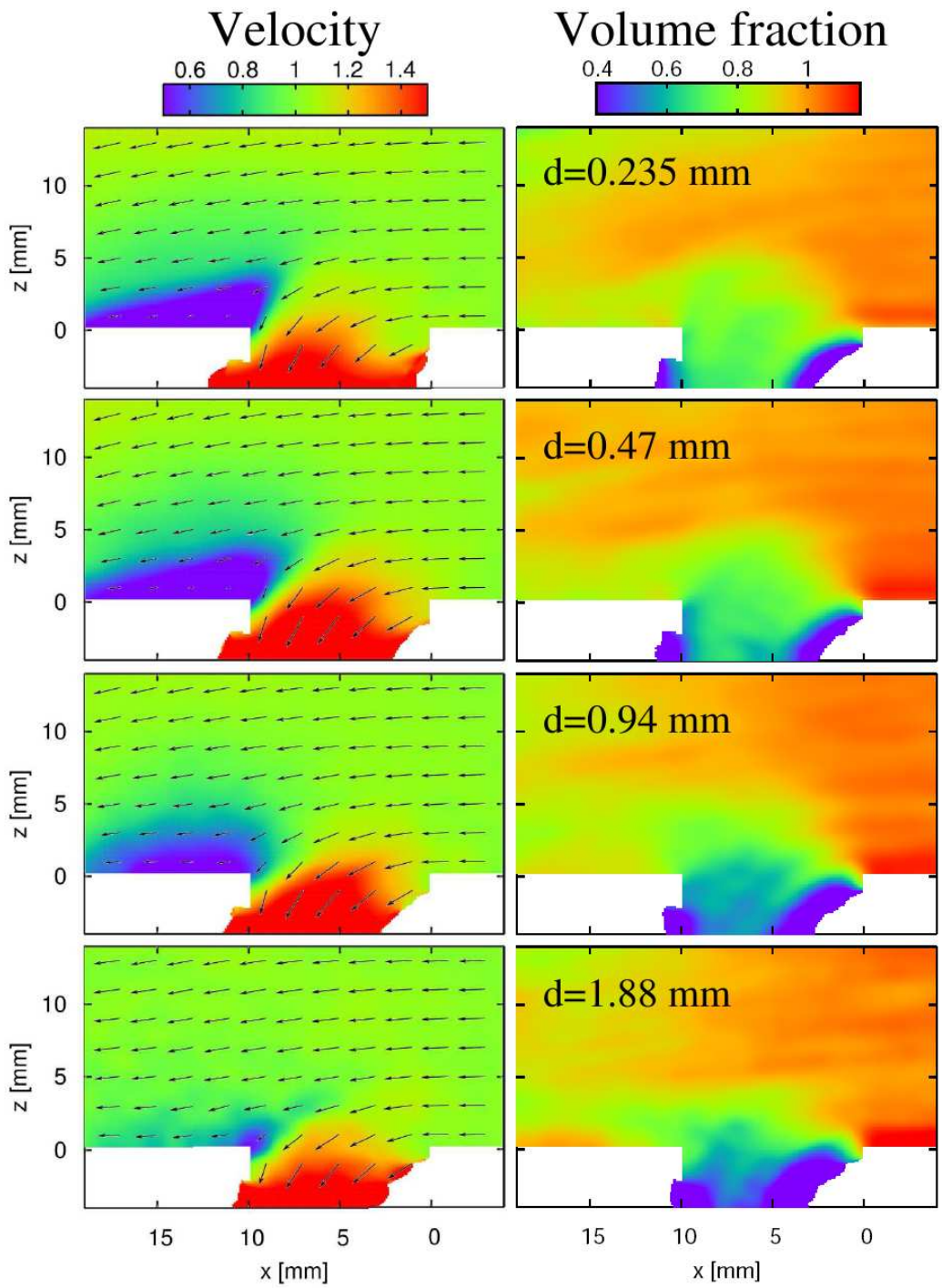

Figure 3.6: Velocity and volume fraction fields for varied grain diameter d using model D. The setup is displayed in Fig. 3.5a. The velocity is normalized by the shoe velocity, $v_s = 0.18\,\mathrm{m/s}$. The volume fraction is normalized by the bulk value of 0.30. The standard deviation of the Gaussian weighting for smoothing is $\sigma = 0.5\,\mathrm{mm}$.

d [mm]	0.235	0.47	0.94	1.88
θ_{O} [°]	38	39	37	32
θ_{H} [°]	39	39	37	—

Table 3.1: Dependence of outflow angle and heap angle of repose on coarse graining level for model D powder.

3.2.3 Angle of repose

Angles of repose were studied for model D grains (parameters listed in Table C.3, $w \propto R$). Figure 3.7a shows a sequence of simulation snapshots during the heap formation using a moveable slider. The angles of repose were measured after the grains have come to a rest. The angles θ_{O} and θ_{H} are not substantially influenced by coarse graining (see Fig. 3.7b and Table 3.1). However, the curvature of the heaps increases with particle size. The shape of a granular heap's tail can be described by the expression $x = (z_{\max} - z) \,/\, \tan\theta + l_e \log(z_{\max}/z)$, where l_e is proportional to the grain diameter [69]. This explains the more pronounced tail of the ground heap for bigger grains. A similar effect is observed for the peak of the slider heap which becomes more oblate with increasing grain size. An inspection of the initially horizontally colored grain layers in Fig. 3.7b suggests that surface flow extends deeper into the bulk for bigger grains. Due to computational limitations it was not possible to carry out simulations with grain diameters significantly smaller than $235\,\mu$m. However, Fig. 3.7b hints that the simulations using $d = 235\,\mu$m and $d = 470\,\mu$m are representative for even smaller grains.

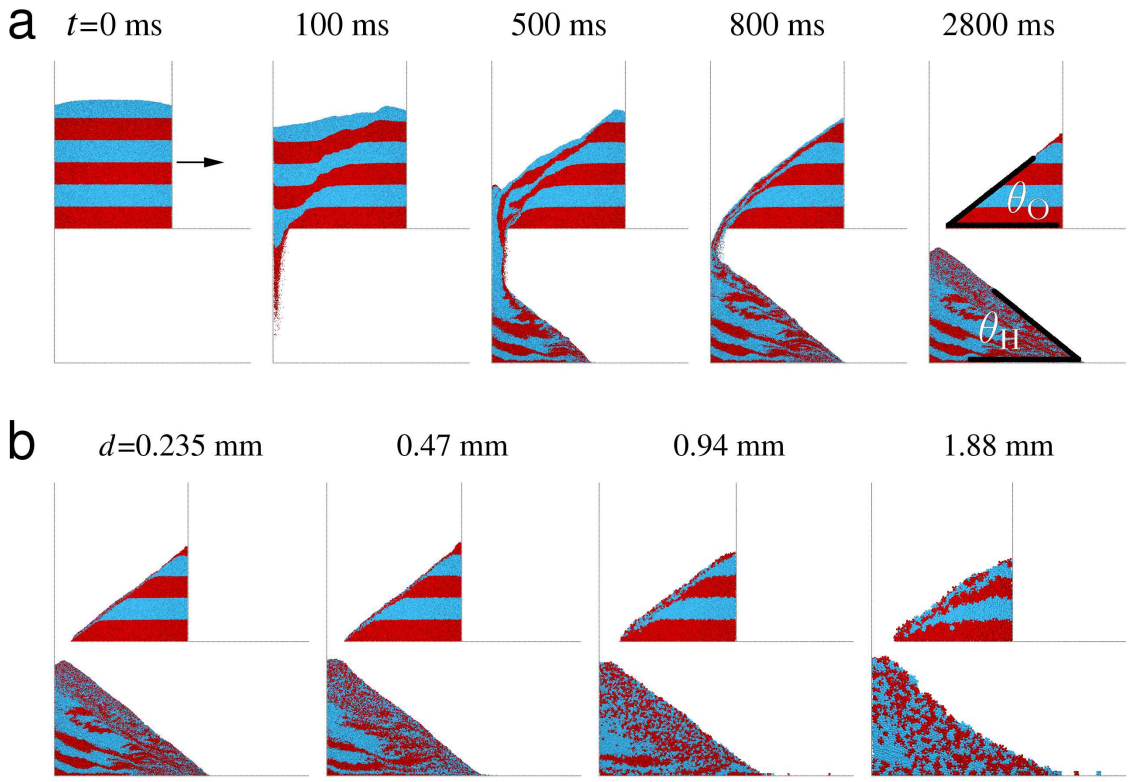

Figure 3.7: (a): Angle of repose formation with definitions of outflow angle, θ_O, and heap angle, θ_H. The setup is periodic along the axis perpendicular to the paper plane. (b): Dependence of angles of repose on grain diameter d for model D powder.

3.3 Conclusion

A coarse graining scheme was proposed which can be applied to overcome the problem of un-manageable grain numbers in DEM simulations. Scaling rules for the material parameters in a coarse grained system were derived by a dimensional analysis of the equations of motion in a binary granular collision combined with the requirement to preserve energy densities in system. Tests in dynamic bulk regimes confirmed that the scaling scheme is not limited to dilute configurations where only binary collisions occur. In fact, it is possible to obtain the same properties (e.g. coordination number, volume fraction, angle of repose) of a given granular system independent of the actual coarse graining level. Limitations arise only if length scales of the system (e.g. the orifice diameter) become comparable to the grain size. Of course, the scheme cannot be applied in a reasonable way if properties of the system depend intrinsically on grain dimensions.

The results hint that the energy density rather than the grain size is characteristic for many granular bulk systems. This supports the fact that continuum descriptions of granular matter do not necessarily contain grain size related parameters (compare Section 5.1).

4 Modeling of real powders in static and dynamic regimes

Particle based numerical simulations yield detailed insight into a granular ensemble due to the availability of complete phase space and contact information. However, only the usage of a reliable numerical model provides the basis for any kind of further analysis. Thus, the objective of the investigations presented in the current chapter is to identify a DEM model which is capable of describing static and dynamic properties of a real powder quantitatively in diverse setups. The model could then be used in the *virtual laboratory* in order to gain trustworthy results. So far, no studies have been conducted which try to identify a model of such flexibility. Investigations were rather focused on single regimes, e.g. flow from a hopper or down an inclined plane, shear in a couette cell or angle of repose formation [70, 71, 72, 73]. A priori, it is not clear that a model which resembles the reality well in one regime does the same in another one. As benchmark experiments the discharge from a moving shoe and the formation of angles of repose were used. The first setup reflects a strongly dynamical situation while the second one is dominated by static powder properties. The experiments were carried out using ASC100.29 iron powder provided by Höganäs AB consisting of irregular shaped grains with a mean diameter of about 100 μm (see Fig. 4.1a).

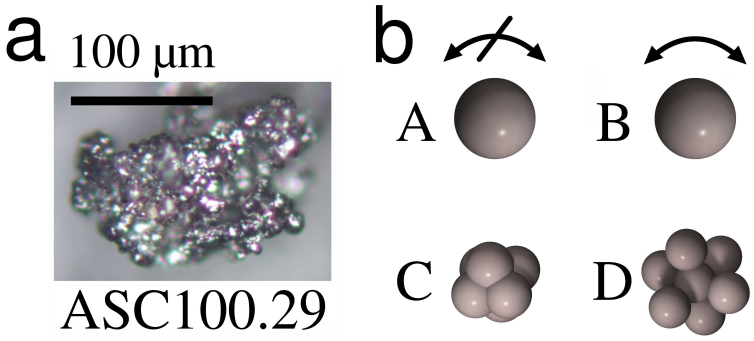

Figure 4.1: (a): Microscopic image of an ASC100.29 grain. (b): DEM grain models.

4.1 Model fitting and validation

The DEM powder models A, B, C, and D (Fig. 4.1b) as introduced in Section 2.1 were tested for their capabilities to resemble the behavior of ASC100.29 in both the dynamic and the static setup. In addition, volume fractions, discharge dependence on powder bulk height, and the filling of a circular cavity were used to distinguish between the models in terms of realism.

The formulations of the DEM force laws are derived from physically plausible interaction mechanisms. Yet, the force laws form a simplification of the real interaction. The corresponding parameters do not necessarily reflect distinct material properties. Therefore, the parameters cannot be easily identified independent of each other for given real powder. Rather a certain combination of force law parameters characterizes an effective granular medium.

The parameters were adjusted via inverse modeling using two different fitting strategies. In the first strategy the mass flow of the ASC100.29 iron powder from a moving shoe through a defined slit was used for the fitting yielding a certain set of model parameters. In the second strategy the same model parameters were adjusted such that the experimental angles of repose were reproduced as closely as possible. The fixed model parameters are listed in Table C.4. Free fitting parameters for all models were the Coulomb friction coefficients $\mu^{\mathrm{A,B,C,D}}$ and the cohesive energy densities $w^{\mathrm{A,B,C,D}}$. For model B the rolling friction coefficient $\mu_{\mathrm{r}}^{\mathrm{B}}$ was an additional tunable parameter. These parameters were chosen, because they strongly affect the behavior of the model powders in the studied setups. The influence of further model parameters is discussed in Section 4.2.

4.1.1 Fitting of parameters to slit outflow

Experimental setup

A model system as shown in Fig. 4.2 was set up. Its design resembles a similar device presented in Refs. [74, 29]. A perspex feeding shoe (32 mm long, 50 mm wide, 37 mm high) moves over an exchangeable polished steel platen (2 mm thick) which contains a slit orifice. The shoe is attached to a valve-controlled pneumatic cylinder allowing movement at a constant velocity in the range between 0.1 and 0.8 m/s, matching the speed of typical industrial devices. The shoe movement is recorded by a displacement transducer connected to a PC. The influence of the acceleration phase was not investigated as it is negligible [74].

The powder delivered through the slit orifice is collected in a perspex box and weighed with a milligram balance. Plots of the shoe-velocity-dependent powder mass transfer were used as a measurement for powder flowability as done by other authors [74, 29, 75, 76].

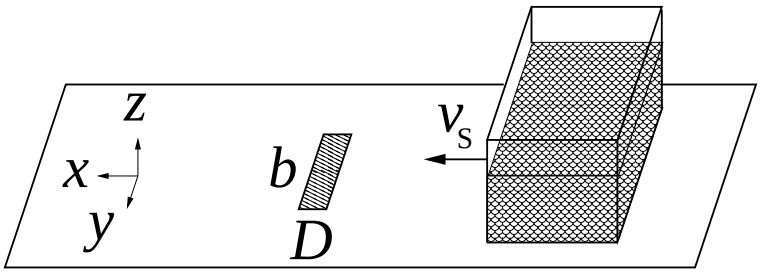

Figure 4.2: Schematic of experimental slit discharge system. The feeding shoe moves at constant velocity v_s. The edge lengths of the slit orifice are D and b.

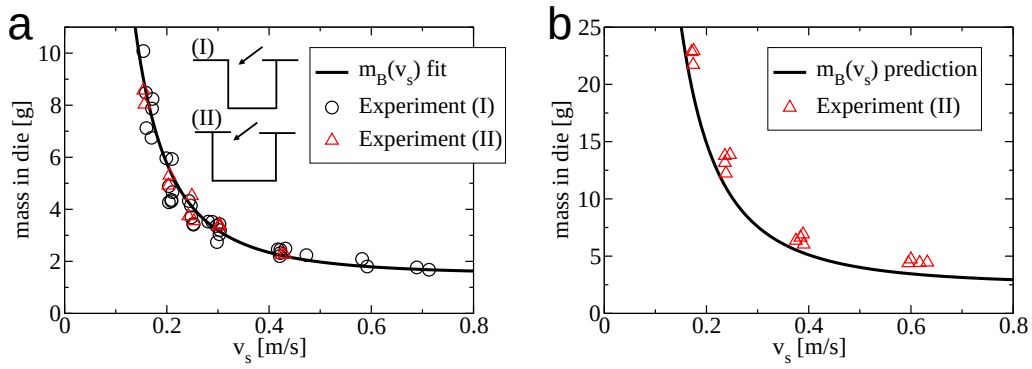

Figure 4.3: Measured powder discharge for the (a) $D = 6\,\text{mm}$ and (b) $10\,\text{mm}$ slit, both with $24\,\text{mm}$ filling height in the shoe.

Experimental results

Figure 4.3 shows the powder mass delivered through orifices with $D = 6\,\text{mm}$ and $10\,\text{mm}$ (both $b = 33\,\text{mm}$ wide) for a range of shoe velocities.

No difference in mass discharge was found between a setup with a box whose vertical wall meets the edge of the orifice or a setup with a vertical wall that is well separated from the edge (insets (I) and (II) in Fig. 4.3a). This means that the results obtained from outflow through a slit are transferable to filling cuboid shaped cavities with rectangular orifices. Discrepancies between these two cases may arise for fine powders because of hindered powder flow due to entrapped air in closed cavities [74, 29, 75]. However, this effect is beyond the scope of this work and not taken into account.

The data from the $D = 6\,\text{mm}$ slit (Fig. 4.3a) are fitted using an exponential law

C_B	C_I	C_F	β
0.081	0.024	4.3	0.093

Table 4.1: Fitted parameters for slit discharge.

for mass discharge from a shoe of length l with velocity v_s,

$$\begin{aligned} m_\mathrm{B}(v_\mathrm{s}) &= \rho_\mathrm{a}\, D\, b\, l\, f_\mathrm{B}\left(\frac{\sqrt{gD}}{v_\mathrm{s}} - x_0\right), \\ f_\mathrm{B}(x) &= C_\mathrm{B} + C_\mathrm{F}\left(x + \frac{1 - C_\mathrm{I}/C_\mathrm{F}}{\beta}\left(e^{-\beta x} - 1\right)\right) \end{aligned} \tag{4.1}$$

as derived in Section 5.2. The apparent density of the ASC100.29 iron powder is $\rho_\mathrm{a} = 3.0\,\mathrm{g/cm^3}$, $x_0 = 1/5$ characterizes the duration of an initial burst phase (see Section 5.2.1) and g denotes the gravitational acceleration. The fitted dimensionless parameters C_B, C_I, C_F and β are listed in Table 4.1.

The prediction of Eq. (4.1) is compared with experimental data for the $D = 10\,\mathrm{mm}$ slit in Fig. 4.3b. The general trend of the experimental data is reproduced well. Only the absolute values are slightly underpredicted. A more detailed discussion of this effect is given in Section 5.2.3.

Model fitting

The simulation setup for the powder discharge from a moving shoe through a slit orifice resembles the experiment. The only difference is the application of periodic boundary conditions along the y-axis. These were used to save computational time. It was carefully checked that the periodic box width, b^sim, has no influence on the simulation results for $b^\mathrm{sim} \geq 5d$. In order to compare experiments and simulations, the sectional area of powder bulk in the xz-plane discharged through the orifice was calculated,

$$A_\mathrm{exp}(v_\mathrm{s}) = \frac{m_\mathrm{B}(v_\mathrm{s})}{\rho_\mathrm{a}^\mathrm{exp}\, b}, \quad A_\mathrm{sim}(v_\mathrm{s}) = \frac{P(v_\mathrm{s})\, m}{\rho_\mathrm{a}^\mathrm{sim}\, b^\mathrm{sim}}, \tag{4.2}$$

where $m_\mathrm{B}(v_\mathrm{s})$ denotes the discharged mass according to Eq. (4.1), b the slit width in y-direction, $P(v_\mathrm{s})$ the number of discharged grains, m the mass of a single grain, and $\rho_\mathrm{a}^\mathrm{exp,sim}$ the apparent densities obtained in experiment and simulation, respectively. The free parameters μ, w, and μ_r were adjusted in a series of subsequent simulations. Figure 4.4a compares $A_\mathrm{exp}(v_\mathrm{s})$ with $A_\mathrm{sim}(v_\mathrm{s})$ from simulations using initial and fitted parameter sets (see Table 4.2). It was possible to find an optimized parameter set for each model (referred to as A1 to D1).

In order to quantify the parameter fitting, perpendicular residuals [77] were calculated. For a given set of parameters the perpendicular residual ϵ^2 is the sum of

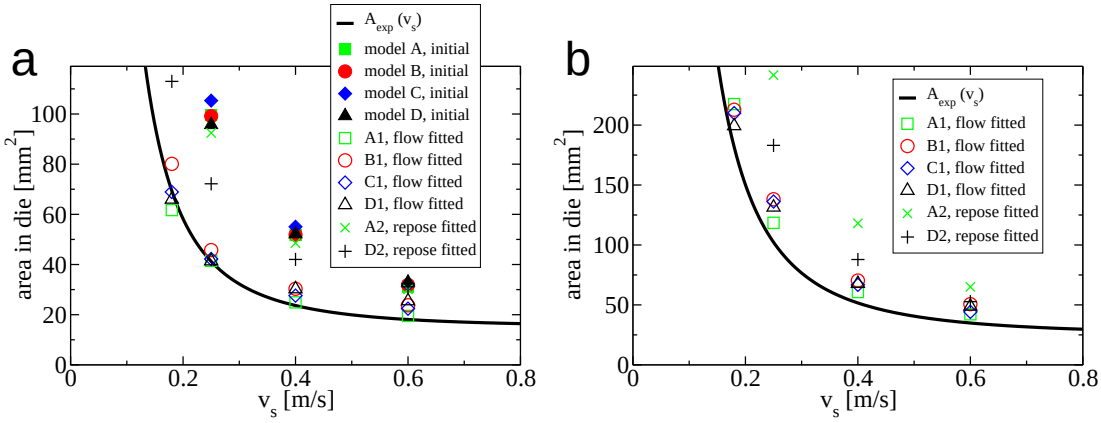

Figure 4.4: Powder discharge through the (a) $D = 6\,\mathrm{mm}$ and (b) $10\,\mathrm{mm}$ slit. Results from various powder models (open and closed symbols) are compared with the experiments (black line). The model parameters labelled *flow fitted* were adjusted to the $D = 6\,\mathrm{mm}$ experiment while the $D = 10\,\mathrm{mm}$ results represent predictions.

Model:	A1	A2	B1	C1	D1	D2
initial μ [ ]				0.25		
fitted μ [ ]	1.0	0.3	1.0	1.0	1.0	1.0
initial w [J/m^2]				0.0		
fitted w [J/m^2]	$1.0 \cdot 10^{-2}$	0.0	$1.0 \cdot 10^{-3}$	$2.0 \cdot 10^{-1}$	$1.5 \cdot 10^{-1}$	$1.0 \cdot 10^{-2}$
initial μ_r [m]	—	—	$3.75 \cdot 10^{-5}$	—	—	—
fitted μ_r [m]	—	—	$3.75 \cdot 10^{-4}$	—	—	—

Table 4.2: Initial and fitted values for the adjustable parameters of the simulations. A1, B1, C1, D1: fitted in slit outflow; A2, D2: fitted in angle of repose formation.

squared distances d_i between the k data points $(v_{\mathrm{s},i}, A_{\mathrm{sim},i})$ from simulations and a parameterized curve,

$$\mathbf{C}(v_\mathrm{s}) = \begin{pmatrix} v_\mathrm{s} \\ A_\mathrm{exp}(v_\mathrm{s}) \end{pmatrix}, \tag{4.3}$$

describing the experimentally found relation between shoe velocity and discharged area. Note that v_s is a continuous variable while the $v_{\mathrm{s},i}$ are discrete values. The perpendicular residual is defined as

$$\begin{aligned} \epsilon^2 &= \frac{1}{k}\sum_{i=1}^{k}\delta_i^2, \\ \delta_i^2 &= \left(\mathrm{dist}\left[\begin{pmatrix} v_{\mathrm{s},i}/v_\mathrm{s,max} \\ A_{\mathrm{sim},i}/A_\mathrm{max} \end{pmatrix}, \begin{pmatrix} v_\mathrm{s}/v_\mathrm{s,max} \\ A_\mathrm{exp}/A_\mathrm{max} \end{pmatrix}\right]\right)^2 \\ &= \min_{v_\mathrm{s}}\left[\left(\frac{v_{\mathrm{s},i}-v_\mathrm{s}}{v_\mathrm{s,max}}\right)^2 + \left(\frac{A_{\mathrm{sim},i}-A_\mathrm{exp}}{A_\mathrm{max}}\right)^2\right]. \end{aligned} \tag{4.4}$$

In order to avoid the influence of the chosen physical units and absolute values on the residuals, the axes are normalized by the maximum velocity $v_\mathrm{s,max}$ and the maximum area A_max, respectively. Residual plots for all tested models are displayed in Fig. 4.5. The thick green bars represent the model parameters fitting the experiment best. In the present work the parameters were adjusted by educated guessing a path through the parameter space. However, this process could be automated by using residuals as a target function in an appropriate minimization technique.

4.1.2 Validation by using a larger slit

The predictive ability of the powder models was explored in an experiment analogous to the fitting setup but with a larger slit, i.e. $D = 10\,\mathrm{mm}$. The agreement between experiment and simulation is good (Fig. 4.4b), considering that $m_\mathrm{B}(v_\mathrm{s})$ underestimates the experimental discharge slightly (compare Fig. 4.3b). With any of the four powder models A1–D1 the experimental discharge behavior is reproduced. Thus, it is not possible to distinguish between the quality of the models solely based on the slit outflow observations.

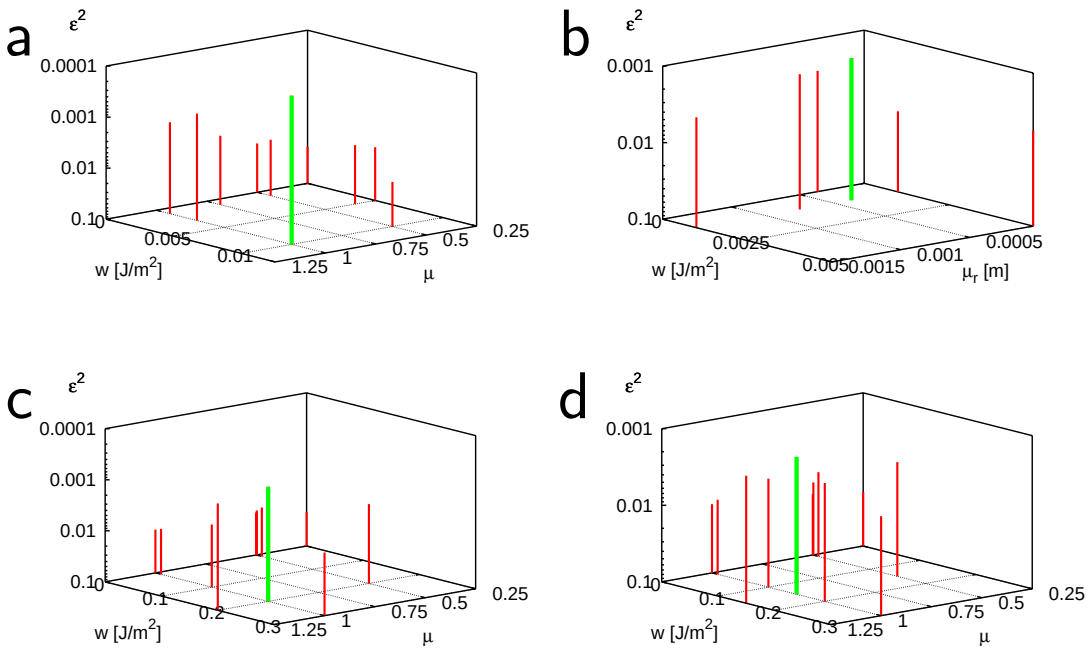

Figure 4.5: Plots of the residuals ϵ^2 (Eq. (4.4)) from parameter fitting via slit discharge for model A (a), model B with $\mu = 1.0$ fixed (b), model C (c), and model D (d).

4.1.3 Fitting of parameters to angle of repose

Experimental setup

To complement flow measurements the angle of repose was analyzed, which reveals static properties of a granular material. Its theoretical maximum value is related to the internal angle of friction of the material, $\phi = \arctan(T/N)$, where T is the maximum shear force the powder bulk can withstand when applying a normal force N [14]. It was shown by Grasselli *et al.* that at least five fundamentally different macroscopic angles exist depending on the formation history of a granular heap [78]. Two of them, namely the outflow angle, θ_{O}, obtained by heap decomposition through slow outflow and the heap angle, θ_{H}, obtained by heap composition via pouring grains on top of a newly forming heap were measured in a setup similar to the one used by Grasselli *et al.*, who found $\theta_{\mathrm{O}} > \theta_{\mathrm{H}}$. These two angles were used as the second part of the fitting and validation stage. The device consists of a perspex container (5 cm wide) with three sidewalls and a movable slider with one vertical wall (see Fig. 4.6a). The slider is supported by a plane 4.2 cm above the box ground and initially touches the container walls. Powder is poured into the

reservoir and the slider is gently moved a few millimeters by hand. The powder flows through the slit along one sidewall and finally a heap with angle θ_O forms on the slider while a heap with angle θ_H builds up on the container ground.

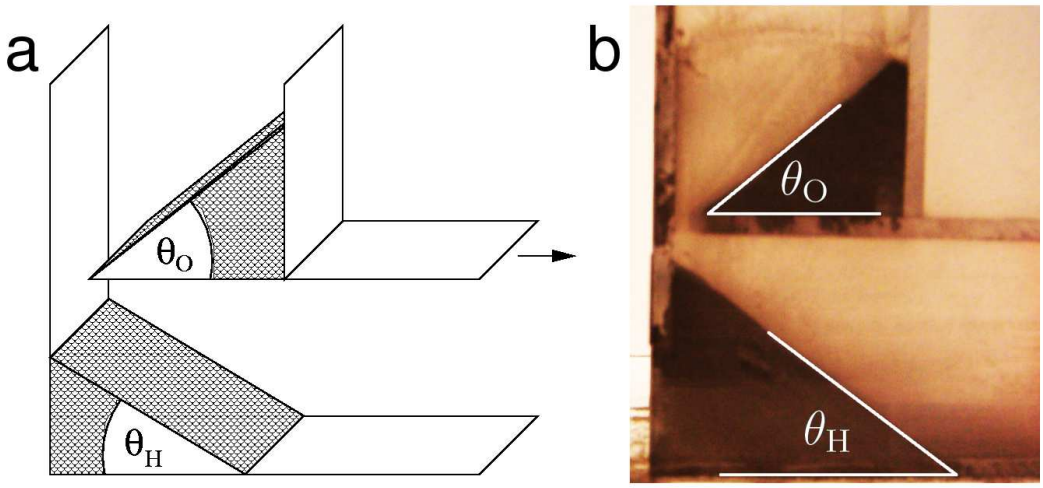

Figure 4.6: (a): Schematic of the experimental setup used for angle of repose measurements. (b): Angles of repose observed in heap (de)construction.

Experimental results

Figure 4.6b shows a typical result of the angle of repose experiments. An average over eleven experimental measurements yields values of the angles of repose of $\theta_O = (39.7 \pm 1.1)^\circ$ and $\theta_H = (37.0 \pm 0.6)^\circ$. No influence of the actual slit size (varying from 2–5 mm) was observed.

Model fitting

As for the slit outflow, periodic boundary conditions along the y-direction were employed in the simulations of the angle of repose formation. In the experiment the ratio of the perspex box width to grain diameter was roughly 500, while finite size effects are expected to vanish for a ratio above 180 [78]. Therefore, a periodic boundary approximation is considered to be a reasonable simplification of the experimental setup.

Figure 4.7 shows the result of the angle of repose simulations and experiment. Models B and C fail completely to describe the shape of the experimental heaps regardless of the used parameterization. Only models A and D are able to reproduce the experimental outflow angle, θ_O, as displayed in the lower panel of Fig. 4.7. The respective parameter sets are referred to as A2 and D2 in Table 4.2. The heap

	Experiment	A2	D2	D1
θ_O [°]	39.7 ± 1.1	41	39	59
θ_H [°]	37.0 ± 0.6	41	39	36

Table 4.3: Overview of outflow and heap angles of repose.

angles θ_H are slightly overestimated by the simulations. Model A2 reproduces the discharged heap worse than model D2, because a secondary heap with very low inclination is formed which is not observed on the experiment. Table 4.3 gives an overview of the angles of repose from experiments and from those simulations that exhibited straight slopes.

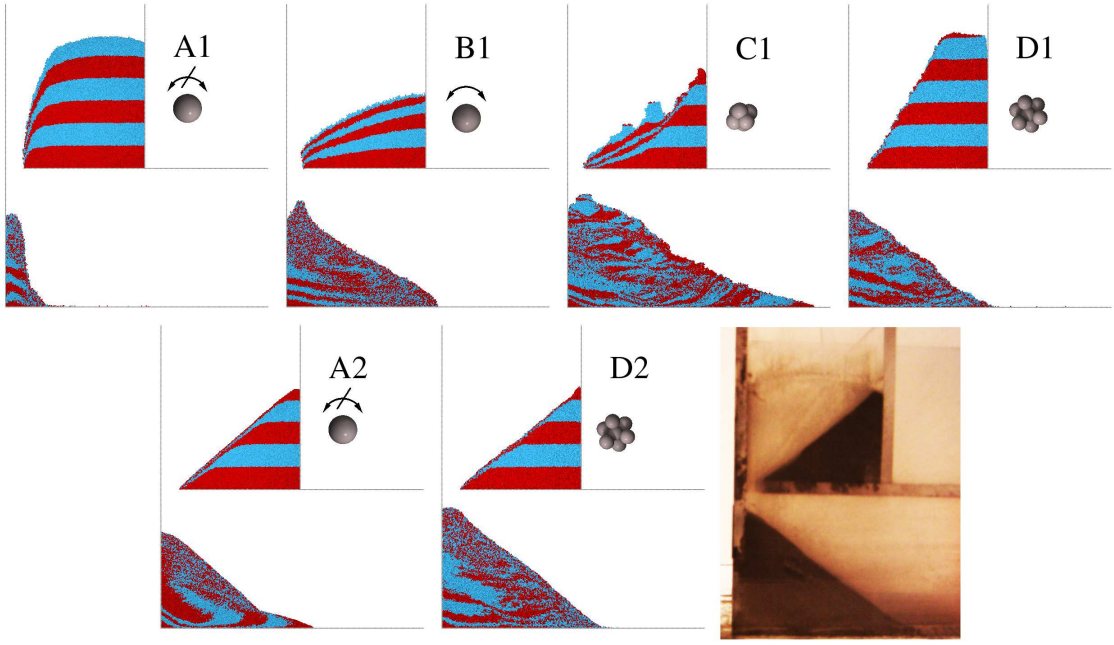

Figure 4.7: Angles of repose observed in heap (de-)construction. Simulations and experiment (lower right).

4.1.4 Reciprocal validation of slit outflow and angle of repose

As a validation step, angles of repose were calculated employing the model parameters that were fitted to the slit outflow experiment (see upper panel of Fig. 4.7). It can be observed that models A1 and B1 yield very unrealistic heap shapes. Grains still detach from the model B1 heap at a long time scale compared to the typical

heap formation time of about 2 s. This effect can be explained by the absence of a static friction torque (see discussion in Section 2.1.3). The rolling friction torque in Eq. (2.11) allows for a slow rotational motion of the spheres leading to the observed long term relaxations. Model C1 produces irregular slopes and also shows long term dynamical behavior, i.e. the heap *melts* slowly.

Only model D1 provides a reasonable description of the experiments. The observed $\theta_{\mathrm{H}} = 37°$ matches the experiment well. However, $\theta_{\mathrm{O}} = 59°$ overestimates the experimental value. A comparison of models D1 and D2 shows that the outflow angle θ_{O} is strongly influenced by the cohesive energy density w while the heap angle θ_{H} is not. In addition, the slopes for model D1 deviate stronger from straight lines than for the less cohesive model D2. Similar experimental observations were reported for a comparison of dry and wet particles [79].

In an additional validation step, the powder discharge through the $D = 6\,\mathrm{mm}$ and 10 mm slit is calculated using the models A2 and D2 from the angle of repose fitting procedure (see Fig. 4.4). Both models overestimate the observed powder outflow. However, model D2 comes closer to the experimental data than model A2.

In summary, either the slit discharge or the angle of repose is too large for model D with a certain set of parameters. A comparison of models C and D reveals that for a higher degree of sphericity the angle of repose is dramatically lower (if the heap is stable at all) while the discharge rate is just slightly larger. Thus, a refined model with somewhat more spherical grains than model D should be able to describe both, slit discharge and the angle of repose of ASC100.29 quantitatively.

4.1.5 Validation with volume fractions

The four models A1, B1, C1 and D1 differ significantly in the mean volume fraction f_{m}. For ASC100.29 iron powder $f_{\mathrm{m}} \approx 0.38$. Note that the value of f_{m} for random packing of hard spheres without cohesion lies between 0.64 (close packing [80]) and 0.55 (loose packing [81]). Table 4.4 reports mean volume fractions of the four models calculated by Voronoï tessellation as described in Section 2.2. Two values of f_{m} are given: after settling in the shoe at the beginning of the slit outflow simulations and after the acceleration phase during constant shoe motion.

The volume fractions of models A, B, and C with the initial parameter sets (before the fitting) are rather similar. This can be explained by the spherical or sphere like grains that were used in these models. Model D with the initial parameter set shows a significantly lower volume fraction due to the pronounced non-spherical shape. The optimized models with higher friction coefficients and cohesive surfaces yield a decrease in volume fraction of the order of 0.1. Yet, the optimized models A1, B1, and C1 are still less porous than ASC100.29 iron powder. On the other hand, model D1 has a higher porosity. The optimized model A2 is considerable denser than model A1. This can be explained by the fact that model A2 is non-cohesive and has only a slightly larger friction coefficient ($\mu = 0.3$) than the initial model

Model:	A1	A2	B1	C1	D1	D2
initial f_m [ ]	0.59/0.59		0.59/0.60	0.62/0.62	0.38/0.38	
fitted f_m [ ]	0.48/0.49	0.57/0.58	0.51/0.53	0.51/0.52	0.30/0.31	0.32/0.33

Table 4.4: Mean volume fractions for initial parameters and parameters fitted to slit outflow (A1, B1, C1, D1) or angle of repose (A2, D2); compare Table 4.2 for the actual values of the parameters. The slash separates values obtained after settling in the shoe and after acceleration of the shoe.

A ($\mu = 0.25$). Similarly, model D2 is a bit denser than model D1 due to weaker cohesion.

4.1.6 Validation with powder filling height in the feeding shoe

Slit outflow experiments showed that the discharged powder mass increases with a decrease of the initial powder filling height in the shoe (see lower right panel of Fig. 4.8). The effect is pronounced for low shoe velocities, i.e. $v_\mathrm{s} < 0.4\,\mathrm{m/s}$ for the $D = 6\,\mathrm{mm}$ slit. Small heights yield better flowability as *nose flow* becomes important, i.e. the bulk surface in the shoe declines significantly towards the slit and fast powder flow along the surface occurs [75]. For higher shoe velocities the differences for varied filling heights vanish, which is a hint that flow in this regime only occurs due to powder detaching from the bulk in the vicinity of the orifice (*bulk flow* [75]). In addition, an overall convergence for large filling heights is observed. Thus, the measurements with 24 mm filling height used for the model fitting in Section 4.1.1 are representative for the limit of large filling heights. The experimental findings were tested using models A1, B1, C1, D1, and D2 (see Fig. 4.8). Models A1 and B1 strongly overestimate the increase of discharge for a shallow filling height. Apparently, the spherical shape of the model A1 and B1 grains significantly promotes nose flow. Model C1 recovers the effect only rudimentary and model D1 not at all. Both models are very cohesive, which prevents surface declination and the associated increase in flow rate to some extend. Closest to the experimental observations comes model D2. For a shallow filling height of 10 mm the discharge is increased compared to 19 and 41 mm which lead to similar discharge behavior. The combination of moderate cohesion and asperitic shape appears to describe the nose/bulk flow behavior of ASC100.29 powder at least qualitatively in an adequate way.

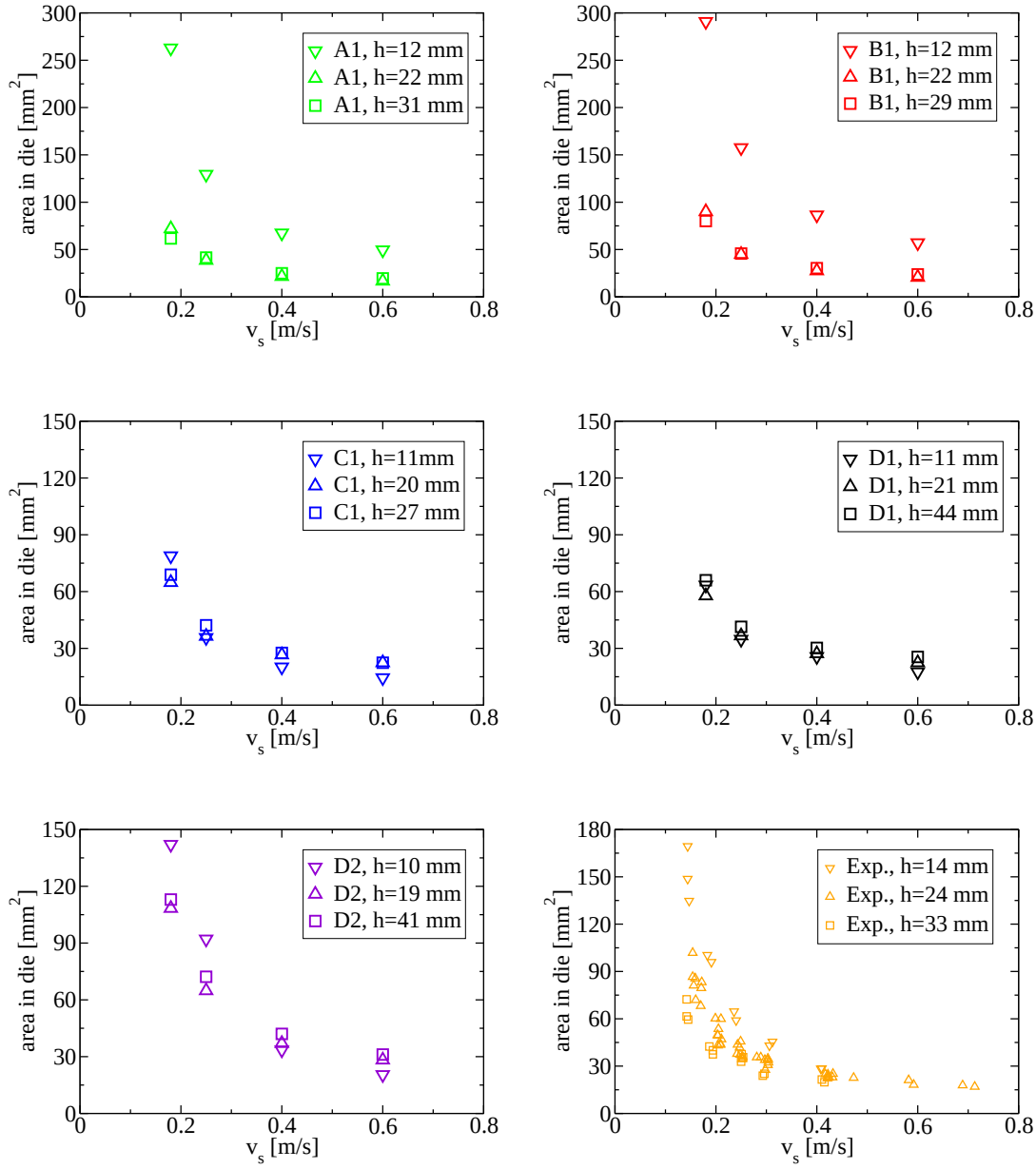

Figure 4.8: Slit discharge dependence ($D = 6\,\mathrm{mm}$) on powder filling height in the shoe. Models A1, B1, C1, D1, D2, and experiment.

4.1.7 Validation with filling levels in the circular cavity

Further filling experiments and simulations were carried out using a narrow circular cavity. The inner and outer diameter of the cavity are 16 mm and 20 mm, respectively, with a height of 15 mm (see Fig. 4.9).

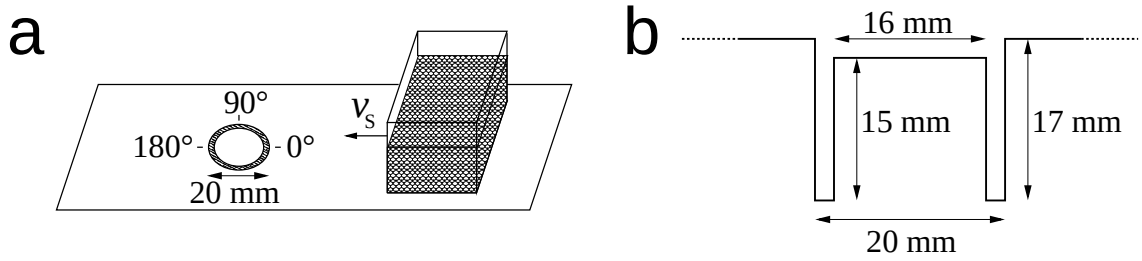

Figure 4.9: Schematic of the experimental setup used for filling of a circular cavity (a) and diametral view of the cavity (b).

The filling of the circular cavity was performed using two shoe velocities, 0.2 m/s and 0.5 m/s. The shoe meets the cavity first at the azimuthal angle of 0° and last at 180° (compare Fig. 4.9a). Figure 4.10 shows 3D visualizations of the filled cavities from simulations with models A1, B1, C1, D1, A2, and D2 for the two shoe velocities. Figure 4.11 presents a comparison of the filling heights measured in experiments (averaged over five repeated runs) and simulations. The filling heights are measured depending on the azimuthal angle of the cavity. It does not vary significantly in radial direction. The filling heights can be considered to be a suitable quantity for the validation of powder models since they reflect how much powder enters the cavity and in which way it settles within the cavity. Both velocities are sufficiently high to prevent complete filling of the cavity after just one shoe passage. The amount of discharged powder is higher for the lower shoe velocity. The angles of repose of the free surfaces are similar for both velocities in the experiment.

For $v_s = 0.2\,\mathrm{m/s}$, model D2 is the only one that almost reproduced the experiment. Merely the surface slope in the incompletely filled region deviates from the experiment. For $v_s = 0.5\,\mathrm{m/s}$, both, models D1 and D2 reproduce the experimental data well. The filling height close to 180° is slightly underestimated by model D1 and somewhat overestimated by model D2. All other models show larger deviations from the experiment. The strongest deviations are found for model A1 with the largest underestimation and model A2 with the largest overestimation of the experimental filling levels.

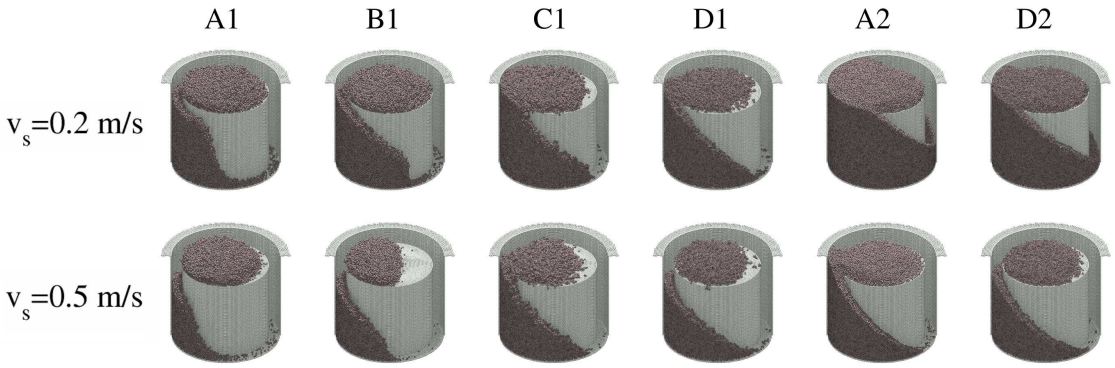

Figure 4.10: Incompletely filled ring cavities. The shoe passes from right to left.

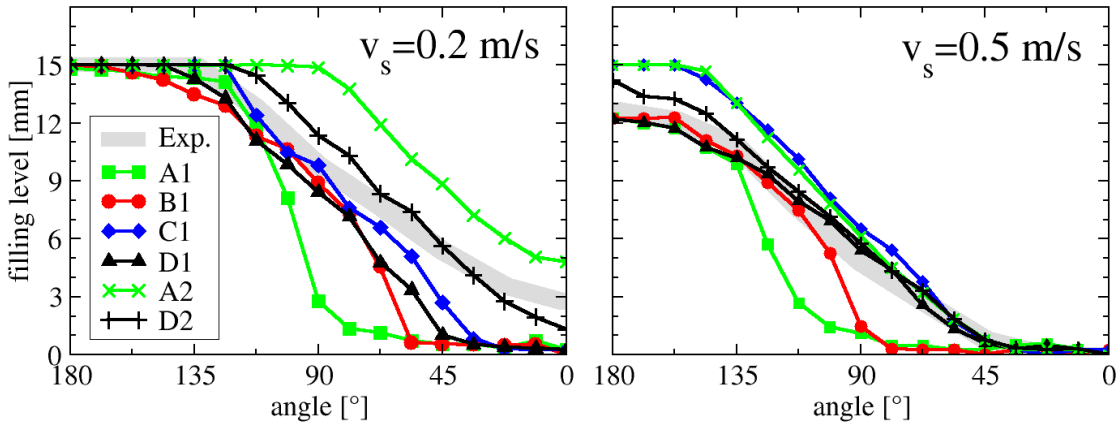

Figure 4.11: Comparison between experiments and simulations of filling levels in a ring cavity (Fig. 4.9) plotted along the azimuthal angle using different shoe velocities.

4.1.8 Velocity and volume fraction fields for slit outflow

Models A1, B1, C1, and D1 are able to resemble the integral mass discharge measured in the slit flow setups. In this section the question is raised whether or not the models differ on a more detailed scale. Velocity (Fig. 4.12) and volume fraction fields (Fig. 4.13) are analyzed in an area close to the 10 mm slit during discharge using the shoe velocities $v_s = 0.18\,\mathrm{m/s}$ and $v_s = 0.4\,\mathrm{m/s}$, respectively. For better comparability the velocity fields are normalized by v_s and the volume fraction fields by the average bulk volume fraction, f_m, of the respective model (as listed in Table 4.4). Both, velocity and volume fraction fields differ significantly for the different shoe velocities. On the scale of these differences, the four models exhibit essentially identical velocity and volume fraction fields for a fixed v_s.

For $v_s = 0.18\,\mathrm{m/s}$, the outflowing grains at ground level are about a factor 1.3 faster than the shoe. A zone with slow granular motion (velocity $< 0.6 v_s$) is located behind the slit close to the ground. This zone is more pronounced for models C1 and D1. All models exhibit arch-shaped velocity isolines in the vicinity of the slit similar to the case of hopper flow, i.e. $v_s = 0\,\mathrm{m/s}$ (compare Section 5.1). The volume fraction decreases from the bulk towards the slit and stays small in the region of low velocity behind the slit. For $v_s = 0.4\,\mathrm{m/s}$, the bulk velocity and volume fraction fields are homogeneous apart from the close vicinity of the slit.

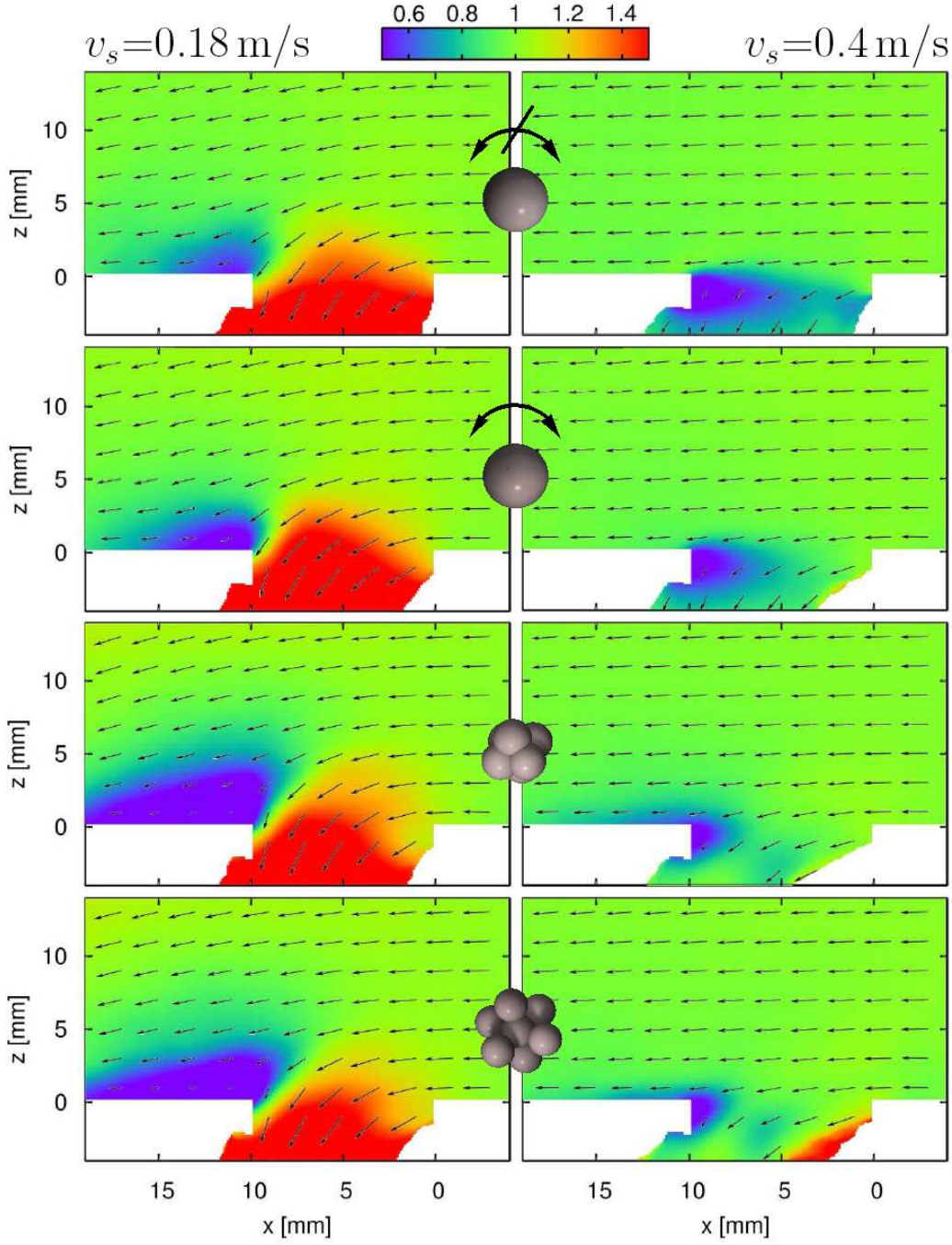

Figure 4.12: Velocity fields for outflow through the $D = 10\,\mathrm{mm}$ slit. The velocity is normalized by the shoe velocity. The standard deviation of the Gaussian weighting is chosen as $\sigma = 0.5\,\mathrm{mm}$ in order to obtain smooth maps.

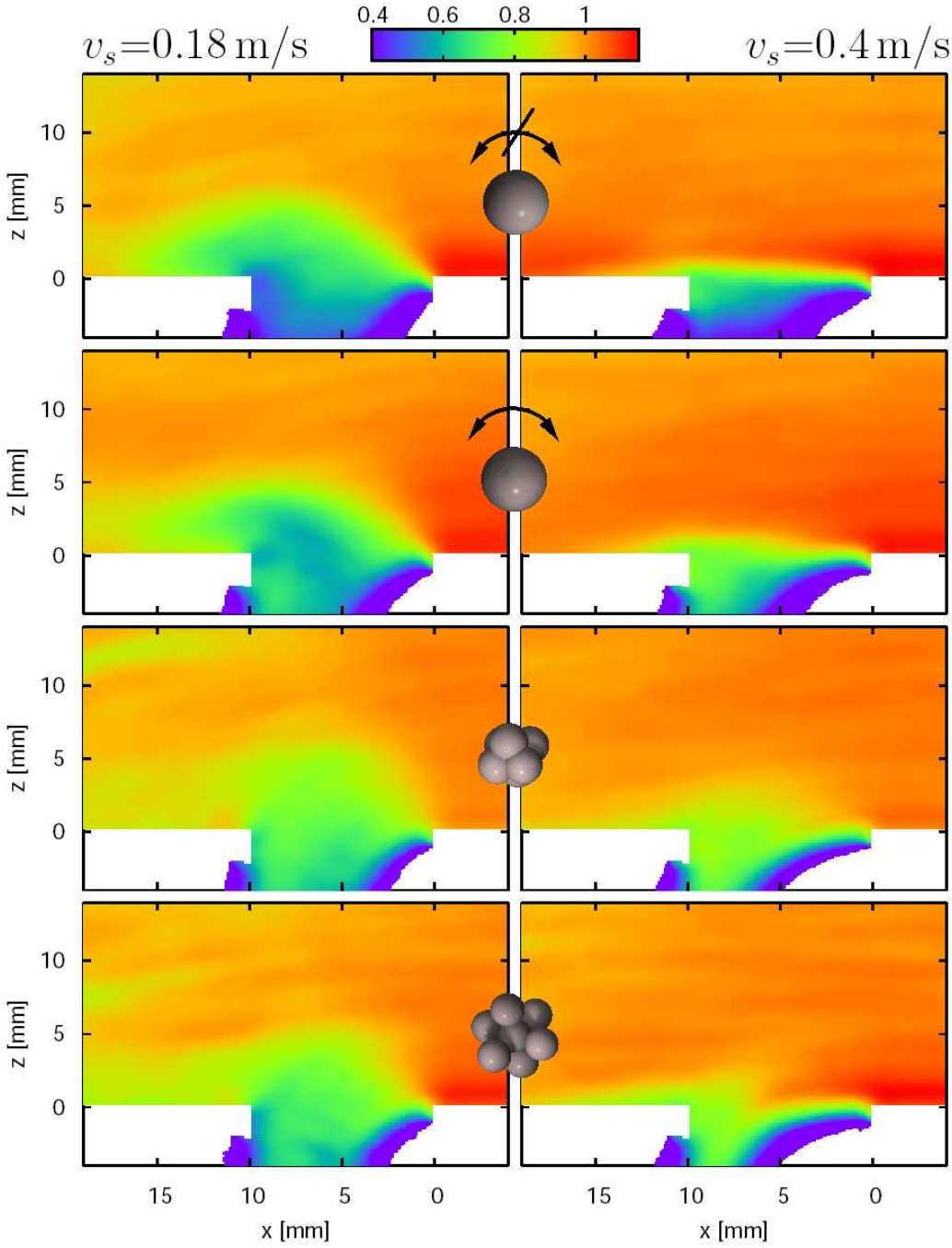

Figure 4.13: Volume fraction fields for the $D = 10\,\mathrm{mm}$ slit. The volume fraction is normalized by the bulk mean value f_m of each model. $\sigma = 0.5\,\mathrm{mm}$.

Setup #	v_s [m/s]	f_m	discharged grains	discharged area [mm^2]
1	0.18	0.322	13982	284
2	0.18	0.323	13660	277
3	0.18	0.323	13928	282
1	0.4	0.322	4383	89
2	0.4	0.323	4346	88

Table 4.5: Volume fraction and slit outflow dependence ($D = 10\,\text{mm}$) on initial random packing using model D2.

4.2 Influence of further model parameters

The tangential spring constant κ_t was not used as a free parameter. It was observed in hopper simulations that either κ_t or μ can be used to adjust the outflow rate within a similar range while the other quantity is kept constant [82]. Therefore it is reasonable to use just one of these two parameters for fitting purposes.

4.2.1 Initial random packing

The influence of statistical variations of the initial spatial grain configuration on simulation results for slit outflow and angle of repose formation was tested. The variations are introduced by using different random offsets for the initial grain positions and different random angular velocities in the setup procedure as described in Section 2.1.6. Table 4.5 shows the results for slit outflow from a moving shoe. The volume fraction f_m is obtained after settling of the grains in the shoe. Its variations in different setups, i.e. with statistically varied initial conditions, are negligible. The number of discharged grains varies within three percent. This value can be understood as a measure for statistical deviations in slit outflow simulations.

The effect of varied initial random packings on angle of repose formation is presented in Table 4.6. The outflow angle of repose θ_O appears to be independent of the actual packing. In contrast, the heap angle of repose is sensitive to statistical variations in the initial packing. This observation correlates with the larger experimental error in the measurement of θ_H compared to θ_O.

4.2.2 Young's modulus

An intrinsic difficulty in modeling metal powders is given by the high Young's modulus. Typical values are 70 GPa for aluminum, 200 GPa for iron and up to 650 GPa for tungsten carbide. For stable and reproducible DEM simulations a collision between two particles has to be sampled over several timesteps [49]. Because the

Setup #	d [mm]	θ_O [°]	θ_H [°]
1	0.94	37	37
2	0.94	37	41
3	1.88	32	—
4	1.88	32	—

Table 4.6: Dependence of outflow and heap angles of repose on initial random packing using model D2).

collision duration decreases with increasing $\tilde{E}$, simulations using realistic Young's moduli are restricted to either short simulated times or small particle numbers. The real time to be simulated is defined by the process (e.g. a few seconds for die filling). In how far the particle number can be reduced by coarse graining is discussed in Section 3. As this is only possible within a certain range, the only way to simulate large systems even with present day computer clusters is via artificial reduction of the Young's moduli of the particles. Of course, this modification is only legitimate if it does not affect the results. DEM simulations of granular flow on inclined planes reveal that the Young's modulus can be chosen about five orders of magnitude lower than the real value without affecting volume fractions and velocity profiles [71]. It was observed in previous particle packing simulations that a realistic value of $\tilde{E}$ is important only if an external pressure is applied [83]. However, in the setups used in the present thesis the situation is different, because the main pressure acting on the grains results from the weight of the grains above and its magnitude is negligible, i.e. in the order of 100 Pa. In this work the value of $\tilde{E}$ is chosen about four orders of magnitude lower than the value for iron. Tests of the influence of $\tilde{E}$ on volume fractions and slit discharge are presented in the following.

Figure 4.14a shows the dependency of height resolved volume fractions on $\tilde{E}$ after settling of grains in a feeding shoe. Up to choosing $\tilde{E}$ four orders of magnitude lower than in reality only a slight increase in the volume fraction is found. However, when choosing $\tilde{E}$ six orders of magnitude lower the volume fraction increases dramatically. In addition, the density profile shows an unrealistic height dependency.

Slit outflow simulations with varied $\tilde{E}$ are summarized in Table 4.7. Using $\tilde{E} \geq 10^9$ Pa deviations in the discharged grain number are comparable to statictical effects (see Section 4.2.1). For $\tilde{E} = 10^7$ Pa both the volume fraction and discharged grain number increase which leaves the discharged area unaffected. Thus, this choice of the stiffness of the grains is legitimate. Only when applying $\tilde{E} = 10^5$ Pa the discharged particle number increases dramatically. As all other simulations throughout the thesis are carried out using $\tilde{E} \approx 10^7$ Pa, the obtained flow rates and volume fraction results are representative for real iron within an error of a few

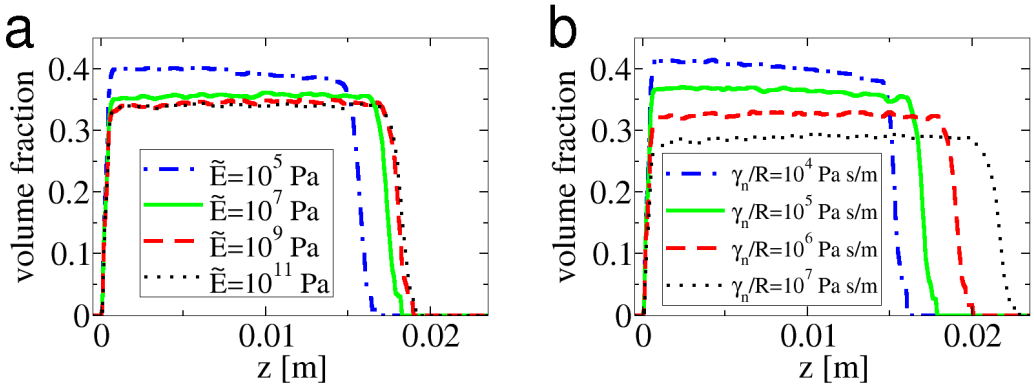

Figure 4.14: Influence of (a) Young's modulus and (b) dissipative parameter on volume fraction. Model D with $\mu = 0.5$ and $w = 0\,\mathrm{J/m^2}$ was used for the variation of $\tilde{E}$ and model D2 for the variation of γ_n.

$\tilde{E}$ [Pa]	f_m	discharged grains	discharged area [mm^2]
10^5	(0.39)	2441	(41)
10^7	0.36	1476	25
10^9	0.34	1319	25
10^{11}	0.34	1377	27

Table 4.7: Slit discharge dependency on $\tilde{E}$ (model D, $d = 0.47\,\mathrm{mm}$, $v_\mathrm{s} = 0.6\,\mathrm{m/s}$, $D = 6\,\mathrm{mm}$). The values of f_m are obtained from fits to Fig. 4.14a. Therefore, only a rough value can be given for $\tilde{E} = 10^5\,\mathrm{Pa}$. Model D, $\mu = 0.5$, $w = 0\,\mathrm{J/m^2}$.

percent.

Increasing the work of adhesion per unit contact area, w, decreases the flowability of the grains. To obtain a certain flowability, w is adjusted depending on $\tilde{E}$, as the latter influences the actual contact area due to surface deformation of the grains. The dependency is not trivial. This fact has to be considered when comparing values of w given in this thesis to experimentally measured cohesive energies.

4.2.3 Dissipative constant

The dissipative constant γ_n controls the amount of kinetic energy which is dissipated during an inelastic collision of two grains. Its value was not varied or fitted during the fitting and validation procedures. In this section the influence of the variation of γ_n on various investigated properties is addressed.

γ_n/R [Pa s/m]	f_m	discharged grains	discharged area [mm^2]
10^4	0.41	14629	234
10^5	0.37	14239	252
10^6	0.32	13928	285
10^7	0.28	12417	290

Table 4.8: Slit discharge dependence on γ_n/R. Model D2, $v_s = 0.18\,\mathrm{m/s}$, $D = 10\,\mathrm{mm}$.

γ_n/R [Pa s/m]	θ_O [°]	θ_H [°]
10^5	38	38
10^6	37	37
10^7	37	37

Table 4.9: Dependence of outflow and heap angles of repose on γ_n/R. Model D2, $d = 940\,\mu\mathrm{m}$.

Volume fractions decrease with increasing γ_n/R which is tested during the formation of an initial distribution from previously free floating particles without contacts (see Fig. 4.14b). This effect was already observed by Silbert *et al.* [84]. Stronger inelastic collisions yield a less dense packing as the grains undergo less collisions and are more likely to come to rest while forming a more porous network.

Table 4.8 gives a summary of outflow simulations through the $D = 10\,\mathrm{mm}$ slit at a shoe velocity of $0.18\,\mathrm{m/s}$. Note that the dependency of the total number of discharged grains is only weakly dependent on γ_n/R while the dependency of the volume fraction f_m is stronger. This leads to different values in the discharged area which is evaluated according to Eq. (4.2). For strong dissipation, i.e. $\gamma_n/R \geq 10^6\,\mathrm{Pa\,s/m}$, flow rates and volume fractions depend likewise on γ_n/R and, thus, the discharged area is nearly constant. Angles of repose are only marginally affected by a variation of γ_n/R which is denoted in Table 4.9. Therefore, it was reasonable not to include γ_n in the fitting procedure.

The results of the model fitting and validation procedure are not substantially affected by the choice of γ_n/R with the exception of an overall shift in volume fraction. Yet, a decrease from 10^6 to $10^5\,\mathrm{Pa\,s/m}$ would improve model D2, because the volume fraction of 0.37 is closer to the experimental value of 0.38 for ASC100.29. A lower amount of discharged area in slit outflow is in better agreement with the experiment, too.

A direct experimental measurement of γ_n via binary collisions is problematic due to the irregular grain morphology which yields complicated impact events where a substantial amount of translational kinetic energy can be transformed into rota-

tional kinetic energy [85]. However such a procedure can be carried out for spherical particles [56].

4.2.4 Effective wall friction

Confining walls are formed by spheres positioned on a grid as described in Section 2.1.5. Thus, a wall is not perfectly smooth. The influence of the surface roughness and the microscopic friction coefficient μ_w on an effective wall friction was assessed by a setup as depicted in Fig. 4.15. A normal force f_n is applied on the green lid which is moved at constant velocity v to the right. The blue powder is sheared against the red wall due to the vertical blade which is rigidly connected to the lid. The setup is periodic both in the direction of lid movement and perpendicular to it. The shear force f_t which is necessary for the movement of the lid is measured. An effective wall friction coefficient is then calculated via

$$\mu_{w,eff} = \frac{f_t}{f_n}. \tag{4.5}$$

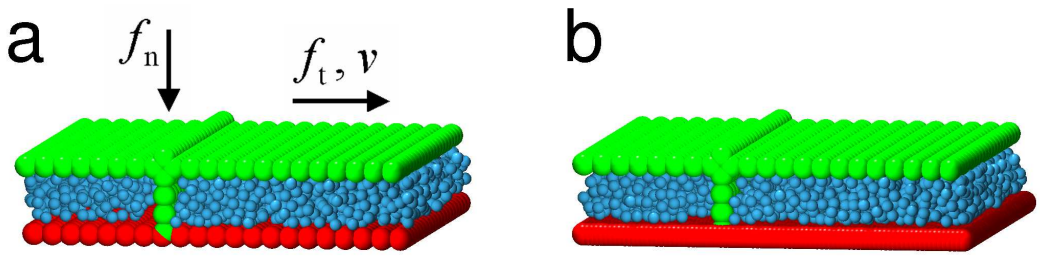

Figure 4.15: Simulation setup for determining the effective friction of the red wall. The wall is apparently rough for a grid spacing of $1.6\,R_w$ (a) while it is smooth for $0.4\,R_w$ (b).

In a series of simulations the wall grid spacing was varied between $0.4\,R_w$ and $1.6\,R_w$ while μ_w ranges from 0.01 to 0.5. For each combination of grid spacing and μ_w two values of the normal force (0.025 N and 0.125 N) and two velocities (0.1 m/s and 0.5 m/s) were applied in subsequent simulations. The normal force corresponds to a pressure of 1 kPa and 5 kPa, respectively. Powder model D2 ($d = 470\,\mu$m) was used for the simulations. Figure 4.16 presents the obtained results. The data points are the mean values of the four measurements, i.e. each combination of normal force and lid velocity, while the error bars represent the standard deviations. For each grid spacing, $\mu_{w,eff}$ depends linearly on the microscopic wall friction coefficient with a slope of about one. An increase in grid spacing raises the wall roughness and, thereby, the effective friction. The ratio of the radius of the wall spheres and

μ_w	grid spacing $[R_w]$	$\mu_{w,eff}$	f_m	discharged grains	discharged area [mm^2]
0.15	0.4	0.16	0.32	14146	289
0.05	1.6	0.17	0.32	13665	279
0.15	0.8	0.18	0.32	13948	285
0.15	1.6	0.28	0.32	13660	279
0.25	1.6	0.38	0.32	14154	289

Table 4.10: Slit discharge is independent of the effective wall friction. Model D2, $v_s = 0.18\,\mathrm{m/s}$, $D = 10\,\mathrm{mm}$.

the basic spheres of the powder grains is about 2 in the presented simulations. Presumably $\mu_{w,eff}$ is a monotonically increasing function of this ratio as the surface roughness increases with respect to the basic sphere size. However, this is not explicitly tested. In order to adjust $\mu_{w,eff}$ for a given real wall material, shear cell experiments in a similar setup [86, 87] can be carried out.

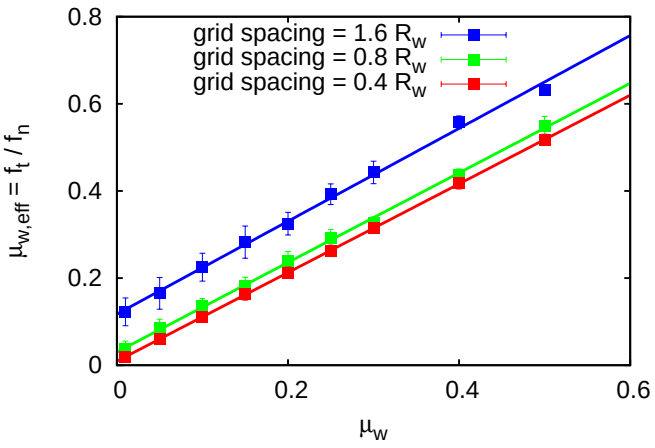

Figure 4.16: Dependence of effective wall friction $\mu_{w,eff}$ on wall friction coefficient μ_w and wall grid spacing.

The influence of the effective wall friction on slit outflow and angle of repose simulations was tested. The results for outflow through a slit are shown in Table 4.10. No systematic trend of the discharged particle number on $\mu_{w,eff}$ is observed. The magnitude of the variations is of statistical nature (compare Section 4.2.1). Angles of repose are not affected by the effective wall friction, too, unless the wall is very smooth in which case it cannot support the lowest layer of the heap.

4.3 Conclusion

The properties of ASC100.29 powder are described qualitatively well in both, static (angle of repose) and dynamic (slit discharge) regimes by DEM grain model D if an adequate parameterization is used. None of the remaining tested models is capable of that. In particular, spherical grain models with rotational degrees of freedom fail completely in reproducing realistic angles of repose. In addition, model D yields very good predictions for the filling behavior of a circular cavity.

The strength of model D is apparently caused by its morphology, because the inadequate model C differs from model D only in grain shape. Model D features a rugged surface just as ASC100.29, although the ratio of the size of the asperities (i.e. the basic spheres for model D) to grain diameter is considerably larger for model D than for ASC100.29 (compare Fig. 4.1). On the one hand, the asperities allow for mutual support of the grains via interlocking. Thus, they contribute to the shape of a granular heap, i.e. the angle of repose. On the other hand, the asperities form barriers which hinder the release of grains from the bulk. Thereby, they influence discharge rates of the powder. A modified grain model with a slightly higher degree of sphericity than model D should be able to cover the behavior of ASC100.29 quantitatively in both situations, i.e. heap formation and outflow, with a single parameterization.

The DEM force law parameters which strongly influence static and dynamic characteristics of the granular medium are the friction coefficient, μ, and the work of adhesion, w. Yet, the actual grain shape is of comparable importance. An improved procedure for parameter adjustment could be the following. A morphology parameter could be defined as the ratio of the diameter of the constituent basic spheres to the diameter of the composed grain. A starting value for this parameter is set via optical analysis of the real grains. Then μ, w and the morphology parameter are adjusted by a gradient based optimization technique using powder discharge, angle of repose, and volume fraction as target values. The results of this chapter indicate that a suchlike adjusted model yields reliable informations on flow and filling behavior even in setups which differ significantly from those used for the adjustment.

A method was presented for the determination of an effective wall friction coefficient within the DEM simulations. This quantity depends on the geometric roughness of the wall which was formed by particles and the microscopic friction coefficient of these particles. However, it was found that the effective wall friction coefficient has no influence on the behavior of the model powders in the studied setups.

5 Continuum description and analytic expressions for granular outflow

A comprehensive theoretical framework for rapid granular flow is not yet discovered. In this chapter granular flow through slit orifices from an immobile hopper or a moving shoe, respectively, is analyzed. The improvement of theoretical models for velocity profiles and the integral mass flow rate motivates these investigations. A brief overview of existing models for these regimes is given in the following.

Several experimental and numerical analyses of granular flow down an inclined plane have been carried out (see e.g. Refs. [88, 71, 89, 90, 91, 92, 93, 94]). A recent success is the description of this system by means of the incompressible Navier-Stokes equations using a constitutive law which relates the viscosity to the local stress, shear rate, and particle size [25]. However, this model is not valid for high inclinations of the plane and is not transferable to vertical granular flow which occurs inside a hopper. A significant difference between the inclined plane and the hopper flow regime exists in the stress distribution. On the inclined plane the compressive stress increases steadily from the surface on downwards due to the weight of the grains. In contrast, discontinuities in the stress field are characteristic for a hopper geometry [95]. Yet, the observed velocity profiles are continuous in both systems [96, 97, 25]. Because of this fundamental difference between stress and velocity, a Navier-Stokes description of the hopper velocity field cannot be based on a constitutive law which takes the local stress into account [43].

Kinematic modeling (KM) [98, 99, 43] is a continuum description for velocity fields in a discharging hopper. The model is comparably simple as it requires only a single fitting parameter. However, measured velocity fields can only be described with moderate accuracy unless the fitting parameter is varied with height [100, 96]. Details of KM are given in Section 5.1.2.

The recently introduced *spot model* for granular flow considers collective displacements of grains as a response to the motion of spots, i.e. zones of lowered volume fraction [101, 102]. The spots enter a hopper at the orifice and drift upward, opposite to gravity, while diffusing horizontally. This model describes profiles of the vertical velocity component adequately [103]. No data has yet been published on the predictive power of the model for the horizontal velocity component.

The Beverloo equation [20] constitutes an early success in describing granular discharge on a less detailed level: The mass flow rate W of a powder with apparent density ρ_a from a flat-bottomed hopper through a circular orifice with diameter D_0 caused by the gravitational acceleration g can be expressed as

$$W = C\rho_\mathrm{a}\sqrt{g}D_0^{5/2}, \tag{5.1}$$

where C is a dimensionless constant. Note the difference between Eq. (5.1) and Torricelli's law for a liquid with density ρ_l flowing through an orifice located at a distance h_0 below the surface of the liquid: $\tilde{W} \propto \rho_\mathrm{l}\sqrt{gh_0}D_0^2$.

Inroads were made into expressing the mass flow rate through an orifice from a feeding shoe which is moving at a velocity v_s based on Eq. (5.1) [74, 29]. Thereby, the constant C is substituted by a shoe-velocity-dependent term, $C(v_\mathrm{s}) \propto v_\mathrm{s}^p$, with $p \approx -1/5$. Although experimental and numerical data could be fitted by using this model [75, 76, 104], the divergence of $C(v_\mathrm{s})$ at $v_\mathrm{s} \to 0$ is obviously invalid.

5.1 Continuum description of velocity distributions

DEM simulations were used to obtain detailed velocity and volume fraction distributions of a granular material which discharges from a hopper. Thereby, the focus was on the spatial vicinity of the slit orifice, in contrast to several previous studies which concentrated on regions farther from the orifice. The kinematic modeling approach was applied in order to describe the velocity profiles. Shortcomings of this method are pointed out. An extension of the kinematic modeling picture was derived, which takes volume fraction variations within the granular material into account. It is demonstrated, that this extended continuum model is able do reproduce the DEM velocity profiles at a high level of detail.

5.1.1 DEM simulations

The setup shown in Fig. 5.1 was used for the granular discharge simulations. DEM model D was used with grain diameter $d = 470\,\mu$m, friction coefficient $\mu = 0.5$, and without cohesion ($w = 0\,\mathrm{J/m^2}$). The remaining simulation parameters are listed in Table C.5. Periodic boundary conditions were used along the y-axis with a simulation box length of about $4.5\,d$. Thus, discharge through an infinitely long slit is resembled by the simulations. The upper panel of Fig. 5.2 displays stationary distributions of the vertical (v_z) and the horizontal velocity component (v_x), respectively. The slit width is $D = 15\,$mm and the hopper width is $l = 45\,$mm. The smoothness of the distributions was achieved via both, time averaging and ensemble averaging. Up to ten simulations with statistically varied initial particle positions and orientations ware used for the ensemble averaging. The filling height of the hopper decreased from about 65 mm to about 50 mm during the time averaging.

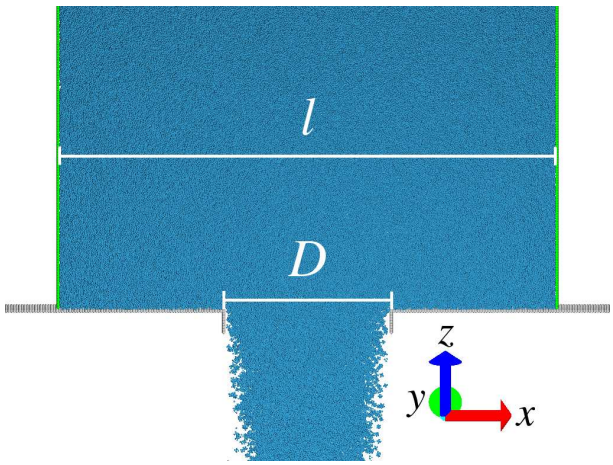

Figure 5.1: Simulation setup for granular outflow from a hopper. The center of the slit orifice is located at at $(x = 0, z = 0)$. The simulation box is periodic along the y-axis.

A typical feature of the vertical velocity component is the rapid broadening of the distribution with respect to height. This behavior reflects the so-called *mass flow* regime which occurs for granular materials without strong friction and cohesion. In contrast, the discharge of very cohesive grains would be governed by the *core flow* regime, i.e. the material is only mobilized in a vertical channel above the orifice corresponding to a narrow velocity distribution even for large heights (several times the slit width) [14]. Both velocity fields are symmetric with respect to the z-axis ($x = 0\,\mathrm{mm}$). The horizontal velocity component vanishes at the axis of symmetry. It also becomes negligible for heights larger than about twice the slit width. Typical is the kidney-shaped appearance of the v_x-field. The maximum magnitudes of v_z and v_x differ by a factor of about 6, i.e. the grains move mainly along the direction of gravitational acceleration. These velocity fields are used as benchmarks for continuum descriptions presented in the following.

5.1.2 Kinematic modeling

The kinematic modeling picture of stationary granular flow inside a discharging hopper is based upon a simple correlation of the horizontal and the vertical velocity component [98, 99, 43]. Figure 5.3 depicts a schematic of the assumed process: A gradient in the vertical velocity components of two adjacent grains (1 and 2) influences the horizontal velocity component of a grain above (3) as it will move into the void left by the faster falling grain (2). The term *kinematic* is adequate, because no forces or stresses are included in this model. The idea is expressed in

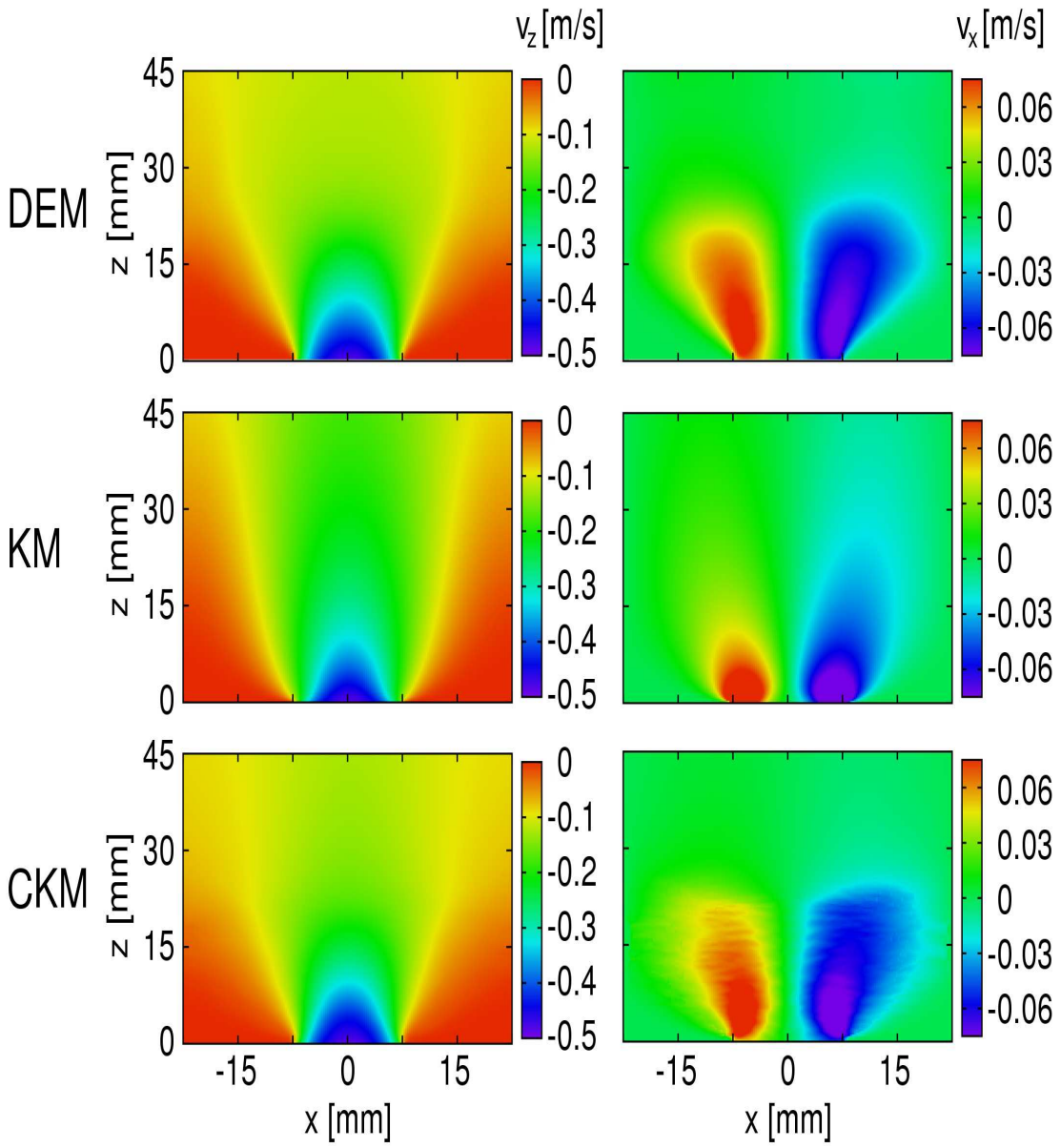

Figure 5.2: Color coded stationary velocity fields. Upper panel: DEM simulations. Middle panel: Kinematic modeling (Eq. (5.4)) using $B = 1.8\,\mathrm{mm}$. Lower panel: Compressible kinematic modeling (Eq. (5.9)).

the mathematically most simple form as

$$v_x = -B\frac{\partial v_z}{\partial x} \tag{5.2}$$

where B is a parameter with the unit of length. Furthermore, the granular material is assumed to be incompressible,

$$\frac{\partial v_x}{\partial x} + \frac{\partial v_z}{\partial z} = 0. \tag{5.3}$$

The combination of Eqs. (5.2) and (5.3) yields a linear partial differential equation for the vertical velocity component,

$$\frac{\partial v_z}{\partial z} = B\frac{\partial^2 v_z}{\partial x^2}. \tag{5.4}$$

The parameter B is sometimes denoted as a *diffusion length* because Eq. (5.4) has the form of a diffusion equation for the vertical velocity component [99, 43]. However, in this work it will be simply referred to as the KM parameter.

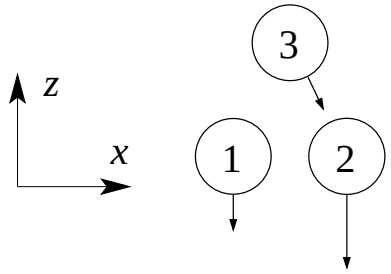

Figure 5.3: Schematic of the idea upon which the kinematic modeling for granular outflow is based (adapted from Ref. [43]). The higher vertical velocity of grain 2 compared to grain 1 causes grain 3 to move to the right.

The vertical velocity component vanishes at the ground walls of the hopper and the horizontal component at the side walls, i.e. $\partial v_z/\partial x = 0$ due to Eq. (5.2). Equation (5.4) can be solved analytically for the boundary condition of a constant vertical velocity along the slit orifice [14]. However, this is a strong simplification. In the present work the partial differential equation (5.4) was solved numerically via finite differences on a staggered grid (see Appendix B). Thereby, the vertical velocity as observed in the DEM simulations was used as boundary condition at the orifice. The resulting velocity distributions for a choice of $B = 1.8\,\mathrm{mm}$ are displayed in the middle panel of Fig. 5.2. The value of B was adjusted such that the basic features found in the DEM simulations are described by the kinematic modeling. Yet, the agreement is not particularly good in detail: E.g. the yellow

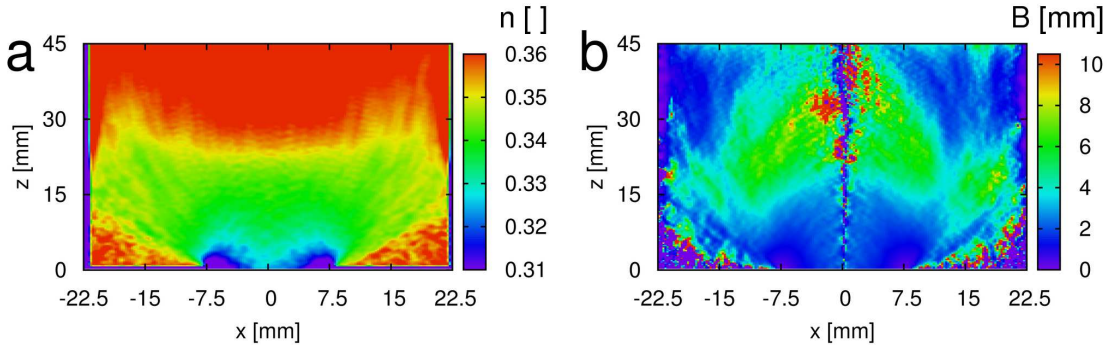

Figure 5.4: Stationary spatial distributions of (a) volume fraction n and (b) KM parameter B for hopper discharge from DEM simulations.

isolines of $v_z \approx -0.1\,\mathrm{m/s}$ are straight in the DEM simulations in the vicinity of the slit while the kinematic modeling predicts them as curved. Deviations between DEM and KM are even more pronounced for the horizontal velocity distributions. It was checked that different choices of B do not provided a better approximation of the DEM data.

5.1.3 Compressible kinematic modeling

It was found that the KM description of measured velocity profiles can be improved by allowing B to increase with z [105, 106, 100, 107, 96]. However, no general rule for the magnitude of B or its dependency on z could be provided. The correlation between B and v_z was analyzed in Ref. [108] with the result that B does not depend monotonically on v_z. A microscopic explanation for this observation was yet not given.

The stationary volume fraction distribution, $n(x, z)$, obtained from the DEM simulations is displayed in Fig. 5.4a. The volume fraction decreases from a height of about 40 mm towards the slit orifice. Above $z = 40\,\mathrm{mm}$ the volume fraction is approximately constant with a bulk value of $n \approx 0.365$. Triangular regions of high volume fraction exist next to the orifice where the granular material remains motionless. Based on the velocity distributions from the DEM simulations, the KM parameter B is evaluated locally via Eq. (5.2). The spatial distribution, $B(x, z)$, is displayed in Fig. 5.4b. The value of B varies over an order of magnitude within the orifice region and depends not only on z but also on x. A visual comparison with the volume fraction distribution suggests some degree of correlation.

The correlation was evaluated locally at the nodes of a rectangular grid with an edge length of 0.25 mm. Figure 5.5 depicts the correlation as clouds of points, each point representing a grid node. In Fig. 5.5a only those nodes are considered

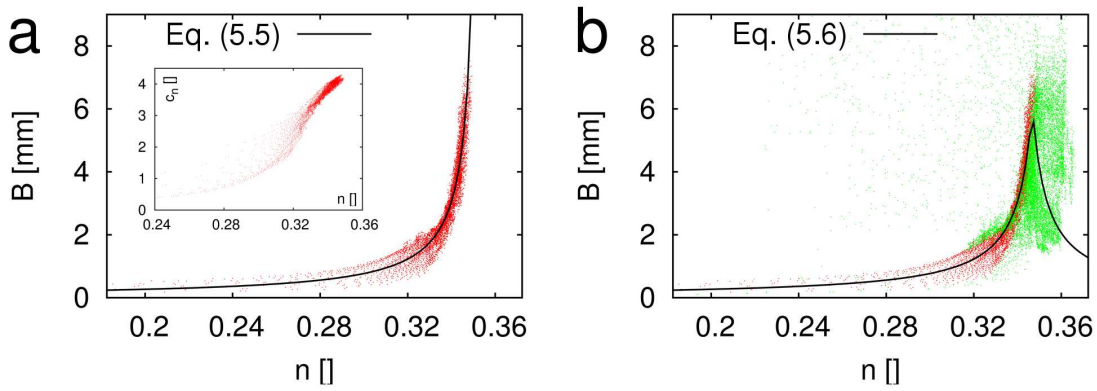

Figure 5.5: KM parameter B as a function of the volume fraction. Restrictions of data evaluation: (a): $|v_x| > 0.038\,\mathrm{m/s}$; (b): red means $|v_x| > 0.038\,\mathrm{m/s}$ and green means $0.008\,\mathrm{m/s} < |v_x| < 0.038\,\mathrm{m/s}$. Inset in (a): Coordination number c_n as a function of the volume fraction.

where $|v_x| > 0.038\,\mathrm{m/s}$, i.e. velocities greater than half the maximum horizontal velocity. In Fig. 5.5b the data from all nodes with $|v_x| > 0.008\,\mathrm{m/s}$ is drawn. The nodes with $|v_x| < 0.008\,\mathrm{m/s}$ are not taken into account, because B cannot be evaluated properly in this case (see e.g. the noise along the axis of symmetry where v_x vanishes in Fig. 5.4b). A monotonic dependency is found when plotting B against the volume fraction for $|v_x| > 0.038\,\mathrm{m/s}$ (see Fig. 5.5a). The correlation can be described by a simple power law,

$$B(n) = \frac{B_0}{1 - n/n_\mathrm{div}}, \tag{5.5}$$

with fitted parameters $B_0 = 0.116\,\mathrm{mm}$ and $n_\mathrm{div} = 0.353$. The inset of Fig. 5.5a shows the coordination number c_n as a function of the volume fraction. At low volume fractions there are less contacts between the grains than at high volume fractions. Hence, the degree of interaction between the grains increases with n. The increase of B with n can then be understood by recalling the idea of KM (Fig. 5.3): If there is only little interaction between the grains, the existence of a horizontal gradient in v_z will have little influence on the horizontal grain movement. In a denser region the influence is larger, because the motion of each grain is stronger correlated with the motion of the surrounding grains.

The dependence of B on n becomes ambiguous at high volume fractions if smaller horizontal velocities are also taken into account (Fig. 5.5b). However, an attempt was made to find an expression $B(n)$ even for high volume fractions. Clearly, B does not diverge. On the contrary, there is a dense branch of data points indicating a decrease of B in average towards high volume fractions. Thus, a simple approach

in order to approximate the complete data set was done by mirroring the power law at $n_{\mathrm{peak}} = 0.347$ which is about 95 % of the observed maximum volume fraction,

$$B(n) = \frac{B_0}{1 - n/n_{\mathrm{div}}}\Theta(n_{\mathrm{peak}} - n) + \frac{B_0}{1 + (n - 2n_{\mathrm{peak}})/n_{\mathrm{div}}}\Theta(n - n_{\mathrm{peak}}), \quad (5.6)$$

where $\Theta(n)$ is the Heaviside step function.

This finding suggests a modification of the kinematic modeling by considering the KM parameter as a material specific function of the volume fraction, $B(n)$. Thus, Eq. (5.2) turns into

$$v_x = -B(n)\frac{\partial v_z}{\partial x}, \quad (5.7)$$

and Eq. (5.3) is replaced by the compressible continuity equation,

$$\frac{\partial (n v_x)}{\partial x} + \frac{\partial (n v_z)}{\partial z} = 0. \quad (5.8)$$

The combination of Eqs. (5.7) and (5.8) yields

$$\begin{aligned} 0 &= \frac{\partial}{\partial x}\left(B(n) n \frac{\partial v_z}{\partial x}\right) - \frac{\partial (n v_z)}{\partial z} \\ &= \left(n\frac{\partial B(n)}{\partial n} + B(n)\right)\frac{\partial n}{\partial x}\frac{\partial v_z}{\partial x} + B(n) n \frac{\partial^2 v_z}{\partial x^2} - n\frac{\partial v_z}{\partial z} - v_z \frac{\partial n}{\partial z}. \end{aligned} \quad (5.9)$$

Equation (5.9) for itself constitutes an under-determined problem for the two independent variabes n and v_z. However, its predictive quality for the velocity distributions can be assessed by using the volume fraction distribution $n(x, z)$ obtained from the DEM simulations as fixed input quantity. The set of Eqs. (5.7) and (5.9) in combination with an expression for $B(n)$ is from now on referred to as *compressible kinematic modeling* (CKM). Equation (5.6) is used to model $B(n)$.

The CKM partial differential equations were solved numerically as described in Appendix B. The lower panel of Fig. 5.2 shows the obtained velocity distributions. Apparently, there is strong agreement with the DEM results. All features which could not be reproduced by the KM are yet present in the CKM distributions. A more detailed comparison of these two continuum descriptions with the DEM data is given in Fig. 5.6. The CKM and DEM results are nearly identical except for some slight deviations in the horizontal velocity component at small heights. In contrast, the deviations between KM and DEM are pronounced in both velocity components.

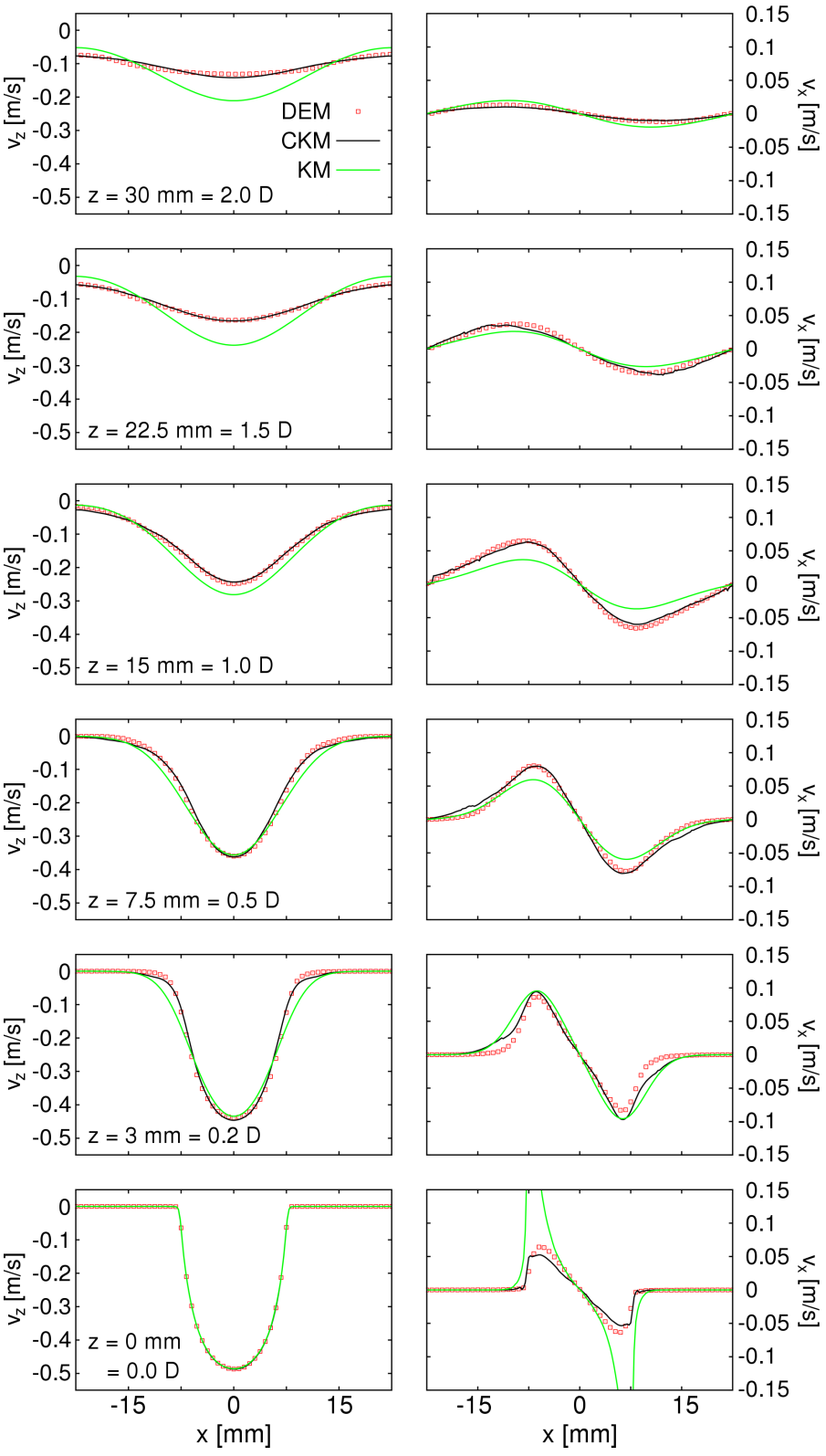

Figure 5.6: Comparison of velocity profiles from DEM, CKM, and KM at six different heights.

Setup #	D [mm]	g [m/s^2]	d [μm]	l [mm]
1	15	9.81	470	45
2	10	9.81	470	45
3	15	1.62	470	45
4	15	9.81	940	45
5	15	9.81	470	60

Table 5.1: Varied parameters for DEM hopper discharge simulations.

5.1.4 Scaling properties

The scaling behavior of granular outflow in the vicinity of the orifice with respect to length and time scales is assessed in this section. Therefore, further simulations were carried out with variations of slit width D, gravity acceleration g, grain diameter d, and hopper width l, in addition to the DEM setup described in Section 5.1.1. Table 5.1 gives an overview of the varied parameters for all setups. Note that the coarse graining scheme (Chapter 3) was not applied for the varied grain size in setup 4 in order to explicitly investigate grain size related effects.

Figure 5.7 displays profiles of both velocity components and the volume fraction for all setups. The distributions are normalized by the length scale D and the velocity scale $\sqrt{gD}$, i.e. the time scale is $\sqrt{D/g}$. This particular scaling for granular flow rates through an orifice was introduced by Beverloo *et al.* [20] and is generally accepted [14]. Note that the grain size does not define the length scale. A data collapse of v_z and v_x is observed close to the orifice, i.e. $z \leq 0.5D$. For $z \geq D$ pronounced deviations of setups 2 and 5 in comparison to the remaining setups exist. The reason is that the velocity scale at large heights is $\sqrt{gD^3}/l$ due to continuity [14, 100]. Thus, only setups 1, 3, and 4 collapse at all heights when normalizing the velocity via $\sqrt{gD}$.

The volume fraction profiles at $z = D$ collapse within the data noise. For $z \leq 0.5D$ the volume fraction in setups 2 and 4 is lower than in the remaining setups within a corridor above the orifice, i.e. $0 \lesssim x \lesssim D$. This observation reflects the effect of lowered volume fraction of a granular material close to a boundary (compare Figs. 2.5 and 3.3). The larger the ratio d/D the more pronounced is this effect with respect to D. At large heights ($z \geq 1.5D$) the deviations of setup 2 and 5 can again be explained by inadequate normalization, i.e. the z-coordinate cannot only scale with D but must also be a function of l. Yet, it remains unclear why setup 3 with altered gravitational acceleration differs from setup 1.

The scaling collapses of both the velocity and the volume fraction distributions (apart from the boundary effect) in the vicinity of the orifice suggest that $B(n)$ can

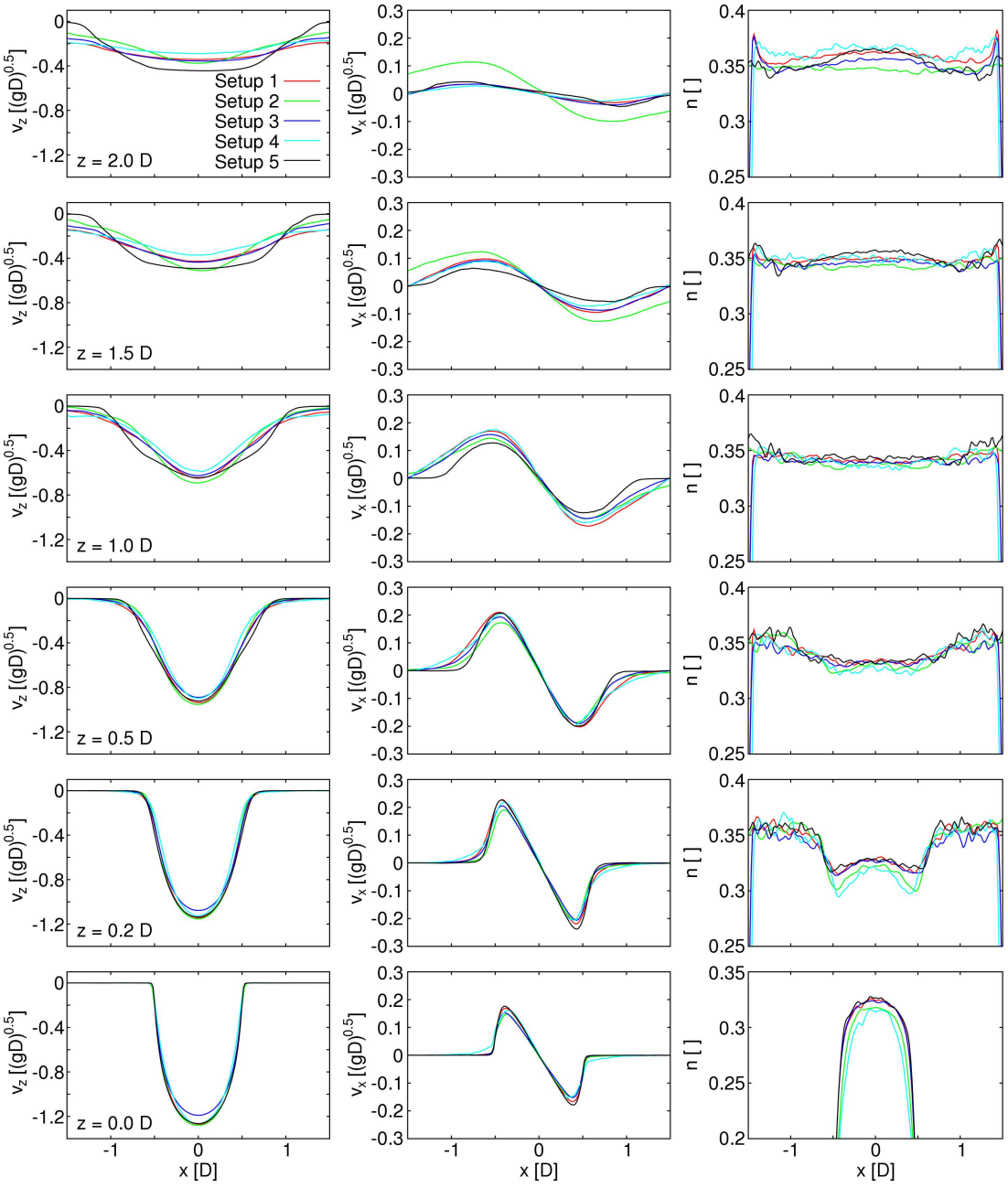

Figure 5.7: Velocity and volume fraction profiles at certain normalized heights, z/D, from DEM simulations with varied length-scales and time-scales (compare Table 5.1).

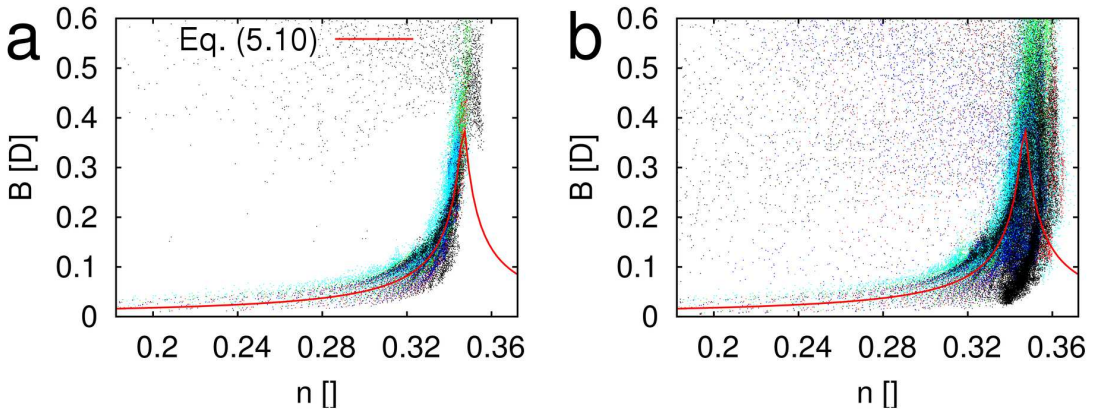

Figure 5.8: Evaluation of $B(n)$ for all tested setups. The color coding of the point clouds is in accordance with Fig. 5.7. Restrictions of data evaluation: (a): $|v_x| > 0.1\sqrt{gD}$; (b): $|v_x| > 0.02\sqrt{gD}$.

be normalized by D,

$$B(n) = \frac{\nu D}{1 - n/n_{\mathrm{div}}}\Theta(n_{\mathrm{peak}} - n) + \frac{\nu D}{1 + (n - 2n_{\mathrm{peak}})/n_{\mathrm{div}}}\Theta(n - n_{\mathrm{peak}}). \quad (5.10)$$

The comparison with Eq. (5.6) yields $\nu = B_0/15\,\mathrm{mm} = 0.0077$. Figure 5.8a shows the locally evaluated $B(n)$ for all setups under the restriction of $|v_x| > 0.1\sqrt{gD}$, i.e. $|v_x| > 0.038\,\mathrm{m/s}$ for $D = 15\,\mathrm{mm}$. The data points collapse and, thus, the left branch of Eq. (5.10) provides a valid description. The right branch of Eq. (5.10) cannot be justified by the present simulations (see Fig. 5.8b). Thus, it should only be understood as a necessary extension of $B(n)$ for $n > n_{\mathrm{peak}}$ in order to solve the CKM problem numerically. The point clouds in Fig. 5.8 are more noisy compared to Fig. 5.5, because 5 statistically different simulations were used for the ensemble averaging for setups 2 to 5 while 10 were used for setup 1.

The scaling behavior $B \propto D$ is validated in Fig. 5.9. The CKM equations were solved for setups 1 and 2 using the respective volume fraction fields $n(x, z)$ from the DEM simulations and the universal function $B(n)$ as defined in Eq. (5.10). The distinct features of both setups are reproduced by the continuum description. In summary, it seems justified to understand $B(n)$ as a general relationship within the scope of the introduced CKM for the used grain model in the flat-bottomed hopper geometry. Thus, the parameter ν and perhaps even the functional form of $B(n)$ could depend on both, the actual hopper shape as well as morphologic and mechanic properties of the grains.

The independency of B on grain diameter d requires some discussion. Velocity profiles from several experiments [105, 106, 107] were fitted using KM with the

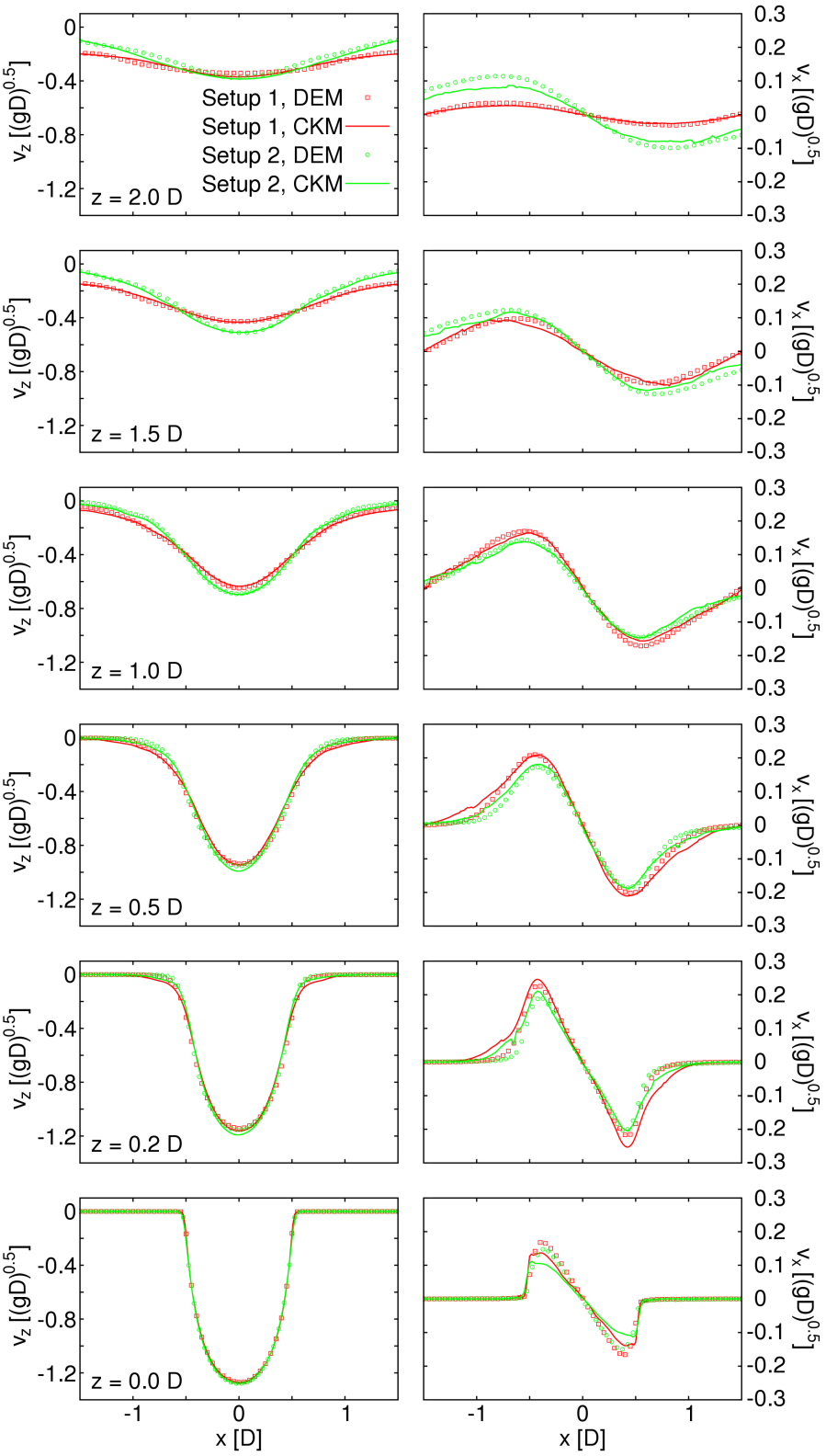

Figure 5.9: Velocity profiles from DEM and CKM for setup 1 ($D = 15\,\mathrm{mm}$) and setup 2 ($D = 10\,\mathrm{mm}$).

outcome of a linear dependency, $B/d = s$, with s varying from 1 to 3 for the different studies. This finding was not confirmed by the present work where the velocity distributions coincide for varied grain size. The contradicting results might be explained as follows. The experiments did not focus on the region close to the orifice, but rather on vertical coordinates equal to several times the orifice width. In addition, analytic solutions of Eq. (5.4) were used with a fixed volume flow rate at a point orifice as boundary condition. Thus, flow details in the vicinity of the orifice are neglected. Apparently, the flow regime close to the orifice differs fundamentally from the flow regime in sufficient distance from the orifice, i.e. at least a few times D away [99]. Velocity profiles seem to be independent of grain size in the dilute zone at the orifice while they are not in regions with high volume fractions, i.e. close to the bulk value. The behavior in the dense regime is consistent with a recently developed constitutive law for granular flow down an inclined plane where the viscosity and, thus, velocity profiles depend on the grain diameter [25].

5.2 Analytic expressions for mass flow rates

Although hopper discharge has been studied experimentally [20, 109, 110, 111, 112, 113, 114, 115] and numerically [116, 117, 118, 82, 70, 41, 115] for a long time, only very little attention has been paid to the onset of outflow immediately after opening the orifice [119]. A time-dependent extension of the Beverloo equation for the initial phase of hopper discharge is derived in this section. A formula for mass discharge from a moving shoe is then obtained from the transient Beverloo equation.

5.2.1 Transient Beverloo equation

The powder mass flow rate $W(t)$ from a hopper through a rectangular opening with edge lengths D and b is given by the expression

$$W(t) = \rho_{\mathrm{a}}\, b\, D\, \bar{u}(t), \tag{5.11}$$

where ρ_{a} is the apparent density and $\bar{u}(t)$ is the average downward velocity at the opening. Let $b \gg D$, which is true for openings with high aspect ratio or simulations with periodic boundary conditions where b is the simulation box size along the periodic dimension. It was observed experimentally that $\bar{u}$ is independent of grain size, hopper width and filling height [20, 109]. Thus the only characteristic length scale of the system is D and the characteristic time scale is $\sqrt{D/g}$. This is in agreement with the findings presented in Section 5.1.4.

Grains moving through the hopper are accelerated due to gravity. Their movement is hindered by collisions with surrounding grains resulting in effective damping. The influence of the collisions is expressed as a viscous term in analogy to the

Langevin equation. Thus, the following equation is proposed to describe the time evolution of the mass flow rate,

$$\frac{\mathrm{d}W}{\mathrm{d}t} = \rho_\mathrm{a}\, b\, D\, \frac{\mathrm{d}\bar{u}}{\mathrm{d}t} = \rho_\mathrm{a}\, b\, D\, (-\lambda\bar{u} + \epsilon g)\,. \tag{5.12}$$

In order to obtain only dimensionless parameters within the equation, the damping coefficient λ is normalized by the characteristic timescale, $\beta = \lambda\sqrt{D/g}$. For long times t the mass flow rate reaches its equilibrium value, $\epsilon\rho_\mathrm{a} bD\sqrt{gD}/\beta$. By introducing $C_\mathrm{F} = \epsilon/\beta$ the well known Beverloo equation for the mass flow rate through a rectangular opening emerges [109],

$$W_\mathrm{eq} = W(t \to \infty) = C_\mathrm{F}\, \rho_\mathrm{a}\, b\, D\, \sqrt{gD}. \tag{5.13}$$

Immediately after opening the hopper, the discharge mechanism is somewhat different from the later stage which is governed by the damped flow regime. The first few granular layers are rapidly pushed out of the hopper thereby releasing the pressure in the outflow region close to the opening. Simultaneously the average coordination number and volume fraction drops in the outflow region. Simulations show that this initial burst occurs on a timescale smaller than $t_0 = \frac{1}{5}\sqrt{D/g}$ which is at least an order of magnitude smaller than the convergence time of the average velocity. The amount of mass being discharged in the burst phase should be proportional to ρ_a, b and D^2. The D^2-dependency is motivated by the fact that the height of the free fall zone above the opening scales linearly with D and thus the height of the powder volume which is bursted out should scale the same way. For mathematical convenience the burst phase is expressed using a Dirac delta function,

$$W\,(t < t_0) = C_\mathrm{B}\, \rho_\mathrm{a}\, b\, D^2\, \delta\left(t - \frac{t_0}{2}\right), \tag{5.14}$$

where C_B is the dimensionless height of the powder volume being bursted out. The complete expression for $W(t)$ is then constructed as the sum of Eq. (5.14) for $t < t_0$ and the time-dependent solution of Eq. (5.12) for $t \geq t_0$:

$$\begin{aligned} W(t) = {} & C_\mathrm{B}\, \rho_\mathrm{a}\, b\, D^2\, \delta\left(t - \frac{t_0}{2}\right) \\ & + \Theta\,(t - t_0)\, C_\mathrm{F}\, \rho_\mathrm{a}\, b\, D\, \sqrt{gD}\left(1 - \left(1 - \frac{C_\mathrm{I}}{C_\mathrm{F}}\right) e^{-\beta(t-t_0)}\right), \end{aligned} \tag{5.15}$$

with a dimensionless initial velocity C_I at $t = t_0$ and the Heaviside step function $\Theta(t)$.

Equation (5.15) is in very good agreement with DEM simulations of hopper outflow as can be seen in Fig. 5.10a. Note that convergence to the equilibrium flow rate happens quite fast in typical system sizes, e.g. $\sqrt{D/g} = 0.03\,\mathrm{s}$ for $D = 10\,\mathrm{mm}$ and the magnitude of β lies in the order of unity. The fit parameters are listed in Table 5.2.

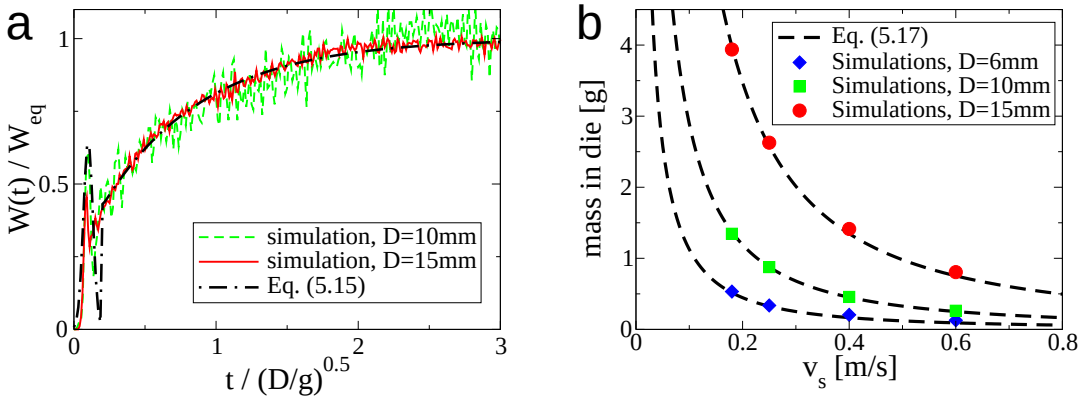

Figure 5.10: (a): Initial hopper discharge with exponential law fit. Note that the burst phase is illustrated using a peak of finite width instead of a delta function. (b): Mass discharge from moving shoe and theoretical prediction. For $D = 15\,\mathrm{mm}$ the shoe was longer ($l = 45\,\mathrm{mm}$) than for the two other cases ($l = 32\,\mathrm{mm}$). Simulation parameters are listed in Table C.5.

C_B	C_I	C_F	β
0.05	0.39	0.92	1.4

Table 5.2: Fitted dimensionless parameters of Eq. (5.15) for hopper discharge DEM simulations.

5.2.2 Mass discharge from moving shoe

The mass discharge from a shoe moving with velocity v_s along the opening edge D is now derived. For this purpose the continuous shoe trajectory is decomposed into a stepped movement, i.e. the shoe is assumed to remain for a time interval D/v_s immobilized while discharging powder. The shoe is then instantaneously displaced by the distance D. Thus the average velocity v_s is conserved. In each step the powder mass above the opening has no initial vertical velocity, because it was placed above the fixed ground just before. So the mass discharge in each step can be calculated by integrating Eq. (5.15),

$$m_\mathrm{step} = \int_0^{D/v_\mathrm{s}} \mathrm{d}t\, W(t). \tag{5.16}$$

A shoe of length l traverses the opening in l/D steps. Therefore the total discharged mass is

$$\begin{aligned} m_\mathrm{B}(v_\mathrm{s}) &= \frac{l}{D} m_\mathrm{step} \\ &= C_\mathrm{B}\,\rho_\mathrm{a}\,b\,D\,l + C_\mathrm{F}\,\rho_\mathrm{a}\,b\,D\,l \\ &\quad \times \left(\frac{\sqrt{gD}}{v_\mathrm{s}} - \frac{1}{5} + \frac{1 - C_\mathrm{I}/C_\mathrm{F}}{\beta} \left(e^{-\beta\left(\frac{\sqrt{gD}}{v_\mathrm{s}} - \frac{1}{5}\right)} - 1 \right) \right). \end{aligned} \tag{5.17}$$

The predictive power of Eq. (5.17) was explored by comparison with simulations of discharge from a continuously moving shoe using the same powder model as in Fig. 5.10a. The agreement between the derived analytic model and the simulations is remarkable (compare Fig. 5.10b) leading to the conclusion that inertial effects in the direction of shoe motion are negligible and, thus, the stepped movement covers essentially the same physical mechanisms as the continuous case.

5.2.3 Experimental validation

The experimental slit discharge system (Fig. 4.2) was used to assess the applicability of Eq. (5.17) for ASC100.29 iron powder (see Fig. 4.1). In addition, comparison was made with an empirical power law expression for mass discharge from a shoe,

$$m_\mathrm{S}(v_\mathrm{s}) = C_\mathrm{S}\,\rho_\mathrm{a}\,D\,b\,l \left(\frac{\sqrt{gD}}{v_\mathrm{s}} \right)^{1+n}, \tag{5.18}$$

as described in Refs. [75, 104]. Figure 5.11a shows the experimental data for a $D = 6\,\mathrm{mm}$ slit and the fits of $m_\mathrm{B}(v_\mathrm{s})$ and $m_\mathrm{S}(v_\mathrm{s})$. The dimensionless fit parameters are summarized in Table 5.3. Equation (5.17) performs better in fitting the data.

The predictions of both formulas are compared with experimental data for a varied slit width ($D = 10\,\mathrm{mm}$) in Fig. 5.11b. Using $m_\mathrm{B}(v_\mathrm{s})$ the general trend

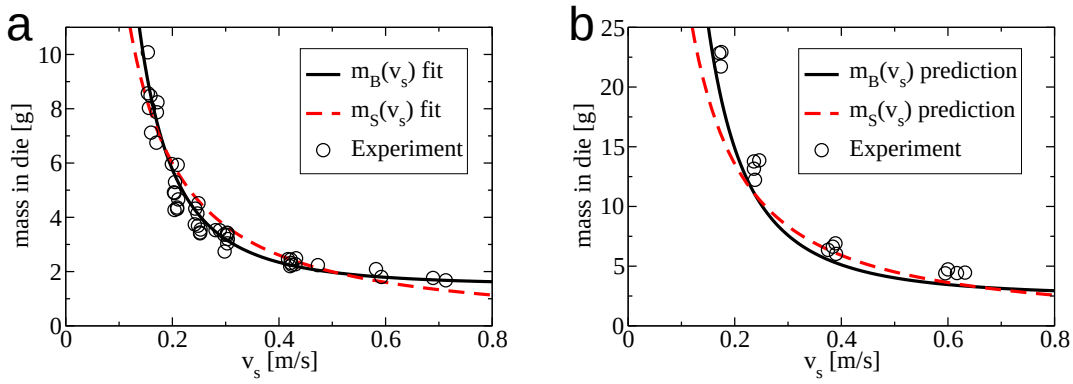

Figure 5.11: Comparison of $m_\mathrm{B}(v_\mathrm{s})$ and $m_\mathrm{S}(v_\mathrm{s})$ for a $D = 6\,\mathrm{mm}$ (a) and $10\,\mathrm{mm}$ (b) slit.

C_B	C_I	C_F	β	C_S	n
0.081	0.024	4.3	0.093	0.25	0.20

Table 5.3: Fitted dimensionless parameters of $m_\mathrm{B}(v_\mathrm{s})$ and $m_\mathrm{S}(v_\mathrm{s})$ for shoe discharge experiments.

of the experimental data is reproduced well; only the absolute values are slightly underpredicted. Using $m_\mathrm{S}(v_\mathrm{s})$ the agreement is good for intermediate shoe velocities while the discharge is strongly underestimated for low velocities. The general trend is covered less accurately. Note that only the expression $m_\mathrm{B}(v_\mathrm{s})$ for mass discharge has a sound physical motivation, while the formula for $m_\mathrm{S}(v_\mathrm{s})$ is purely empirical.

Deviations in the description of experimental data can be attributed to the fact that the cohesive strength σ_c of the powder should also be taken into account in Eq. (5.17). Therefore, an additional dependence on the dimensionless group $\sigma_\mathrm{c}/\rho_\mathrm{a} v_\mathrm{s}^2$ [104] is expected to improve the predictive power of Eq. (5.17).

5.3 Conclusion

DEM simulations of granular discharge from a hopper through a slit orifice were carried out. Stationary velocity profiles were analyzed in the vicinity of the orifice. The profiles collapse if lengths are normalized by the slit width D and velocities are normalized by $\sqrt{gD}$, where g is the gravitational acceleration. The data collapse is in agreement with the Beverloo equation for mass discharge through an orifice which states the same scaling properties [20, 109]. The velocity profiles are also independent of the grain diameter which was varied by a factor of two. This observation points out that granular flow close to the orifice differs substantially from the granular movement at further distances where grain size dependent velocity profiles were found experimentally.

The description of velocity profiles close to the orifice by means of kinematic modeling proved to be difficult due to pronounced spatial variations of the kinematic modeling parameter B. However, a correlation was found by locally relating B to the volume fraction. An analytic expression for this relationship was used in a modification of the kinematic modeling approach. The modification considers compressibility of the granular material and is therefore named compressible kinematic modeling. It was demonstrated that velocity profiles can be reproduced accurately via compressible kinematic modeling for given volume fraction distributions. Of course, the CKM approach would become more powerful, if it could predict a volume fraction distribution instead of requiring it. This issue is yet to be addressed in future investigations.

Granular discharge from a moving shoe was investigated with emphasis on the integral flow rate. A novel equation for the shoe-velocity-dependence of mass discharge through a slit orifice was derived and validated by simulations and experiments. This equation is based on a transient generalization of Beverloo's law for hopper discharge. The link between transient flow from a fixed hopper and stationary flow from a moving shoe was made by decomposing the shoe motion in discrete steps which appears to be a valid approximation.

6 Homogeneous filling of cavities

Cavity filling processes as introduced in Chapter 1 are investigated numerically in the following. Special emphasis is thereby put on the homogeneity of the density distribution.

Only few simulations of cavity filling can be found in the literature. Wu *et al.* [120, 76, 121] were the first to use DEM for cavity filling simulations in order to investigate the influence of escaping air and cavity geometry. Riera *et al.* [122] modeled cavity filling using a scheme based on the finite element method. Gustafsson *et al.* [123] developed a smoothed particle hydrodynamics model for the same purpose. Common to these approaches is that they use only two-dimensional descriptions and, therefore, provide at most a generic understanding of the filling process. So far, no studies incorporating a 3D description have been conducted.

Compared to numerous investigations on compaction and sintering only few experimental investigations on cavity filling have been carried out. Bocchini *et al.* [68] found that the integral filling densities decreases for small cavity sizes. Rice *et al.* [124] tested different devices for their ability to classify powder flowability and integral filling density. Hjortsberg *et al.* [125] observed density variations in a narrow ring cavity. Wu *et al.* [74] studied influences of cavity geometry and shoe kinematics on the integral filling density. In subsequent studies the same authors developed the concept of a critical shoe velocity for complete filling [29, 126, 75].

Results from filling experiments by Burch *et al.* [31] were used in this work to adjust a powder model and for comparison of density distributions. In the experiments Distaloy AE powder was used which is based on ASC100.29 powder but contains 4% nickel, 1.5% copper and 0.5% molybdenum. The results presented in Chapter 4 show that model D grains are capable of representing the irregularly shaped grains of ASC100.29 iron powder in both static and dynamic situations. Due to the morphologic similarity between ASC100.29 and Distaloy AE powder it is reasonable to use model D grains also to represent Distaloy AE in the simulation (compare Figs. 4.1 and 6.1). For the experiments in Ref. [31] a narrow ring cavity and a stepped ring cavity were used. Models of the cavities are displayed in Fig. 6.2. Simulations in the present work were also carried out with both cavities. Despite being rather generic in their geometry, the cavities contain typical features of industrial parts: namely, narrow sections and rotational symmetry.

Figure 6.1: Model D grain and industrially used Distaloy AE powder grain.

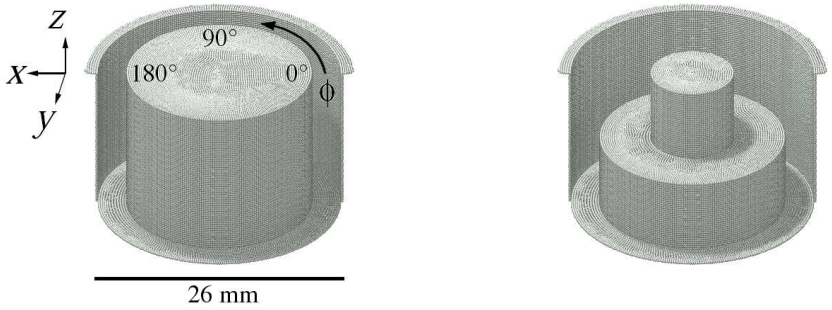

Figure 6.2: Models of narrow ring cavity and stepped ring cavity used for filling experiments and simulations. The feeding shoe moves from right to left during its first (third, fifth) passage and from left to right during its second (fourth, sixth) passage, i.e. it reaches the 0° position first on its first passage.

6.1 Coarse graining

For computational reasons it is not possible to carry out filling simulations of cavities with typical length scales in the range of centimeters, while using grains with mean diameters around 100 μm, which are typical for Distaloy AE. Thus, numerical coarse graining was applied in order to reduce the number of grains involved in the simulations. The investigations presented in Chapter 3 show that properties like volume fraction, angle of repose and flow rates are independent of grain size given that the parameters γ_n, κ_t, and w are scaled in proportion to R, while all other parameters are kept constant. However, boundary effects are not negligible if the grain size becomes comparable to the length scale of cavity features. In this section the influence of coarse graining on the filling simulation results is analyzed. Scaling of the force laws was applied as described in Chapter 3, i.e. $w \propto R$, $\gamma_\mathrm{n} \propto R$, $\kappa_\mathrm{t} \propto R$. The simulation parameters are summarized in Table C.6.

As a first test, the narrow ring (see Fig. 6.2a) was filled using a shoe velocity of 0.2 m/s. The ring width is 3.15 mm. The obtained filling levels for grain di-

ameters $d = 470\,\mu$m, $d = 940\,\mu$m, and $d = 1.88\,$mm are shown in Fig. 6.3a. The levels decrease with increasing grain size. This effect reflects the empty annulus concept [20], stating that the effective ring width is smaller for bigger grains (compare Section 3.2.2). The simulations were repeated using adjusted ring widths b_r according to the formula $b_r = b_0 + 1.4d$ with $b_0 = 1.83\,$mm, while the inner ring wall diameter is kept constant. The numerical value of $1.4d$ specifies the empty annulus zone [20, 14]. The adjustment yields very similar filling levels for the different grain sizes (see Fig. 6.3b). Thus, it appears necessary to adjust the dimensions of a cavity when using coarse graining to equal out the empty annulus effect. However, for a small ratio of grain size to cavity dimensions the relative change of the cavity dimensions will also be small.

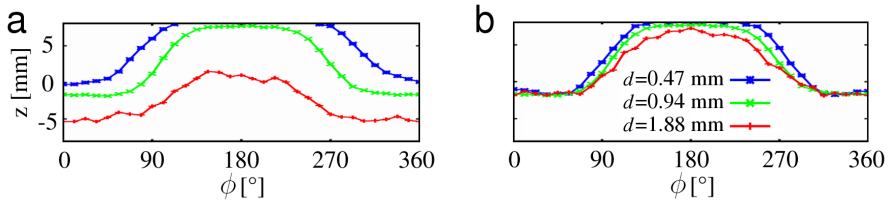

Figure 6.3: Filling levels in the narrow ring after one shoe passage with $v_s = 0.2\,$m/s. Simulations with non-adjusted (a) or adjusted (b) ring cavity width with respect to grain size.

As a second test, volume fraction distributions of completely filled cavities for different feeding shoe velocities and numbers of shoe passages were evaluated. The volume fractions were calculated using Voronoï tessellation as described in Section 2.2. The according density is obtained by multiplying the volume fraction with the material density of the grains. From a physical point of view it appears more general to express the results as volume fractions, which is done throughout this chapter. However, volume fraction and density are used synonymously, because the term *density distribution* is widely established in the powder technology community.

The density distributions are presented in Fig. 6.4. For the narrow ring cavity (Fig. 6.2a) the density is plotted against the azimuthal angle and height. For the stepped ring cavity (Fig. 6.2b) the density was evaluated in the yz-plane along the diameter of the cavity. The narrow ring cavity was adjusted to the grain size as discussed above, while the stepped ring cavity was not.

All of the distributions in the narrow ring cavity are similar for $d = 470\,\mu$m and $d = 940\,\mu$m. The main features appear for both grain sizes. Yet, for $v_s = 0.2\,$m/s after six shoe passages the densified surface layer reaches deeper into the cavity. The densification depth is apparently related to the actual grain size in agreement with a model of Hjortsberg *et al.* [125] (compare Section 6.4.2).

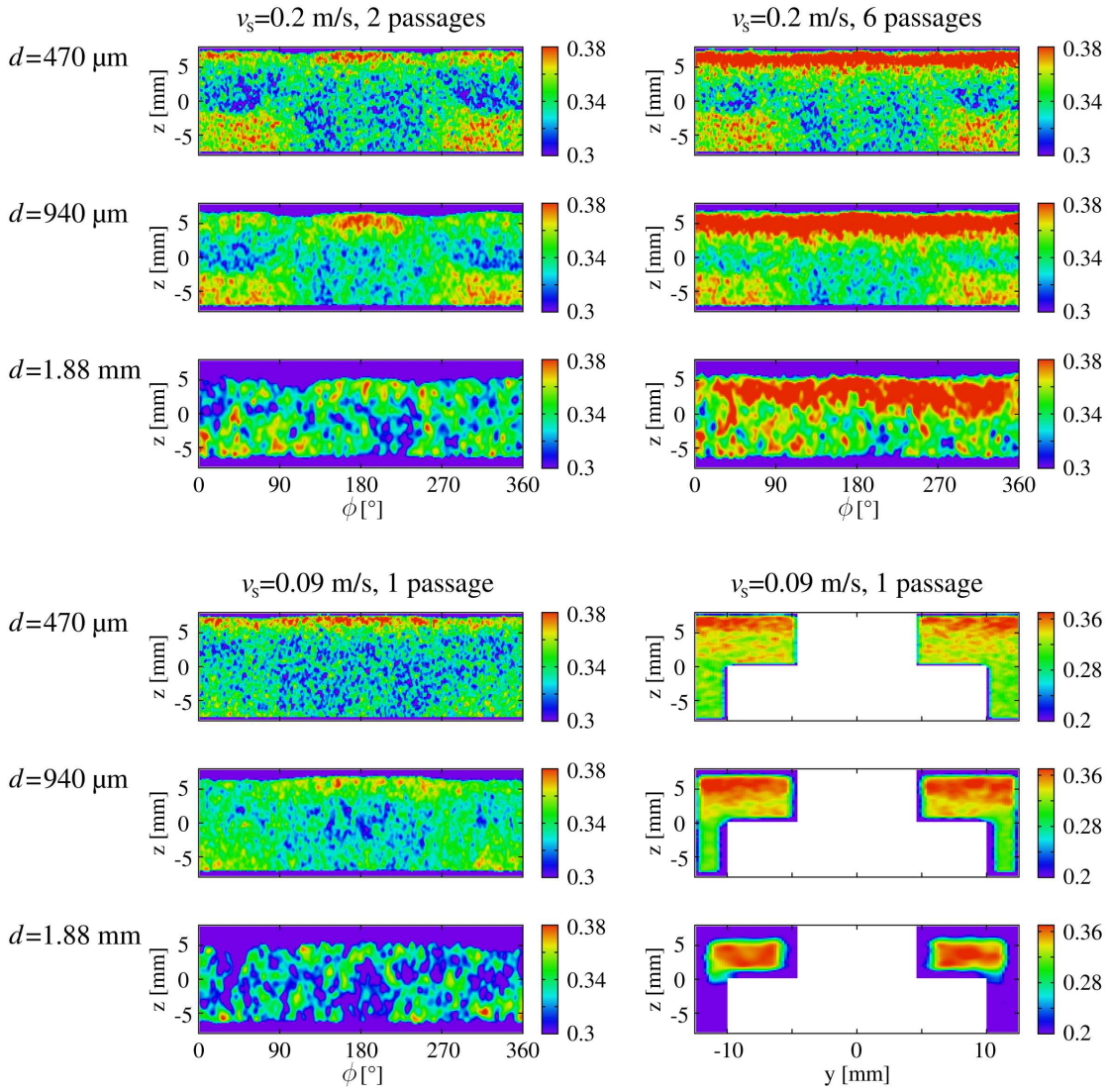

Figure 6.4: Influence of coarse graining on simulated density distributions. For each setup grain diameters $d = 470\,\mu$m, $d = 940\,\mu$m, and $d = 1.88\,$mm were tested.

A circumferential zone of low density appears for the stepped ring using $d = 940\,\mu$m grains in comparison to $d = 470\,\mu$m. This zone is the boundary layer of grains where the density is reduced due to the confining cavity walls (compare Fig. 3.3d and Ref. [68]). It can also be observed at the bottom of the ring cavities.

The simulations with $d = 1.88\,$mm differ strongly from those using smaller grains. For the narrow ring, azimuthal density variations are hardly observable and no surface densification is found except for $v_\mathrm{s} = 0.2\,$m/s after six shoe passages, where it reaches halfway through the cavity. The boundary layers at the bottom are roughly twice as large compared to $d = 940\,\mu$m. For the stepped ring, the boundary layers with reduced density are of the same size as the ring width in the lower, narrow part.

In summary, coarse graining can be applied up to a ratio of $d/b \approx 1/3$, where b is the smallest cavity dimension. Thereby, features in the density distributions are preserved. However, narrow parts of a cavity have to be adjusted according to the grain size to even the empty annulus effect out. Simulations with smaller grains than $d = 470\,\mu$m could not be carried out for computational reasons. A typical filling simulation with this grain size requires about 4500 CPU hours using Xeon 2 GHz processors.

6.2 Adjustment of model parameters

It is shown in Chapter 4 that the model parameters controlling friction, μ, and cohesion, w, have strong influence on the discharge rate from a feeding shoe and the angle of repose of the powder. Furthermore, if a numerical powder matches a real one in discharge rate, angle of repose, and to some degree also in morphology, it reproduces the azimuthal dependence of filling height in a narrow ring cavity well (compare Section 4.1.7). Measurements of an incompletely filled ring cavity using Distaloy AE powder are given in Ref. [31]. The model parameters μ and w were adjusted in an iterative process such that the filling level of the narrow ring cavity (Fig. 6.2) after one passage at a shoe velocity of $v_\mathrm{s} = 0.2\,$m/s is reproduced. The surface energy for wall-grain interaction, w_w, was set to zero. The wall friction coefficient was set to a typical value of $\mu_\mathrm{w} = 0.15$ [86]. Table C.6 gives an overview of all simulation parameters.

The shoe reaches the $0°/360°$ position first and the $180°$ position last on its passage. Figure 6.5 displays both experimental and simulation results of the filling level plotted as a function of the azimuthal angle. Good agreement between experiment and simulation could be achieved by using $\mu = 1.0$ and $w/R = 64\,\mathrm{J/m^3}$. Especially the slopes around $90°$ and $270°$, respectively, are well reproduced.

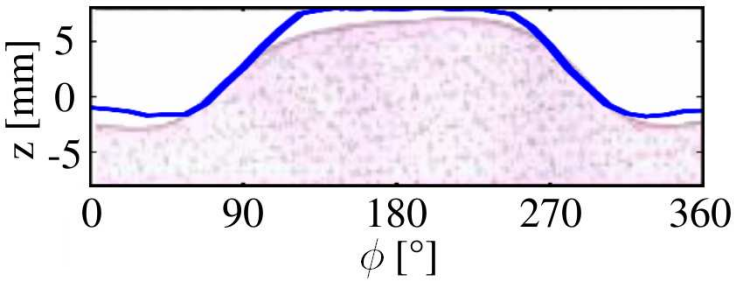

Figure 6.5: Filling levels in the narrow ring after one shoe passage with $v_s = 0.2\,\mathrm{m/s}$. Experiment with Distaloy AE (purple area) and simulation (thick line).

6.3 Prediction of density distributions

Spatial density distributions in completely filled cavities after one or several shoe passages were used as benchmarks for the filling simulations. Density distributions were experimentally measured using X-ray CT technique [31].

Figure 6.6 shows a comparison of measured and calculated density distributions. Only for the stepped ring cavity quantitative densities are published in Ref. [31]. Thus, the comparison between experiments and simulations for the narrow ring cavity is of qualitative nature. All simulations presented in the current section and in Section 6.4.1 were carried out using grains with diameter $d = 470\,\mu\mathrm{m}$.

After a single shoe passage at $v_s = 0.09\,\mathrm{m/s}$ significant features in the experimental distribution are a comparably low density around 180° throughout the whole height (see Fig. 6.6a). For angles smaller than 90° and larger than 270° the density in the lower half of the ring is markedly higher while surface densification is slightly reduced. All features found in the experiment were reproduced by the simulation. Note that surface densification is slightly exaggerated due to coarse graining, as the model grains are approximately five times larger than the experimental grains.

After two passages at $v_s = 0.2\,\mathrm{m/s}$ (see Fig. 6.6b) the experimental density in the 180° region is higher compared to the case of $v_s = 0.09\,\mathrm{m/s}$ and one passage. The highest density is found in small areas at the bottom of the cavity close to 90° and 270°. Around 0°/360° the density is lower except for a thin horizontal line at half height, corresponding to the filling level after a single passage. Gaps within the dense surface layer are located around 90° and 270°. The simulation is in agreement with the experiment except for some missing details around 0°/360°.

After six shoe passages (see Fig. 6.6c) further densification at the surface and in the region below 90° and above 270° occurs in the experiment. The region around 180° is only slightly densified. The simulation reproduces the experimental features. However, the depth of surface densification is overpredicted.

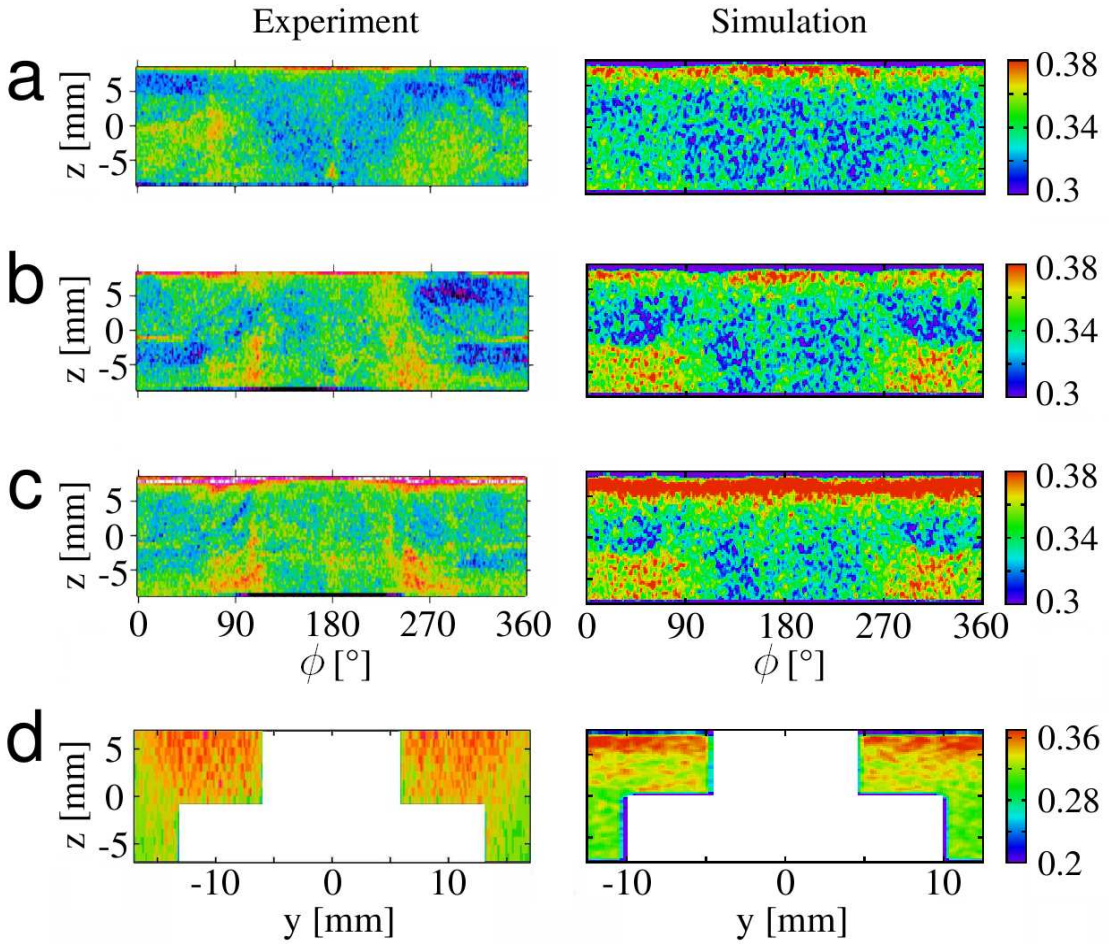

Figure 6.6: Comparison of density distributions from experiments [31] and simulations. Narrow ring filled with shoe velocity $v_s = 0.09\,\mathrm{m/s}$, 1 shoe passage (a). Narrow ring with $v_s = 0.2\,\mathrm{m/s}$, 2 passages (b) and 6 passages (c). Stepped ring with $v_s = 0.09\,\mathrm{m/s}$, 1 passage (d). Compare Fig. 6.2 for the shoe movement. Quantitative color scales refer only to simulations.

The experimental density in the upper part of the stepped ring is significantly higher (109% of mean density [31]) compared to the lower part (92% of mean density) where the cavity is narrower (see Fig. 6.6d). The simulation resembles the experimental observations. The simulated density near the surface of the stepped ring is about 0.36, while it is about 0.30 in the lower narrow part. Thus, the relative differences compared to the mean density of 0.33 are in very good agreement with the experimental results.

6.4 Transient filling analyses

6.4.1 Density formation during filling

The case of filling the narrow ring cavity at $v_s = 0.09\,\mathrm{m/s}$ was chosen as an example to illustrate the evolution of the density distribution during the filling process. Figure 6.7 depicts density maps, $\rho(\phi, z, t_0 + n\Delta t)$, for intervals of $\Delta t = 150\,\mathrm{ms}$ and $t_0 = 100\,\mathrm{ms}$. In addition, density difference maps, $\rho(\phi, z, t_0 + n\Delta t) - \rho(\phi, z, t_0 + n\Delta t - 50\,\mathrm{ms})$, are displayed. The plots reveal that density changes due to the newly arriving grains only occur close to the current surface. No significant densification can be observed in the bulk regions below the surface. Thus, the momentum of a discharged grain is absorbed within the surface layers. Features of the final density distribution can be explained by considering the cavity geometry and the feeding shoe movement: At $n = 0$ an initial heap of grains forms around $0°/360°$. The remaining space in the cavity is then filled until $n = 2$. The density in the lower part of the cavity (i.e. $z < 0\,\mathrm{mm}$) has its highest values around $0°/360°$. In that region the new grains impact perpendicularly onto the current surface region, thereby compacting it. In contrast, thoughout the remaining regions the newly arriving grains hit the surface at a lower angle and can also flow along the surface. Thus the compaction is less efficient. In the upper part of the cavity ($z > 5\,\mathrm{mm}$) the transient development of surface densification can be observed. At $n = 2$ the surface is only densified around $0°/360°$, while at $n = 3$ it is densified around the whole cavity. Yet, the densification is strongest around $180°$ where the powder is confined by the outer cavity wall in the direction of shoe movement.

6.4.2 Grain displacement and surface densification

Grain displacement fields are shown in Figs. 6.8 and 6.9 as they occur between subsequent shoe passages at $v_s = 0.2\,\mathrm{m/s}$ for the narrow ring and for a wide ring. All simulations presented from now on were carried out using grains with diameter $d = 940\,\mu\mathrm{m}$. The cavities are completely filled after the second shoe passage. Thus, the displacement fields are displayed from the third passage on. The strongest displacement is found within the topmost grain layers, which are in direct contact

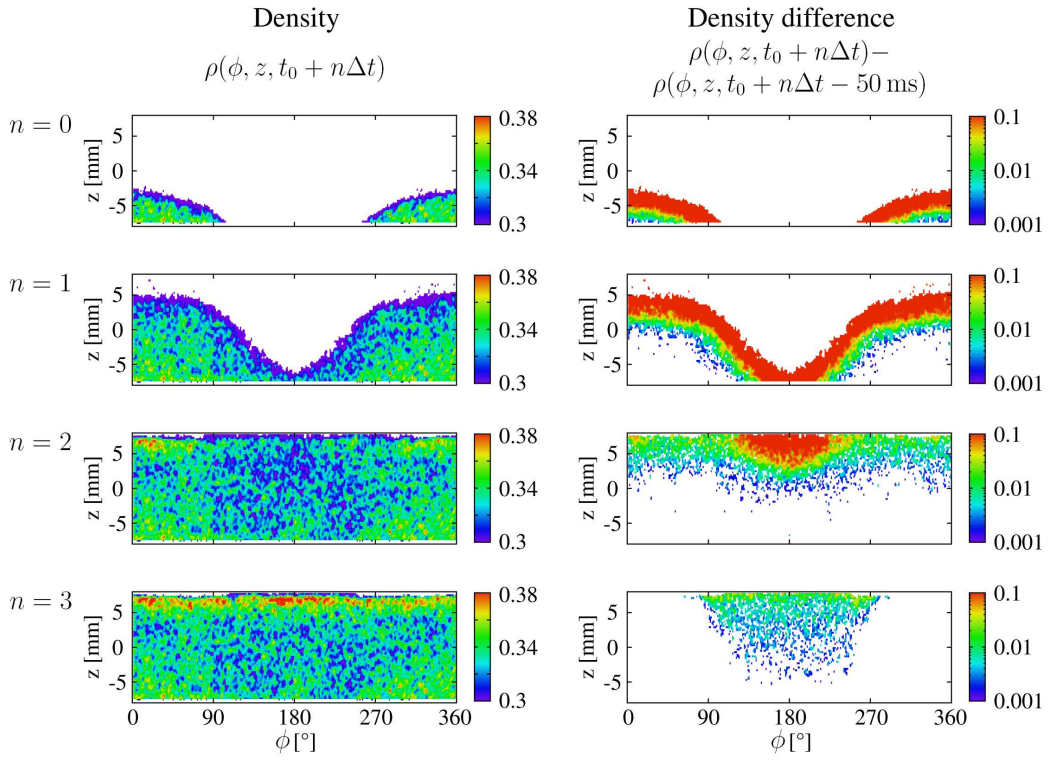

Figure 6.7: Density evolution during filling of the narrow ring at $v_\mathrm{s} = 0.09\,\mathrm{m/s}$.

with the powder inside the passing shoe. The rearrangement is affected by the cavity geometry. Compaction at the surface is especially strong near the 90° and 270° regions for the narrow ring, while it is rather homogeneous around the wide ring. In the narrow ring notable displacements occur down to approximately one third of the cavity height. For the wide ring the depth of displacement increases along the direction of shoe motion. These observations confirm a mechanism as proposed by Hjortsberg *et al.* [125], who ascribed compaction during subsequent shoe passages to shear induced granular rearrangement. Independent of cavity geometry it is observed that the strength of compaction decreases with the number of passages.

Densification of the granular bulk within filled cavities during subsequent shoe passages was investigated more closely by using density difference fields as plotted in Fig. 6.10. The fields were obtained by subtracting the density distribution after two (four) shoe passages from the distribution after four (six) passages. It is observed that the strength of compaction decreases with the number of passages. In all cases a gradient of densification exists, pointing from the bottom to the top of the cavities. For the wide ring densification reaches deeper than for the narrow

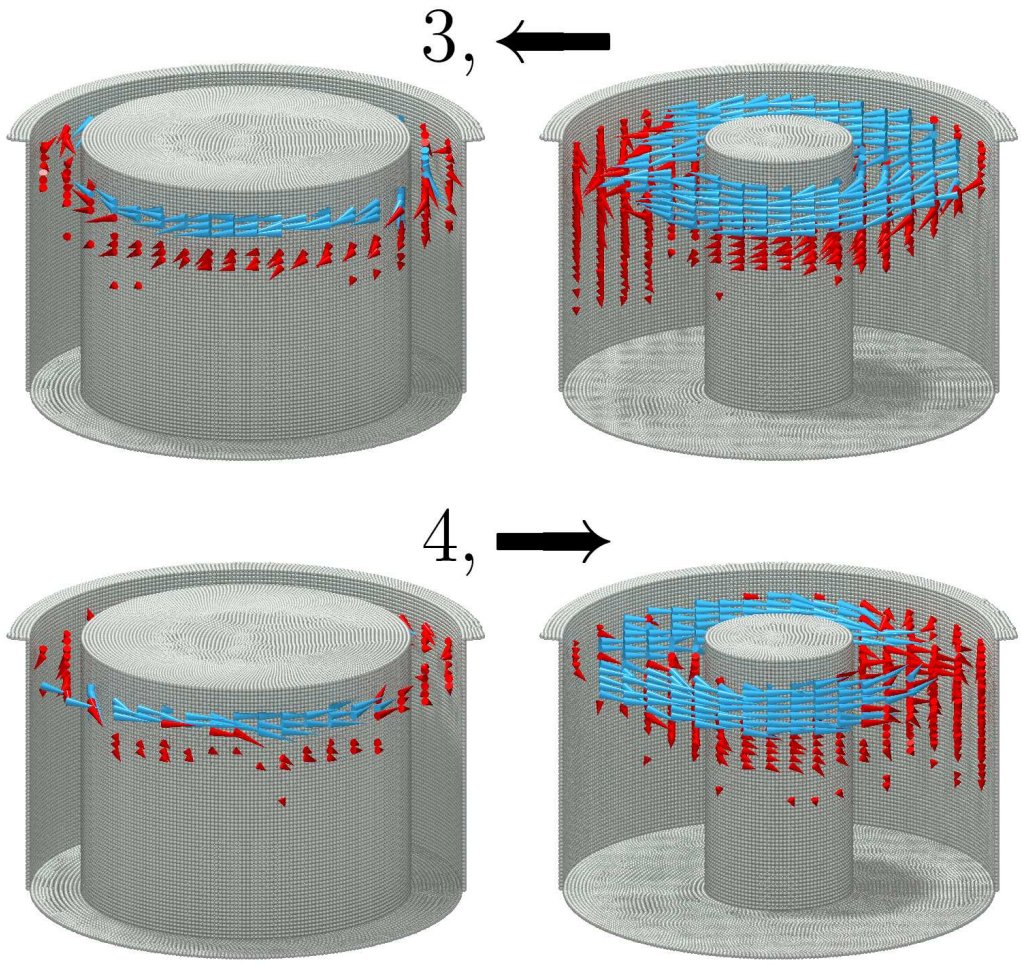

Figure 6.8: Grain displacements between subsequent shoe passages, labeled by passage number and direction. Each arrow head points towards the direction of the average grain displacement at its position. The length of the red arrows is proportional to the displacement magnitude. Blue arrows represent displacements above a threshold of 0.5 mm and have constant length. For better visibility all arrows are scaled up by a factor of five. Displacements below 0.1 mm and displacements of grains newly entering the cavities are not drawn.

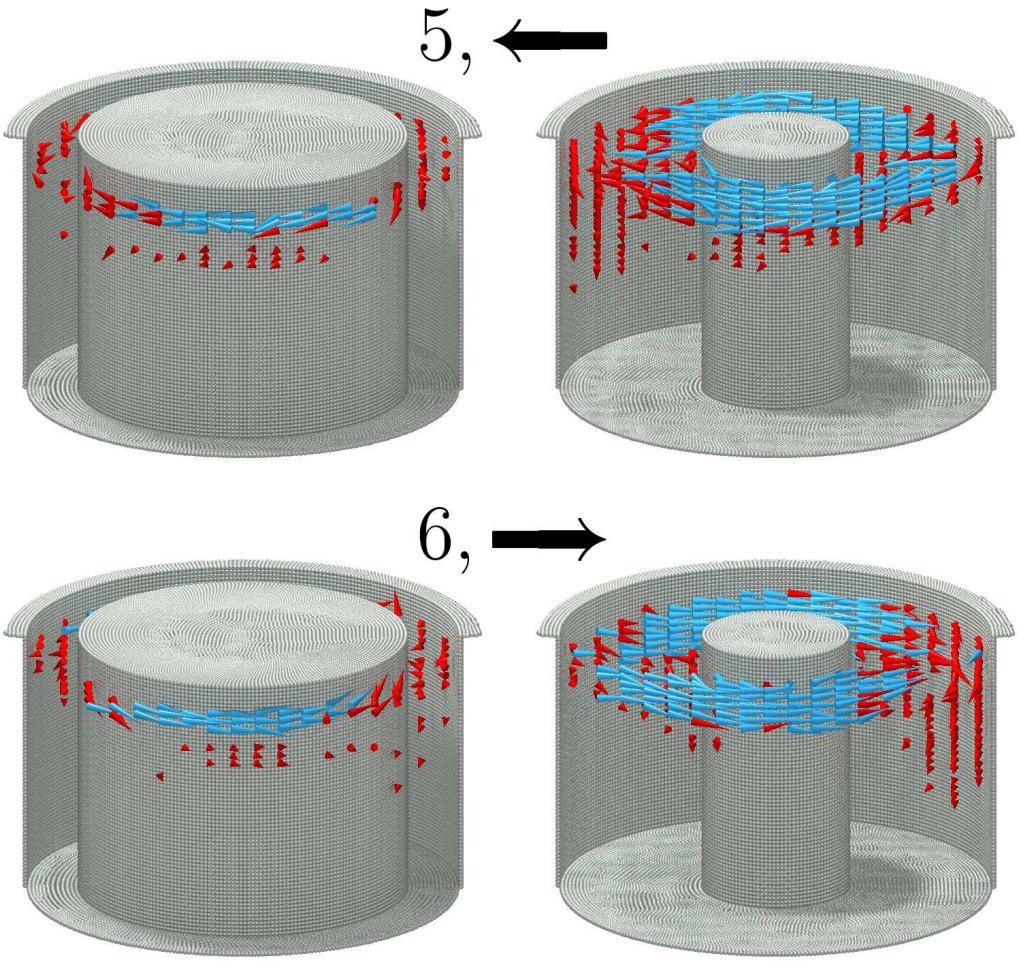

Figure 6.9: Same as Fig. 6.8 but for fifth and sixth shoe passage.

ring. Yet, densification at the surface is stronger in the narrow ring. Between two and four passages, compaction close to the cavity surface is homogeneous around the wide ring while it is especially strong around 90° and 270° for the narrow ring. Figure 6.6b shows that after two passages the surface region at 180° is denser compared to 90° and 270° in the narrow ring. The surface densification is seemingly more effective in those formerly less dense regions. In the lower half of both cavities the densification is more pronounced at 0°/180° than at 90°/270°. The displacement fields (Figs. 6.8 and 6.9) give the explanation: At 0° and 180° grains move rather vertical than lateral due to the confining cavity walls. Thereby the bulk material beneath is compacted.

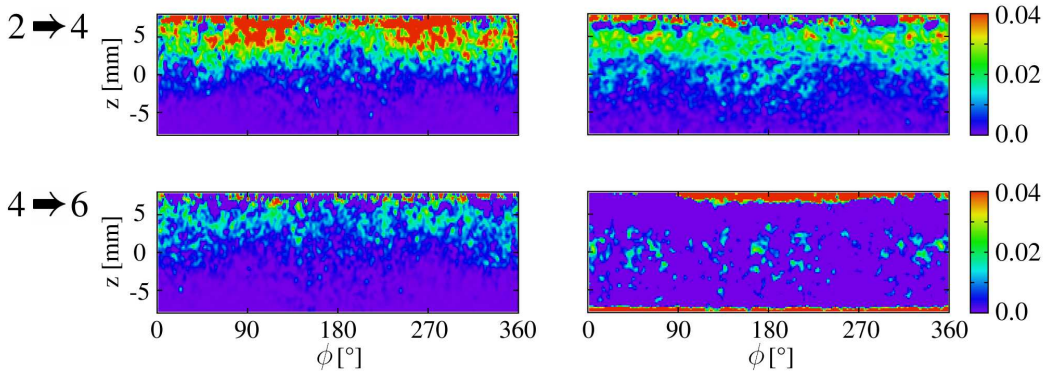

Figure 6.10: Density differences in narrow (left) and wide (right) ring cavity between second and fourth feeding shoe passage as well as between fourth and sixth passage.

In summary, the transient filling analyses reveal that density inhomogeneities are mainly caused by the feeding shoe movement which does not respect the typically rotational cavity symmetry. Thus, this method of cavity filling is intrinsically anisotropic.

6.5 Density (in)homogenization

In this section variations of the filling process are investigated for their effects on the final density distribution.

6.5.1 Influence of shoe velocity

For both the narrow ring and the stepped ring cavity the shoe velocity was varied in further simulations. The resulting densities after one shoe passage using three different velocities are displayed in Fig. 6.11. In the case of the narrow ring the

density distributions are more inhomogeneous for low shoe velocities. The strongest surface densification and the most pronounced density dependency on the azimuthal angle is observed for the lowest velocity. In the stepped ring the distributions are very similar for all three velocities. Thus, lowering the shoe velocity does not generally help to improve homogeneity.

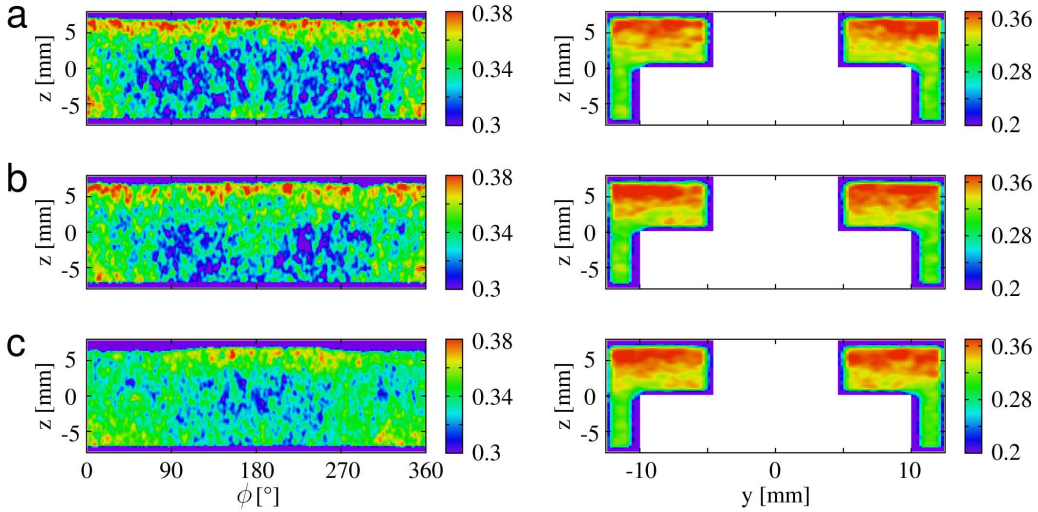

Figure 6.11: Density distributions using varied shoe velocities for the narrow ring and the stepped ring. (a): $v_s = 0.022\,\mathrm{m/s}$, (b): $v_s = 0.044\,\mathrm{m/s}$, (c): $v_s = 0.09\,\mathrm{m/s}$.

6.5.2 Cavity and shoe vibrations

The effects of oscillations of the shoe or the cavity during or after the filling stage were investigated for the narrow ring cavity. The shoe velocity was 0.09 m/s in all cases.

First, oscillations with a frequency $f = 32\,\mathrm{Hz}$ and an amplitude 1 mm in the direction of shoe motion (x-axis) were applied during the filling stage. The oscillation frequency f is the inverse of the oscillatory period. Figure 6.12 shows the density distribution after one passage of the feeding shoe. Shaking the shoe does not alter the density significantly compared to the case without any oscillations (see Fig 6.11c). However, cavity oscillations have a strong impact on the distribution. The average density increases and angular density variations appear. The cavity sections oriented parallel to the axis of oscillation (i.e. 90°/270° for shaking along the x-axis) are denser than those perpendicular to it.

Second, cavity oscillations with 1 mm amplitude perpendicular to the shoe motion (i.e. along the y-axis) were applied after the shoe passage. The frequency was varied

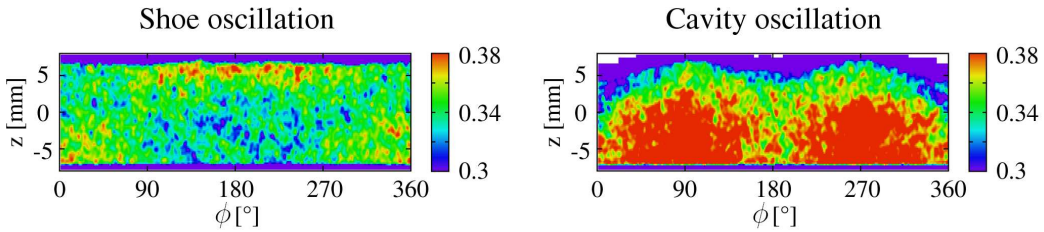

Figure 6.12: Densities for the narrow ring cavity under oscillations along the x-axis during the filling stage.

between 2 Hz and 32 Hz. Figure 6.13 shows the results. Up to 8 Hz the density distribution remains unaffected compared to the case without any oscillations. At 20 Hz strong densification near the 0°/360° and 180° positions occur reaching from the surface downwards into the cavity. At 32 Hz the situation is reversed and densification is pronounced in the lower half of the cavity. Note, that the density distribution for $f = 32$ Hz is very similar to the case of cavity oscillation during filling (Fig. 6.12) except for the different shaking direction. Thus, it appears to be unimportant whether the oscillations are applied during or after the filling stage.

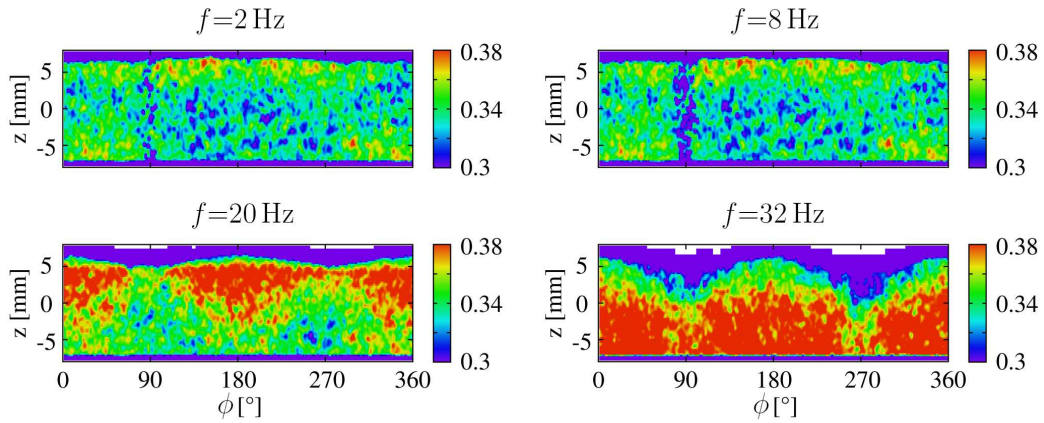

Figure 6.13: Densities for the narrow ring cavity under varied oscillation frequencies along the y-axis after the filling stage.

In order to overcome the anisotropy caused by linear oscillations, the influence of rotational oscillations was investigated. The motion of each point of the cavity

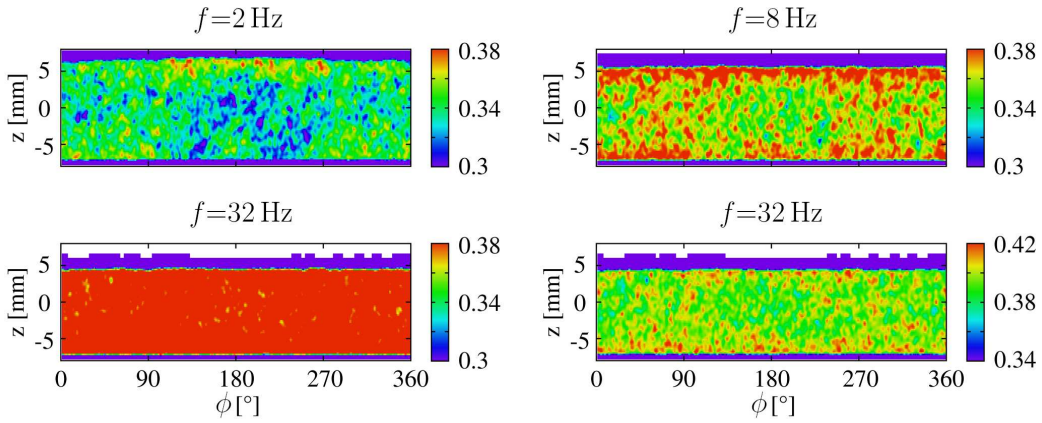

Figure 6.14: Densities for the narrow ring cavity under different rotational oscillation frequencies using an amplitude of 5° after the passage of the shoe. A second density map with different color scale is given for the case of $f = 32\,\mathrm{Hz}$ for clarity.

is described by

$$\mathbf{r}(t) = \begin{pmatrix} \cos(\theta(t)) & -\sin(\theta(t)) & 0 \\ \sin(\theta(t)) & \cos(\theta(t)) & 0 \\ 0 & 0 & 1 \end{pmatrix} \mathbf{r}(0), \quad \theta(t) = \theta_0 \sin(2\pi f t), \tag{6.1}$$

where the origin of the coordinate system lies in the center of the cavity. Thus, the axis of rotation is the z-axis. The rotational oscillation amplitude is $\theta_0 = 5°$, which corresponds to a displacement of 1 mm at the circumference of the ring. The frequency f was varied between 2 and 32 Hz. Figure 6.14 shows density distributions using rotational oscillations applied after filling with $v_\mathrm{s} = 0.09\,\mathrm{m/s}$. For $f = 2\,\mathrm{Hz}$ the effect is negligible. However, using $f = 8\,\mathrm{Hz}$ or 32 Hz the angular dependency of the density distribution vanishes. Especially for $f = 32\,\mathrm{Hz}$ the density is rather homogeneous throughout the cavity. The overall density increases with f and the filling height decreases as a direct consequence.

6.5.3 Volumetric filling

The technical term *volumetric filling* means that the lower punch of the tool set sucks the powder into the cavity from the feeding shoe, which may stop or move during this operation (compare Fig. 6.15). Figure 6.16 displays density distributions using volumetric filling. Shoe oscillations along the x-axis with a frequency of 2 Hz and an amplitude of 1 mm are applied during the punch movement, because arching occurs in the narrow ring without oscillations and the powder does not fall into the

cavity. For the narrow ring volumetric filling yields a homogeneous distribution without azimuthal density gradients. The density is slightly higher at the bottom or top of the cavity compared to half height. For the stepped ring cavity the density in the lower narrow part is increased in comparison to the case of conventional filling (compare Fig. 6.11) and comparable to the density in the upper wide part. However, a region of lower density exists at the transition between the wide and narrow part.

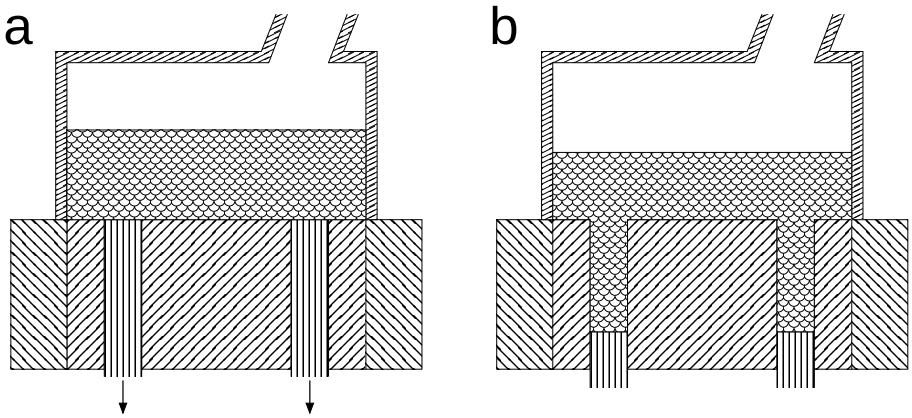

Figure 6.15: Schematic of the volumetric filling process. (a): The shoe moves into position. (b): The powder is sucked into the cavity due to punch movement.

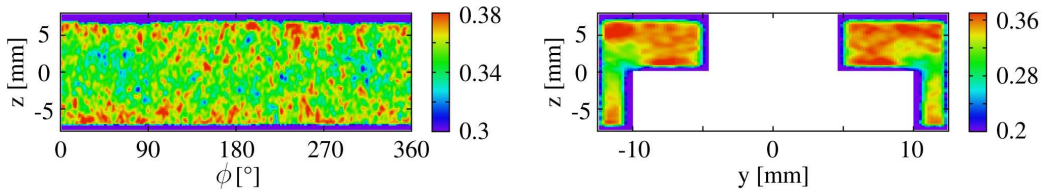

Figure 6.16: Densities for the narrow and stepped ring cavity using volumetric filling with punch velocity 0.02 m/s. The filling is supported by shoe oscillations.

6.6 Conclusion

It was demonstrated that observed features of the density distribution after filling can be reproduced and, thus, predicted by DEM simulations. A simple way of model parameter adjustment was used to match the filling behavior observed in the experiment using the irregular shaped Distaloy AE powder. Simulations with up to ten times larger grain diameters than in reality are able to predict significant density features. The simulations only fail if grain diameters are comparable to cavity dimensions.

The density distribution appears to be strongly determined by the cavity geometry. In the case of incomplete filling the feeding shoe velocity does also affect the density. The shoe velocity has only little influence if the cavity is filled completely.

After grains have settled in the cavity they stay at their positions and the local density remains constant. The kinetic energy of newly arriving grains does only contribute to a slight densification of the current surface.

Regarding subsequent shoe passages, two propositions of the compaction model of Hjortsberg *et al.* [125] could be verified by the present simulations: The densification is limited to a certain depth and it is less pronounced at the location where the shoe meets the cavity first. In addition, it was shown that the compaction depth is correlated with grain size. Therefore, it is necessary to simulate the process with realistic grain sizes if the effect of surface densification is not to be overestimated.

Cavity oscillations affect the density strongly and can be used to homogenize the distribution. However, oscillations might as well introduce inhomogeneities, if they do not respect the cavity symmetry. Thus, rotational oscillations turn out to be helpful for a ring cavity. It is evident that the application of cavity oscillations might not be easily implemented in a given die compaction system. However, by using simulations the possible improvements of these technique can be estimated.

Volumetric filling by punch movement proved to be helpful for homogenization, because intrinsic anisotropies caused by the direction of shoe movement are avoided. However, the build-up of arches must be avoided in slender cavities e.g. by some shaking.

7 Summary and outlook

A numerical study of granular matter at the transition of solid-like and liquid-like behavior was carried out in the framework of the discrete element method.

A coarse graining method was derived for scaling the grain size in DEM simulations of a granular system without changing macroscopic properties of the system. It is based on the conservation of the local energy density in the system. The gravitational potential energy density is preserved for unvaried mass density of the scaled grains. The kinetic energy density decreases due to inelastic grain collisions. A dimensional analysis of binary collisions yielded scaling rules for the material parameters in the DEM force laws. These rules ensure the independence of kinetic energy density loss in collisions on the grain size. The application of the scaling rules leaves the coordination number distribution, the volume fraction, and the potential energy stored in grain contacts unchanged for variation of the grain size in a granular bulk. Discharge through a slit and angle of repose formation were used as further tests for the proposed coarse graining method. These setups exhibit grain size related surface or boundary effects which, however, vanish in the limit of small grain diameters. Apart from these effects, macroscopic properties of the granular medium are invariant under the proposed coarse graining method. Notably, the scaling rules remain valid in bulk systems with multi-grain contacts although derived from binary contacts.

The proposed scaling method allows for the investigation of systems with large particle numbers which were previously unapproachable. The coarse graining scheme differs from a scaling of all external length scales as the latter procedure might alter dimensionless numbers which characterize the system and thereby change the physical process being studied. Nevertheless, it has to be checked whether or not system properties depend intrinsically on the actual grain size. If so, the coarse graining method cannot be applied. It will be interesting to figure out to what extend the scaling scheme can be applied to other granular systems, e.g. whether or not it preserves properties of sound propagation in a granular bulk [127] or the density of a granular gas [28].

Flexible and reliable DEM models can be utilized in the virtual laboratory in order to discover new physical laws of granular systems. This approach can be superior to experiments due to the inherent availability of complete phase space and grain contact information. In addition, industrial processes including powders can be optimized numerically with an appropriate model. For the scope of this work a grain model should be able to reflect both flow and filling properties of a

real powder. No studies on modeling a real powder in such a comprehensive manner, i.e. covering static and dynamic regimes as well as the transitions between them, have been published so far. Therefore, DEM models of different mechanical and morphological complexity were compared to a real iron powder. Model parameters were fitted by matching macroscopic quantities, i.e. the angle of repose of a powder heap and the powder mass flow from a moving shoe through a defined orifice. It was found that grain shape is an essential parameter besides friction and cohesion between the grains. The iron powder consists of irregular, asperitic grains. It could be represented best by a model with likewise shaped grains. This model also proved to be capable of predicting the behavior of the iron powder in a different setup: the filling of a circular cavity with a feeding shoe.

The findings suggest a fitting procedure for the adjustment of static and dynamic properties of a DEM grain model. Friction, cohesion, and a shape parameter should be adjusted in order to match the angle of repose, discharge rate, and volume fraction of a real powder. Note however that such a procedure is computationally demanding, i.e. it would require about 10^5 CPU hours. Future model improvements should address the following issues: An inclusion of particle size distributions would allow for the study of segregation phenomena [128, 129]. Collisions between complex shaped grains will be described in greater detail, if a closer approximation of the real grain shape is used [85]. Especially for small and light grains the explicit consideration of air drag is necessary [121]. This requires an efficient method to couple DEM computations with an air flow solver in three dimensions.

An accurate continuum model for the description of granular velocity fields inside discharging hoppers was derived. It is based on the kinematic modeling approach which relates the horizontal velocity component to the gradient of the vertical velocity component via a coupling constant B which has the unit of length. The basic kinematic modeling assumption of incompressibility was replaced by explicitly considering the volume fraction field in the hopper. Consequently, the extended approach is referred to as compressible kinematic modeling. It was demonstrated that B is a monotonically increasing function of the local volume fraction up to 95 % of the maximum volume fraction of the system. The only relevant length-scale in the vicinity of the hopper orifice is the width of the orifice. Thus, B scales with the size of the orifice. So far, compressible kinematic modeling cannot predict the volume fraction field but requires it. A transient description of the system which includes the evolution of the volume fraction field would therefore be beneficial and should be addressed in the future.

Complementary to discharge from an immobile hopper, granular outflow from a moving shoe was investigated. Thereby, a novel equation for the shoe-velocity-dependence of mass discharge through a slit orifice was derived. This was achieved by mapping a transient extension of the Beverloo equation for hopper discharge onto the moving shoe regime.

The optimization of cavity filling as used in powder technological part production

provides a challenging application for DEM simulations due to the large number of particles involved. In order to study the filling process, use was made of a coarse grained, non-spherical DEM grain model as developed in the course of this work. Comparisons with X-ray computer tomography measurements [31] revealed that an adequately adjusted, coarse grained model can predict density distributions depending on cavity geometry and process parameters (e.g. feeding shoe velocity) qualitatively and partly even quantitatively. It was shown that density inhomogeneities are mainly influenced by the combination of cavity geometry and feeding shoe velocity. A schematic model for surface densification in subsequent shoe passages due to shear of the topmost granular layers in the cavity [125] was confirmed. Two possible procedures for density homogenization were identified: First, the suction of the powder into the cavity due to punch movement avoids density anisotropies caused by feeding shoe movement. Second, rotational oscillations applied after the filling stage yield homogeneous distributions in cavities with rotational symmetry.

Yet another application example with high industrial relevance is the wire sawing process for silicon wafer separation. Numerical investigations on the interaction of abrasive grains, wire, and ingot in a hydrodynamic environment are presented in Appendix A with the main outcome that the spatial stress distribution on the ingot surface strongly depends on the applied wire velocity and stress. This result adds to a more profound understanding and, thus, improvement of the process.

Some remarks shall be given on the used computational resources in this work. A slit outflow simulation as presented in Section 4.1.1 takes about 300 CPU hours. Roughly 600 CPU hours are required for an angle of repose simulation as shown in Section 4.1.3 and for a silo outflow simulation as presented in Section 5.1. A complete die filling simulation (Chapter 6) which involves 600,000 grains, i.e. four million basic spheres, takes about 4,500 CPU hours. All values are given for calculations running on Xeon 2 GHz CPUs using model D with a grain diameter of 470 μm. The computational time was reduced by using up to 35 CPUs in parallel.

In conclusion, several results of general relevance for the description and handling of granular systems were obtained within the scope of this work: a DEM coarse graining scheme (Chapter 3), a procedure providing realistic DEM models for rapid flow and filling situations (Chapter 4), improvements of the kinematic modeling picture for granular flow from a hopper as well as an analytic expression for the powder mass discharge from a moving shoe (Chapter 5), and optimization strategies for density homogenization in cavity filling (Chapter 6).

Future developments of discrete element modeling as well as increasing computational resources will allow for a rise in numerical optimization of technological processes and will contribute in no small part to building a comprehensive theoretical framework for granular matter.

A Modeling of wire sawing

Wire sawing is an efficient process for wafer slicing from a silicon ingot. It is massively employed both in the solar and the semiconductor industry. Multi-wire saws use an assembly of several hundred parallel running wires to simultaneously separate the wafers. The width of the sawing grooves which corresponds to non-recyclable Si dust is referred to as kerf loss. A wafer thickness of about 220 μm and a kerf loss of about 180 μm can be achieved by using a typical wire diameter of 140 μm. Yet, there is still an economic demand for a decrease in wafer thickness and kerf loss while meeting high standards for wafer quality, e.g. strength and roughness. A systematic optimization under these conditions requires a profound and detailed understanding of the wire sawing process.

The abrasive slurry used in the sawing process typically consists of polyethylene glycol (PEG) with suspended silicon carbide grains. The sawing wire drags the slurry through a groove in the Si ingot where the SiC grains cause the abrasion. However, microscopic details of the sawing process are not fully understood, partly because experimental in-situ investigations are not possible so far.

In this chapter numerical investigations of the dynamic interactions between wire, slurry, and ingot in the sawing groove are presented. The particle based simulations allow for analyses of the process at SiC grain level.

A.1 Numerical method

The system consisting of Si ingot, sawing wire, and PEG/SiC slurry was modeled using a hybrid approach, i.e. fluid and rigid body dynamics are coupled in the simulation. All components of the system were composed of spherical particles as basic building blocks. The particle movement is governed by Newton's equations of motion and a velocity Verlet scheme, Eq. (2.2b), is used for explicit time integration. The actual force laws yield physically reasonable behavior of the components, e.g. hydrodynamic flow of the PEG or repulsion between distinct SiC grains. Details of the modeling approach are given in the following sections.

A.1.1 Modeling of PEG

An extension of the dissipative particle dynamics (DPD) method [44] was used to describe the PEG fluid. Basic DPD particles can be interpreted as single molecules

or lumps of fluid molecules depending on the applied level of coarse graining. Their interaction is given by a density-dependent force as described in Ref. [130],

$$\begin{aligned}\mathbf{f}_{ij}^{\mathrm{C}} = \Bigg(2K\Big(&(\rho_i - \rho)\,\rho_i^2 + (\rho_i - \rho)^2\,\rho_i \\ &+ (\rho_j - \rho)\,\rho_j^2 + (\rho_j - \rho)^2\,\rho_j\Big) w\left(r_{ij}\right)\Bigg)\hat{\mathbf{r}}_{ij},\end{aligned} \tag{A.1}$$

a dissipative force,

$$\mathbf{f}_{ij}^{\mathrm{D}} = -\left(\gamma_{\mathrm{D}} w\left(r_{ij}\right)^2 \left(\mathbf{v}_i - \mathbf{v}_j\right)\cdot\hat{\mathbf{r}}_{ij}\right)\hat{\mathbf{r}}_{ij}, \tag{A.2}$$

and a stochastic force,

$$\mathbf{f}_{ij}^{\mathrm{R}} = \left(\sigma_{\mathrm{R}} w\left(r_{ij}\right)\boldsymbol{\zeta}_{ij}\right)\hat{\mathbf{r}}_{ij}, \tag{A.3}$$

where $r_{ij} = |\mathbf{r}_{ij}|$, K is a compressibility constant, $\rho$is the average fluid number density, ρ_i is the local number density at $\mathbf{r}_i$, γ_{D} is a dissipative constant, and σ_{R} is a random force constant. $w\left(r_{ij}\right)$is a monotonically decreasing weight function which vanishes for particle distances larger than the interaction range r_{c},

$$w\left(r_{ij}\right) = \begin{cases} 1 - \frac{r_{ij}}{r_{\mathrm{c}}} & , r_{ij} < r_{\mathrm{c}} \\ 0 & , r_{ij} \geq r_{\mathrm{c}} \end{cases}. \tag{A.4}$$

$\boldsymbol{\zeta}_{ij}$ is a Gaussian white noise with vanishing mean value and a variance of unity. Equation (A.1) models the fluid's thermodynamics and allows for the formation of free surfaces. Equation (A.2) describes viscous damping of the fluid and Eq. (A.3) is motivated by the influence of suppressed atomic degrees of freedom. A fluctuation-dissipation theorem is satisfied via $\sigma_{\mathrm{R}}^2 = 2\gamma_{\mathrm{D}}(k_{\mathrm{B}}T)'$, where $(k_{\mathrm{B}}T)'$ is the product of Boltzmann constant and temperature in reduced numerical units.

The DPD simulation scheme makes use of intrinsic units which cannot be converted into SI units in an unambiguous way. A possible way to perform the conversion is described as follows. A coarse graining level of unity is chosen, i.e. a DPD particle corresponds to a single PEG molecule with mass $m_{\mathrm{PEG}} = 200\,\mathrm{u}$ and volume $V_{\mathrm{PEG}} = 2.9 \cdot 10^{-28}\,\mathrm{m}^3$. This sets the unit of mass to $[m] = m_{\mathrm{PEG}} = 3.3 \cdot 10^{-25}\,\mathrm{kg}$. Density conservation yields the unit of length, $[r_{\mathrm{c}}] = \sqrt[3]{\rho V_{\mathrm{PEG}}} = 1.1\,\mathrm{nm}$. The thermal velocity of the PEG molecules, v_{th}, defines the unit of time, $[\tau] = r_{\mathrm{c}}/v_{\mathrm{th}} = r_{\mathrm{c}}/\sqrt{3k_{\mathrm{B}}T/m_{\mathrm{PEG}}} = 6.0\,\mathrm{ps}$ for $T = 300\,\mathrm{K}$. An overview of the simulation parameters is given in Table C.7.

A snapshot of a fluid drop is shown in Fig. A.1. The blue spheres are the individual DPD particles.

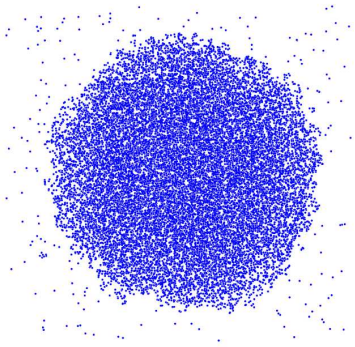

Figure A.1: DPD particles forming a fluid drop.

A.1.2 Modeling of SiC grains

Each SiC grain consists of an ensemble of rigidly connected particles. The method described in Section 2.1.4 was used to conserve the rigidity over time. The basic particles of the SiC grains interact with the DPD particles of the PEG via Eqs. (A.1)–(A.3). Thereby, hydrodynamic coupling between the PEG model and the grains is ensured. Linear and angular momentum of the fluid is transferred to the grains causing drag and rotation. Basic particles of two distinct SiC grains interact via elastic repulsion,

$$\mathbf{f}_{ij}^{\mathrm{E}} = \left(\kappa w \left(r_{ij}\right)^{3/2}\right) \hat{\mathbf{r}}_{ij}, \tag{A.5}$$

to satisfy the excluded volume of each grain; κ sets the repulsive strength. Although no explicit frictional force is used, torque is transmitted between grains due to their morphological ability to interlock. A microscopic image of typical SiC grains is displayed in Fig. A.2a. Fig. A.2b shows the corresponding model grains. The grain size distribution used for the simulations resembled the experimentally measured one.

A.1.3 Modeling of wire and ingot

Both the sawing wire and the Si ingot are represented by rigidly connected particles. The viscoelastic interaction between the particles of the wire or ingot and those of the SiC grains is defined by Eqs. (2.3) and (2.6). At the interfaces between the wire or ingot, respectively, and the PEG fluid no-slip boundary conditions are ensured by using an adhesive DPD wall model [131]. No fracture mechanism is included in the model. Yet, stresses acting on the SiC grains and the Si ingot can be extracted from the simulations. Figure A.3a shows a schematic drawing of wire and ingot. The setup is periodic along the y-axis thereby resembling an infinitely long wire and cutting groove.

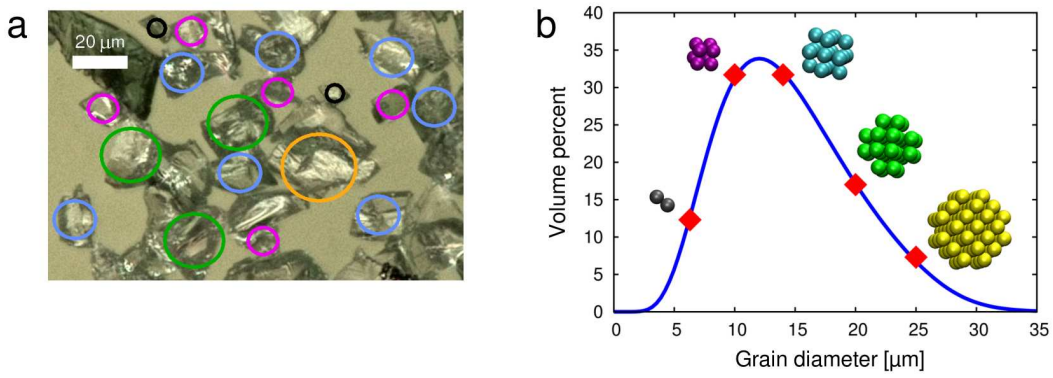

Figure A.2: (a): Microscopic image of SiC grains. (b): Corresponding model grains and size distribution as used in the simulations.

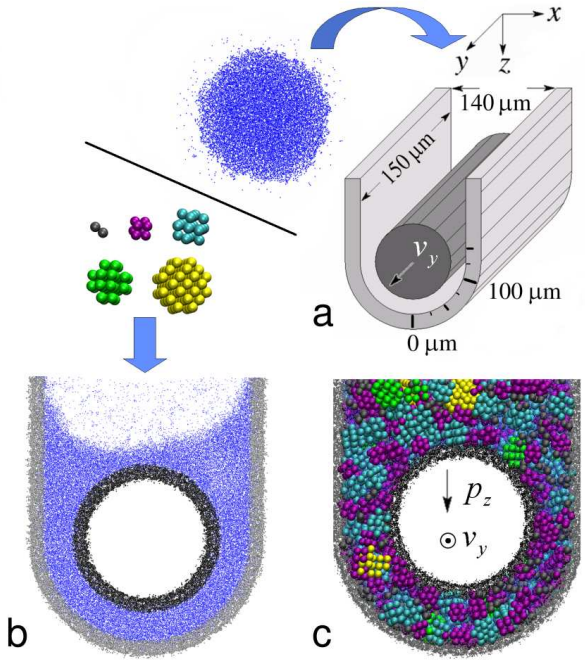

Figure A.3: (a): Schematic of ingot groove and wire. Snapshots from simulations including only PEG (b) and with complete slurry (c).

Quantity	Simulation value	Equivalent experimental value
Wire diameter	22 nm	100 μm
Wire velocity	122 m/s	17 m/s
Wire stress	89 N/mm^2	1.5 N/mm^2
Slurry density	1.7 g/cm^3	1.7 g/cm^3
Slurry viscosity	0.34 mPa s	200 mPa s

Table A.1: Overview of simulation parameters and equivalent experimental values in terms of dynamic similarity.

A.2 Model validation

A.2.1 Dynamic similarity

On the basis of the derived units the simulations are limited to comparably small time (about 100 ns) and length scales (about 100 nm). However, it is possible to compare numerical and experimental results by using two non-dimensional numbers which characterize the system. The Reynolds number,

$$\mathrm{Re} = \frac{v d \rho_\mathrm{S}}{\eta}, \tag{A.6}$$

is the ratio of inertial to viscous forces. For a typical wire sawing situation using a wire velocity $v = 17\,\mathrm{m/s}$, slurry density $\rho_\mathrm{S} = 1.7\,\mathrm{g/cm^3}$, slurry viscosity $\eta = 200\,\mathrm{mPa\,s}$ and an approximate distance $d = 20\,\mu\mathrm{m}$ between wire and ingot the resulting Reynolds number is $\mathrm{Re} = 3$. In the simulations d and ρ_S are set while η is measured using Lees-Edwards boundary conditions [45]. The requirement to meet the experimental Reynolds number then defines the wire velocity in the simulations. The ratio of an external stress p to the kinetic energy per volume,

$$\mathrm{C} = \frac{p}{\frac{1}{2}\rho_\mathrm{S} v^2}, \tag{A.7}$$

renders the conversion of the applied wire stress between simulation and experiment possible. Table A.1 lists the quantities as used in the simulations and their equivalent experimental values as defined by Eqs. (A.6) and (A.7). For the purpose of easy comparison, lengths, velocities, and stresses are expressed by their equivalent experimental values throughout this chapter.

A.2.2 Hydrodynamic drag

A simplified setup consisting only of wire, ingot and PEG without SiC grains was used to test the hydrodynamic behavior of the fluid. Figure A.3b shows a frontal

snapshot of the simulation. The wire diameter is 100 μm and the groove width is chosen to be 140 μm according to a typical value of the kerf loss. The wire was dragged in y-direction at a velocity of 17 m/s and the velocity field of the fluid was evaluated. The result is shown in Fig. A.4. The velocity increases linearly from the surface of the ingot to the wire surface corresponding to a laminar flow regime, which is expected for Re = 3. Furthermore, it can be clearly seen that no-slip boundary conditions are fulfilled.

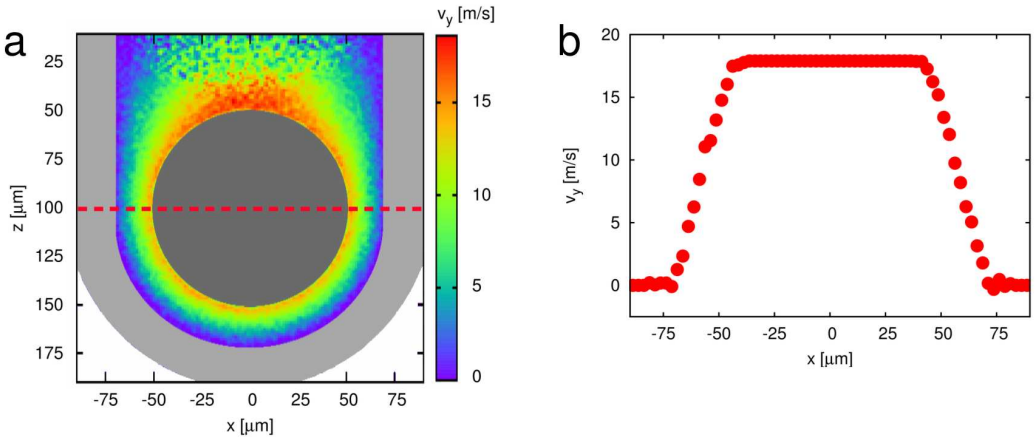

Figure A.4: Laminar flow of PEG: Color coded velocity field around wire (a) and velocity profile along the marked line (b).

A.2.3 Viscosity

Rheology measurements of pure PEG and a slurry with 25volume percent SiC grains showed that the slurry viscosity is about four times larger than the PEG viscosity. The same viscosity ratio is obtained in according simulations. No dependence of the viscosity on the shear rate is observed in experiments for sufficiently high shear rates, i.e. larger than 100 s^{-1}. Simulated viscosities are also shear rate-independent.

A.3 Wire sawing simulations

A.3.1 Setup

The model system used for the sawing simulations is similar to the one used for the hydrodynamic drag test described in Section A.2.2. Yet, in this case 25volume percent SiC grains are included (compare Fig. A.3c). The slurry is located initially in the cutting groove while the wire is positioned above the slurry surface. Then the

	v_y	
p_z	4.25 m/s	17 m/s
0.15 N/mm^2	23 μm	35 μm
1.5 N/mm^2	14 μm	*contact*

Table A.2: Average distance between wire and ingot depending on wire stress p_z and wire velocity v_y.

dynamic simulation starts and the wire is forced into the slurry due to an applied stress p_z while it is dragged with constant velocity v_y. The stress p_z is defined by the quotient of the normal force on the wire and the cross sectional area of the wire. The simulations are stopped after a stationary wire floating height is reached. Stress distributions on ingot and grains are sampled in the stationary regime. The combinations of two wire stresses ($p_z = 0.15$ or $1.5\,\mathrm{N/mm^2}$) and two wire velocities ($v_y = 4.25$ or $17\,\mathrm{m/s}$) were applied in the simulations.

A.3.2 Contact regimes

Reference [10] distinguishes for the steady state sawing process between a non-contact and a semi-contact regime on the basis of elasto-hydrodynamic modeling depending on wire stress and velocity. This distinction refers on the distance between wire and ingot surface with respect to the SiC grain size. Both regimes are observed in the particle based simulations. Average distances between wire and ingot surface in z-direction are listed in Table A.2. When applying a low stress and a high wire velocity, several layers of grains are located between wire and ingot, i.e. the system is in the non-contact regime (see Fig. A.5a). For a high wire stress at a low velocity semi-contact is observed (see Fig. A.5b): Grains within a single layer are in contact with both the wire and the ingot. At low stress and low velocity an intermediate regime exists where only the biggest grains are in contact with wire and ingot. High stress and high velocity yield direct contact between the wire and the ingot.

A.3.3 Stress on ingot surface

The stress exerted from the SiC grains on the surface of the ingot groove was tracked during the simulations. The stress was averaged over time and along the y-coordinate because the system is translationally invariant in that direction. Figure A.6 shows distributions of the stress normal to the ingot surface along the tangential coordinate of the groove in the non-contact and semi-contact regime. The stress distribution is strongly localized around the center of the groove in the case of semi-contact. In the non-contact regime the stress is evenly distributed

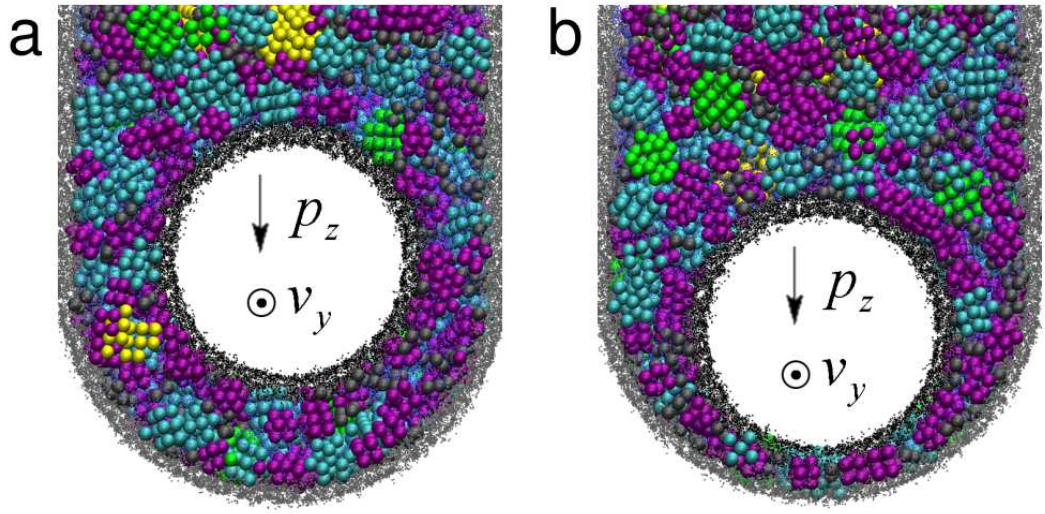

Figure A.5: (a): Non-contact regime at low wire stress and high velocity. (b): Semi-contact regime at high stress and low velocity.

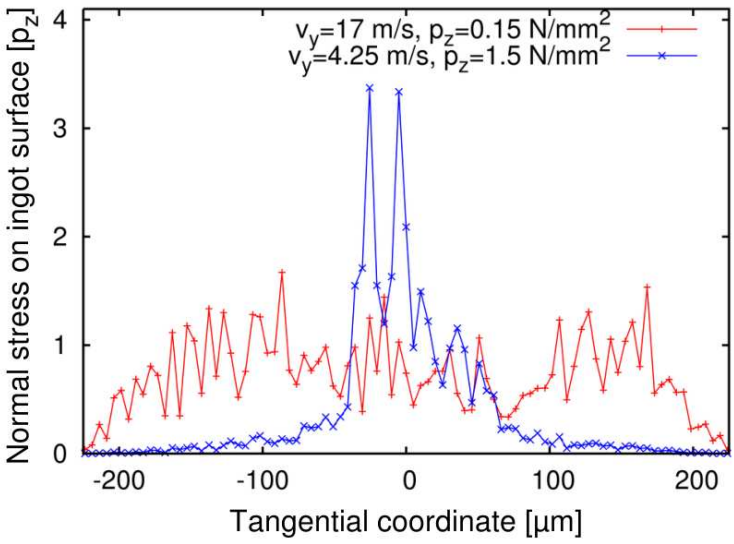

Figure A.6: Stress distribution along the ingot groove for non-contact (red) and semi-contact (blue) regime. The tangential coordinate is defined in Fig. A.3a.

along the surface. Note, that the distributions are normalized by the applied wire stress p_z. Thus, the absolute normal stress exerted on the sides of the groove, i.e. for values of the tangential coordinate larger than $100\,\mu$m or smaller than $-100\,\mu$m, is comparable for both cases.

A.3.4 Stress on SiC grains

Compressive stresses on the SiC grains were evaluated complementary to the ingot stress analysis. Figure A.7 shows stress distributions for the different grain sizes. In the non-contact regime the distributions are alike for different grain sizes. Merely the distribution tails are wider for bigger grains. In the semi-contact regime the situation is different. Large grains undergo by far the highest stresses. A detailed analysis of the distributions is given in Tables A.3 and A.4, where the stresses are divided into three intervals for each grain size.

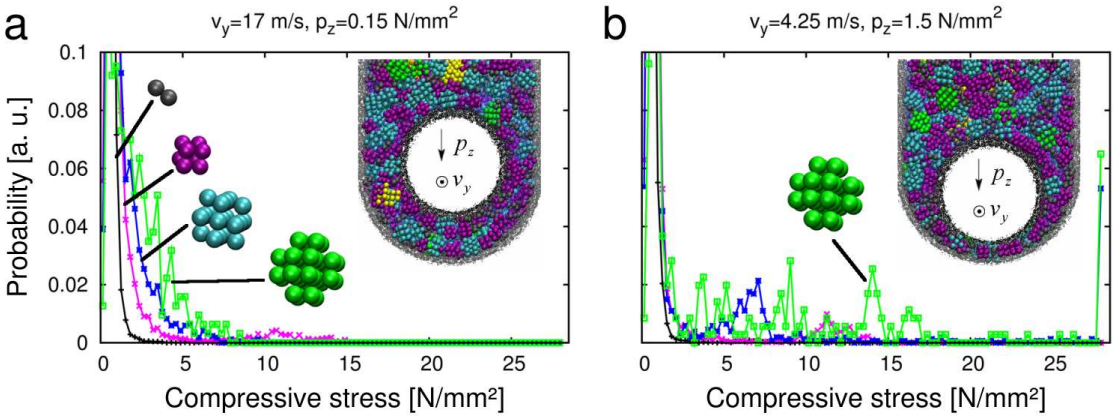

Figure A.7: Stress distributions for different grain sizes in the non-contact regime (a) and semi-contact regime (b). The peaks around $28\,\mathrm{N/mm^2}$ represent stresses higher than that value.

In Fig. A.8 the grain stress intervals from Table A.4 are spatially visualized. The highest stresses are exerted on the grains between the wire and the bottom of the groove.

	Compressive stress		
Grain diameter [μm]	low	medium	high
6 (black)	99.9 %	0.1 %	0.0 %
10 (purple)	94.7 %	5.3 %	0.0 %
14 (cyan)	96.7 %	3.3 %	0.0 %
20 (green)	92.7 %	7.3 %	0.0 %

Table A.3: Cumulated stress distributions for different grain sizes in the non-contact regime. Stress intervals: low $\leq$ 5N/mm^2 $<$ medium $\leq$ 25N/mm^2 $<$ high. Simulation with $v_y = 17\,\mathrm{m/s}$, $p_z = 0.15\,\mathrm{N/mm^2}$.

	Compressive stress		
Grain diameter [μm]	low	medium	high
6 (black)	98.9 %	1.1 %	0.0 %
10 (purple)	92.9 %	7.1 %	0.0 %
14 (cyan)	78.4 %	15.8 %	5.8 %
20 (green)	59.9 %	33.0 %	7.1 %

Table A.4: Same as Table A.3, but for simulation with $v_y = 4.25\,\mathrm{m/s}$, $p_z = 1.5\,\mathrm{N/mm^2}$; semi-contact regime.

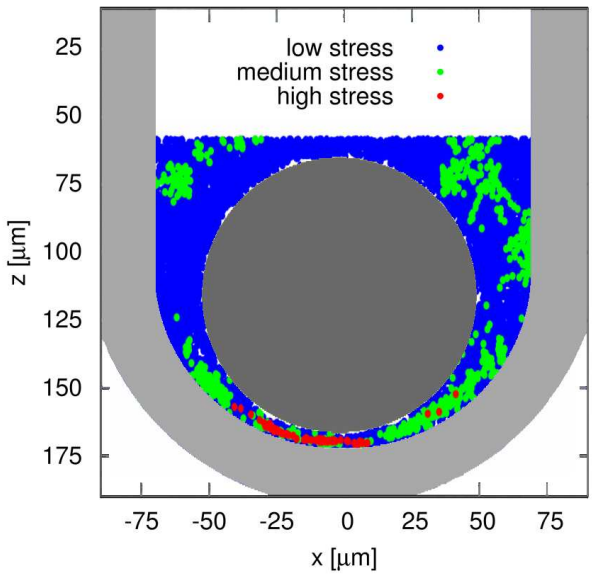

Figure A.8: Spatial occurrence of different compressive stress levels on SiC grains in the semi-contact regime.

A.4 Conclusion

The non-contact and the semi-contact sawing regime could be observed in the particle based simulations. Furthermore, the occurrence of semi-contact (non-contact) for high wire loads and low wire velocities (low loads and high velocities) is in agreement with predictions from elasto-hydrodynamic modeling [10]. It was found that in the semi-contact regime a large share of the applied normal stress on the wire is transmitted directly to the ground of the groove. In the non-contact case the stress exerted on the ingot is evenly distributed along the ground and the sides of the groove. Thus, it might be assumed that the abrasion is rather localized in the semi-contact regime, which would imply less kerf loss. However, this has to be checked by explicit modeling of fracture events at the ingot surface.

Furthermore, the simulation of the semi-contact regime shows that the largest SiC grains endure the highest compressive stresses. These stresses occur at the ground of the groove. Experiments [132] show a decrease of wafer strength and an increase of wafer roughness with increased normal stress on the wire. The simulations support these findings by assuming that for high wire stresses the semi-contact regime is reached. In this case the ingot could be significantly damaged due to localized strong impacts of SiC grains.

B Numerical solution of partial differential equations

The (compressible) kinematic modeling approach of granular outflow (Section 5.1) is mathematically expressed via partial differential equations (PDEs). Instead of solving the PDEs (5.4) and (5.9) implicitly, a time dependency is artificially introduced by means of a relaxation ansatz. Thus, Eq. (5.4) transforms into

$$\frac{\partial v_z}{\partial t} = v_\mathrm{r} \left(B \frac{\partial^2 v_z}{\partial x^2} - \frac{\partial v_z}{\partial z} \right). \tag{B.1}$$

Equation (5.9) transforms analogously into

$$\frac{\partial v_z}{\partial t} = v_\mathrm{r} \left(\left(n \frac{\partial B(n)}{\partial n} + B(n) \right) \frac{\partial n}{\partial x} \frac{\partial v_z}{\partial x} + B(n) n \frac{\partial^2 v_z}{\partial x^2} - n \frac{\partial v_z}{\partial z} - v_z \frac{\partial n}{\partial z} \right). \tag{B.2}$$

The velocity $v_\mathrm{r} = 2\,\mathrm{m/s}$ is introduced as a relaxation constant. The stationary solutions, $v_z(t \to \infty)$, of Eqs. (B.1) and (B.2) do also solve the original (C)KM problem without time dependency. The horizontal velocity component, v_x, can then be computed via Eqs. (5.2) and (5.7), respectively.

Equations (B.1) and (B.2) were solved numerically using finite differences on a *staggered grid* [77]. Details of the algorithm are given in the following. Figure B.1 shows an exemplary grid covering the computational domain where the PDEs are to be solved. The most simple way of discretization would be to evaluate each quantity of interest (i.e. v_x, v_z, n) at the grid cell centers. However, numerically more accurate is the so-called staggered grid approach. Thereby, only scalar values are kept track of at the cell centers while the components of vector quantities are shifted towards the cell edges (or cell faces in three dimensions).

An exemplary cell for the present problem is depicted in Fig. B.2. The cell edge lengths are $\Delta x = 0.25\,\mathrm{mm}$ and $\Delta z = 0.25\,\mathrm{mm}$ while the time is discretized in steps of $\Delta\tau = 1\,\mu\mathrm{s}$. To simplify the notation, the quantities v_x, v_z, and n are indexed using integer and half-integer values, e.g. $v_z(i + 1/2, j, k) = v_z((i + 1/2)\Delta x, j\Delta z, k\Delta\tau)$.

The spatial computational domain is limited by $i_\mathrm{min} = -l/(2\Delta x)$, $i_\mathrm{max} = l/(2\Delta x)$, $j_\mathrm{min} = 0$, and $j_\mathrm{max} = h/\Delta z$, where l is the hopper width and $h = 20\,\mathrm{cm}$ is the hopper height. The calculations start at $k_\mathrm{start} = 0$ and finish at $k_\mathrm{end} = T/\Delta\tau$ with $T = 40\,\mathrm{ms}$. As boundary condition at j_min the velocity distribution obtained

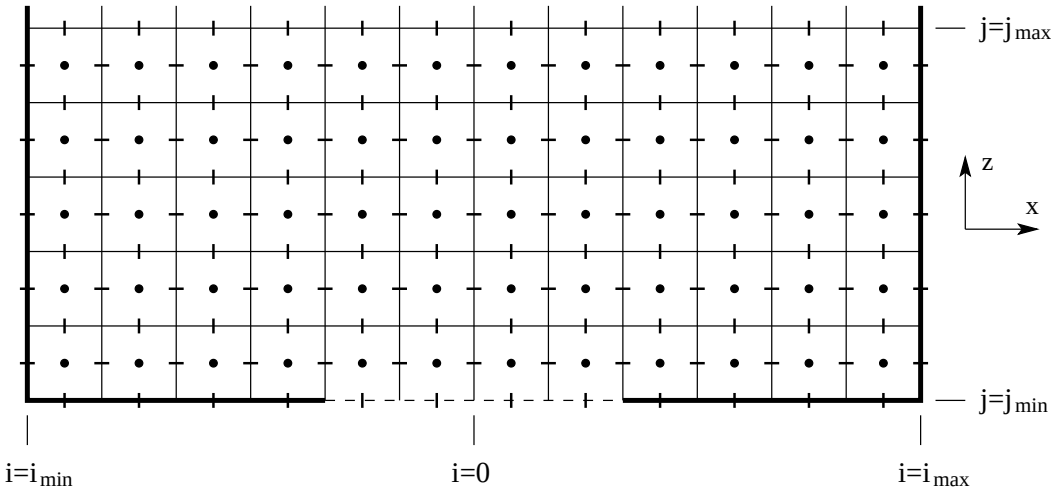

Figure B.1: Schematic of the staggered grid partition of the hopper for the solution of the KM and CKM equations via finite differences. The thick outline symbolizes the hopper walls while the dashed line represents the slit orifice (compare Fig. 5.1). Note that a finer discretization is used for the actual computation.

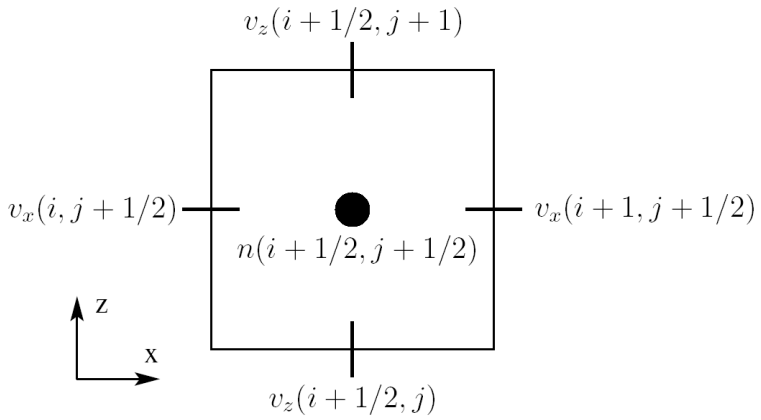

Figure B.2: A single staggered grid cell. The volume fraction, n, is evaluated at the cell center while the velocity components, v_x and v_z, are evaluated at the centers of the corresponding cell edges.

from the DEM simulations is assigned to the vertical velocity component. All other velocities are set to zero at k_{start}. At $i_{\min}$ and $i_{\max}$ the boundary conditions are $v_x = 0$. No boundary condition is used at $j_{\max}$. Instead, an upwind (or forward) difference is used, which propagates the initial *perturbation* at $j_{\min}$ through the domain in $+z$-direction.

Finite difference scheme for kinematic modeling

Apart form the domain boundaries, i.e. $i \in [i_{\min}+1, i_{\min}+2, \ldots, i_{\max}-2]$ and $j \in [1, 2, \ldots, j_{\max}]$, the time integration of Eq. (B.1) is given by

$$\begin{aligned} v_z(i+1/2, j, k+1) &= v_z(i+1/2, j, k) + \Delta\tau v_{\text{r}} \\ &\times \left(B \frac{v_z(i+3/2, j, k) - 2v_z(i+1/2, j, k) + v_z(i-1/2, j, k)}{\Delta x^2} \right. \\ &\left. - \frac{v_z(i+1/2, j, k) - v_z(i+1/2, j-1, k)}{\Delta z} \right). \end{aligned} \tag{B.3}$$

The upwind method is expressed by the asymmetric finite difference stencil for $\partial v_z / \partial z$ with respect to j.

The boundary condition $v_x = 0$, which results in $v_z(i_{\min} - 1/2, j, k) = v_z(i_{\min} + 1/2, j, k)$ and $v_z(i_{\max} - 1/2, j, k) = v_z(i_{\max} + 1/2, j, k)$ via Eq. (5.2), is satisfied at the left hopper wall via

$$\begin{aligned} v_z(i_{\min}+1/2, j, k+1) &= v_z(i_{\min}+1/2, j, k) + \Delta\tau v_{\text{r}} \\ &\times \left(B \frac{v_z(i_{\min}+3/2, j, k) - v_z(i_{\min}+1/2, j, k)}{\Delta x^2} \right. \\ &\left. - \frac{v_z(i_{\min}+1/2, j, k) - v_z(i_{\min}+1/2, j-1, k)}{\Delta z} \right), \end{aligned} \tag{B.4}$$

and at the right wall via

$$\begin{aligned} v_z(i_{\max}-1/2, j, k+1) &= v_z(i_{\max}-1/2, j, k) + \Delta\tau v_{\text{r}} \\ &\times \left(B \frac{-v_z(i_{\max}-1/2, j, k) + v_z(i_{\max}-3/2, j, k)}{\Delta x^2} \right. \\ &\left. - \frac{v_z(i_{\max}-1/2, j, k) - v_z(i_{\max}-1/2, j-1, k)}{\Delta z} \right). \end{aligned} \tag{B.5}$$

Equations (B.4) and (B.5) are applied to $j \in [1, 2, \ldots, j_{\max}]$.

The horizontal velocity component is computed via Eq. (5.2), resulting in

$$\begin{aligned} v_x(i, j+1/2, k) = & -\frac{B}{2}\frac{v_z(i+1/2, j, k) - v_z(i-1/2, j, k)}{\Delta x} \\ & -\frac{B}{2}\frac{v_z(i+1/2, j+1, k) - v_z(i-1/2, j+1, k)}{\Delta x}. \end{aligned} \tag{B.6}$$

The according index ranges are $i \in [i_{\min}+1, i_{\min}+2, \ldots, i_{\max}-1]$ and $j \in [0, 1, \ldots, j_{\max}-1]$.

Finite difference scheme for compressible kinematic modeling

The time-dependent CKM problem, Eq. (B.2), is solved via

$$\begin{aligned} & v_z(i+1/2, j, k+1) = v_z(i+1/2, j, k) + \Delta\tau v_{\mathrm{r}} \\ & \times \left\{ \left(\frac{n(i+1/2, j+1/2) + n(i+1/2, j-1/2)}{2} \right.\right. \\ & \times \frac{B'\left(n(i+1/2, j+1/2)\right) + B'\left(n(i+1/2, j-1/2)\right)}{2} \\ & \left.\left. + \frac{B\left(n(i+1/2, j+1/2)\right) + B\left(n(i+1/2, j-1/2)\right)}{2} \right) \right. \\ & \times \left(\frac{1}{2}\frac{n(i+3/2, j-1/2) - n(i-1/2, j-1/2)}{2\Delta x} \right. \\ & \left. + \frac{1}{2}\frac{n(i+3/2, j+1/2) - n(i-1/2, j+1/2)}{2\Delta x} \right) \\ & \times \frac{v_z(i+3/2, j, k) - v_z(i-1/2, j, k)}{2\Delta x} \\ & + \frac{B\left(n(i+1/2, j+1/2)\right) + B\left(n(i+1/2, j-1/2)\right)}{2} \\ & \times \frac{n(i+1/2, j+1/2) + n(i+1/2, j-1/2)}{2} \\ & \times \frac{v_z(i+3/2, j, k) - 2v_z(i+1/2, j, k) + v_z(i-1/2, j, k)}{\Delta x^2} \\ & - \frac{n(i+1/2, j+1/2) + n(i+1/2, j-1/2)}{2} \\ & \times \frac{v_z(i+1/2, j, k) - v_z(i+1/2, j-1, k)}{\Delta z} \\ & \left. - v_z(i+1/2, j, k)\frac{n(i+1/2, j+1/2) - n(i+1/2, j-1/2)}{\Delta z} \right\}, \end{aligned} \tag{B.7}$$

with $B'(n) = \mathrm{d}B(n)/\mathrm{d}n$. The indices i and j take the same values as in the KM case.

The boundary condition $v_x = 0$ yields

$$\begin{aligned}
&v_z(i_{\min}+1/2,j,k+1) = v_z(i_{\min}+1/2,j,k) + \Delta\tau v_{\mathrm{r}} \\
&\times \left(\frac{B\left(n(i_{\min}+1/2,j+1/2)\right) + B\left(n(i_{\min}+1/2,j-1/2)\right)}{2} \right. \\
&\times \frac{n(i_{\min}+1/2,j+1/2) + n(i_{\min}+1/2,j-1/2)}{2} \\
&\times \frac{v_z(i_{\min}+3/2,j,k) - v_z(i_{\min}+1/2,j,k)}{\Delta x^2} \\
&- \frac{n(i_{\min}+1/2,j+1/2) + n(i_{\min}+1/2,j-1/2)}{2} \\
&\times \frac{v_z(i_{\min}+1/2,j,k) - v_z(i_{\min}+1/2,j-1,k)}{\Delta z} \\
&\left. - v_z(i_{\min}+1/2,j,k) \frac{n(i_{\min}+1/2,j+1/2) - n(i_{\min}+1/2,j-1/2)}{\Delta z} \right).
\end{aligned} \tag{B.8}$$

at the left wall and

$$\begin{aligned}
&v_z(i_{\max}-1/2,j,k+1) = v_z(i_{\max}-1/2,j,k) + \Delta\tau v_{\mathrm{r}} \\
&\times \left(\frac{B\left(n(i_{\max}-1/2,j+1/2)\right) + B\left(n(i_{\max}-1/2,j-1/2)\right)}{2} \right. \\
&\times \frac{n(i_{\max}-1/2,j+1/2) + n(i_{\max}-1/2,j-1/2)}{2} \\
&\times \frac{-v_z(i_{\max}-1/2,j,k) + v_z(i_{\max}-3/2,j,k)}{\Delta x^2} \\
&- \frac{n(i_{\max}-1/2,j+1/2) + n(i_{\max}-1/2,j-1/2)}{2} \\
&\times \frac{v_z(i_{\max}-1/2,j,k) - v_z(i_{\max}-1/2,j-1,k)}{\Delta z} \\
&\left. - v_z(i_{\max}-1/2,j,k) \frac{n(i_{\max}-1/2,j+1/2) - n(i_{\max}-1/2,j-1/2)}{\Delta z} \right).
\end{aligned} \tag{B.9}$$

at the right wall.

Equation (5.7) leads to

$$\begin{aligned} v_x(i, j+1/2, k) = & -\frac{B\left(n(i+1/2, j+1/2)\right) + B\left(n(i-1/2, j+1/2)\right)}{2} \\ & \times \left(\frac{1}{2} \frac{v_z(i+1/2, j, k) - v_z(i-1/2, j, k)}{\Delta x} \right. \\ & \left. + \frac{1}{2} \frac{v_z(i+1/2, j+1, k) - v_z(i-1/2, j+1, k)}{\Delta x} \right) \end{aligned} \tag{B.10}$$

in order to compute the horizontal velocity component.

C Simulation parameters

This appendix contains a compilation of the used parameters for all simulations carried out within this thesis unless already specified in the main text.

Parameter	Value
R [m]	$7.84 \cdot 10^{-5}$, $1.568 \cdot 10^{-4}$ and $3.136 \cdot 10^{-4}$
d [m]	$4.7 \cdot 10^{-4}$, $9.4 \cdot 10^{-4}$ and $1.88 \cdot 10^{-3}$
m [kg]	$7.6 \cdot 10^{-8}$, $6.1 \cdot 10^{-7}$ and $4.9 \cdot 10^{-6}$
$\tilde{E}$ [Pa]	10^7
γ_n/R [Pa s/m]	10^5
κ_t/R [Pa]	10^6
w/R [J/m^3]	128
μ [ ]	1.0
μ_a [Pa s]	$2 \cdot 10^{-5}$
Δt [s]	$2.5 \cdot 10^{-7}$

Table C.1: Parameters used for the grain-grain collision simulations (Fig. 3.1). The radius R refers to the basic spheres, while the diameter d and the mass m refer to the composed grains. Fixed values for the cases of inadequate force scaling: $\gamma_\mathrm{n} = 7.8\,\mathrm{Pa\,s}$, $\kappa_\mathrm{t} = 78\,\mathrm{N/m}$ and $w = 1.0 \cdot 10^{-2}\,\mathrm{J/m^2}$, respectively.

Parameter	Adequate scaling		Inadequate scaling		
	non-cohesive	cohesive	γ_n = const.	κ_t = const.	w = const.
γ_n/R [Pa s/m]	10^5	10^5	—	10^5	10^5
γ_n [Pa s]	—	—	7.8	—	—
κ_t/R [Pa]	10^6	10^6	10^6	—	10^6
κ_t [N/m]	—	—	—	78	—
w/R [J/m^3]	0	128	0	0	—
w [J/m^2]	—	—	—	—	$1.0 \cdot 10^{-2}$
μ [ ]	0.5	1.0	0.5	0.5	1.0
R_w [m]			R		
μ_w [ ]			0.15		
w_w [J/m^2]			0		
g [m/s^2]			9.81		

Table C.2: Parameters used for the bulk formation simulations (Figs. 3.2, 3.3, and 3.4). R, d, m, $\tilde{E}$, μ_a and Δt take the same values as listed in Table C.1.

Parameter	Model A	Model D		
	non-cohesive	non-cohesive	$w \propto R$	$w = \text{const.}$
$\tilde{E}$ [Pa]		10^7		
γ_n/R [Pa s/m]		10^6		
κ_t/R [Pa]		10^6		
w/R [J/m^3]	0	0	128	—
w [J/m^2]	—	—	—	$1.0 \cdot 10^{-2}$
μ [ ]	0.5	0.5	1.0	1.0
R_w [m]		$1.5 \cdot 10^{-4}$		
μ_w [ ]		0.15		
w_w [J/m^2]		0		
g [m/s^2]		9.81		
μ_a [Pa s]		$2 \cdot 10^{-5}$		
Δt [s]		$2 \cdot 10^{-6}$		

Table C.3: Parameters used for the slit discharge and angle of repose simulations (Figs. 3.5, 3.6, and 3.7). For model A $d = 2R$ while for model D $d = 6R$.

Model:	A	B	C	D
Parameter	Value			
R [m]	$1.5 \cdot 10^{-4}$	$1.5 \cdot 10^{-4}$	$8.9 \cdot 10^{-5}$	$7.84 \cdot 10^{-5}$
d [m]	$3.0 \cdot 10^{-4}$	$3.0 \cdot 10^{-4}$	$3.56 \cdot 10^{-4}$	$4.7 \cdot 10^{-4}$
m [kg]	$7.63 \cdot 10^{-8}$			
$\tilde{E}$ [Pa]	10^7			
γ_n/R [Pa s/m]	10^6			
κ_t/R [Pa]	10^6			
R_w [m]	$1.5 \cdot 10^{-4}$			
μ_w [ ]	0.15			
w_w [J/m^2]	0			
g [m/s^2]	9.81			
μ_a [Pa s]	$2 \cdot 10^{-5}$			
Δt [s]	$2 \cdot 10^{-6}$			

Table C.4: Parameters used for the simulations of slit discharge, angle of repose formation, and cavity filling in Chapter 4. For models C and D the radius R refers to the constituent spheres while d and m refer to the complete grains for all models.

Parameter	Value
R [m]	$7.84 \cdot 10^{-5}$
d [m]	$4.7 \cdot 10^{-4}$
m [kg]	$7.63 \cdot 10^{-8}$
$\tilde{E}$ [Pa]	10^7
γ_n/R [Pa s/m]	10^6
κ_t/R [Pa]	10^6
w [J/m^2]	0.0
μ [ ]	0.5
R_w [m]	$1.5 \cdot 10^{-4}$
μ_w [ ]	0.15
w_w [J/m^2]	0.0
g [m/s^2]	9.81
μ_a [Pa s]	$2 \cdot 10^{-5}$
Δt [s]	$2 \cdot 10^{-6}$

Table C.5: Parameters used for the hopper and feeding shoe discharge simulations in Chapter 5.

Parameter	Value
R [m]	$7.84 \cdot 10^{-5}$, $1.568 \cdot 10^{-4}$ or $3.136 \cdot 10^{-4}$
d [m]	$4.7 \cdot 10^{-4}$, $9.4 \cdot 10^{-4}$ or $1.88 \cdot 10^{-3}$
m [kg]	$7.63 \cdot 10^{-8}$, $6.104 \cdot 10^{-7}$ or $4.883 \cdot 10^{-6}$
$\tilde{E}$ [Pa]	10^7
γ_n/R [Pa s/m]	10^6
κ_t/R [Pa]	10^6
w/R [J/m^3]	63.8
μ [ ]	1.0
R_w [m]	$1.5 \cdot 10^{-4}$
μ_w [ ]	0.15
w_w [J/m^2]	0.0
g [m/s^2]	9.81
μ_a [Pa s]	$2 \cdot 10^{-5}$
Δt [s]	$2 \cdot 10^{-6}$

Table C.6: Parameters used for the cavity filling simulations in Chapter 6.

Parameter	Numerical value	Corresponds to
r_c	1.0	$1.1\,\mathrm{nm}$
m	1.0	$3.3 \cdot 10^{-25}\,\mathrm{kg}$
$(k_\mathrm{B}T)'$	1.0	$4.1 \cdot 10^{-21}\,\mathrm{J}$ $(= k_\mathrm{B}T)$
Δt	$0.01\,\tau$	$60\,\mathrm{fs}$
ρ	4.15	
K	0.5	
σ_R	3.0	
κ	$1.0 \cdot 10^3$	

Table C.7: Parameters used for the wire sawing simulations in Appendix A.

Bibliography

[1] I. S. Aranson and L. S. Tsimring. Patterns and collective behavior in granular media: Theoretical concepts. *Rev. Mod. Phys.*, 78(2):641–692, 2006.

[2] E. Teunou, J. J. Fitzpatrick, and E. C. Synnott. Characterisation of food powder flowability. *J. Food Eng.*, 39(1):31–37, 1999.

[3] M. E. Möbius, B. E. Lauderdale, S. R. Nagel, and H. M. Jaeger. Brazil-nut effect — Size separation of granular particles. *Nature*, 414:270, 2001.

[4] A. D. Salman, M. J. Hounslow, and J. P. K. Seville, editors. *Handbook of Powder Technology — Volume 11: Granulation*. Elsevier Science, 2007.

[5] C. J. Brown and J. Nielsen, editors. *Silos: Fundamentals of Theory, Behaviour and Design*. Taylor & Francis, 1998.

[6] D. Schulze. *Pulver und Schüttgüter — Fließeigenschaften und Handhabung*. Springer, 2006.

[7] W. Schatt and K.-P. Wieters. *Powder Metallurgy: Processing and Materials*. European Powder Metallurgy Association, 1997.

[8] D. Whittaker. PM structural parts move to higher density and performance. *Powder Metall.*, 50(2):99–105, 2007.

[9] M. Kobayashi, T. Matsui, and Y. Murakami. Mechanism of creation of compressive residual stress by shot peening. *Int. J. Fatigue*, 20(5):351–357, 1998.

[10] H. J. Möller. Basic mechanisms and models of multi-wire sawing. *Adv. Eng. Mater.*, 6(7):501–513, 2004.

[11] P. G. de Gennes. Granular matter: a tentative view. *Rev. Mod. Phys.*, 71(2):S374–S382, 1999.

[12] H. M. Jaeger, S. R. Nagel, and R. P. Behringer. Granular solids, liquids, and gases. *Rev. Mod. Phys.*, 68(4):1259–1273, 1996.

[13] L. P. Kadanoff. Built upon sand: Theoretical ideas inspired by granular flows. *Rev. Mod. Phys.*, 71(1):435–444, 1999.

[14] R. M. Nedderman. *Statics and Kinematics of Granular Materials*. Cambridge University Press, 1992.

[15] T. S. Majmudar and R. P. Behringer. Contact force measurements and stress-induced anisotropy in granular materials. *Nature*, 435:1079–1082, 2005.

[16] R. Y. Yang, R. P. Zou, and A. B. Yu. Computer simulation of the packing of fine particles. *Phys. Rev. E*, 62(3):3900–3908, 2000.

[17] J. B. Knight, C. G. Fandrich, C. N. Lau, H. M. Jaeger, and S. R. Nagel. Density relaxation in a vibrated granular material. *Phys. Rev. E*, 51(5):3957–3963, 1995.

[18] D. M. Wood. *Soil Behaviour and Critical State Soil Mechanics*. Cambridge University Press, 1990.

[19] F. A. Gilabert, J.-N. Roux, and A. Castellanos. Computer simulation of model cohesive powders: Plastic consolidation, structural changes and elasticity under isotropic loads. *Phys. Rev. E*, 78(3):031305, 2008.

[20] W. A. Beverloo, H. A. Leniger, and J. Van de Velde. The flow of granular solids through orifices. *Chem. Eng. Sci.*, 15:260–269, 1961.

[21] H. A. Janssen. Versuche über Getreidedruck in Silozellen. *Z. Ver. Dtsch. Ing.*, 39(35):1045–1049, 1895.

[22] C. A. Coulomb. Essai sur une application des règles de maximis & minimis à quelques problèmes de statique, relatifs à l'architecture. *Mem. de Math. de l'Acad. Royale des Science*, 7:343–387, 1776.

[23] A. W. Jenike. A theory of flow of particulate solids in converging and diverging channels based on a conical yield function. *Powder Technol.*, 50(3):229–236, 1987.

[24] GDR MiDi. On dense granular flows. *Eur. Phys. J. E*, 14(4):341–365, 2004.

[25] P. Jop, Y. Forterre, and O. Pouliquen. A constitutive law for dense granular flows. *Nature*, 441(7094):727–730, 2006.

[26] S. F. Edwards and R. B. S. Oakeshott. Theory of powders. *Physica A*, 157(3):1080–1090, 1989.

[27] A. Mehta and S. F. Edwards. Statistical mechanics of powder mixtures. *Physica A*, 157(3):1091–1100, 1989.

[28] P. Richard, M. Nicodemi, R. Delannay, P. Ribière, and D. Bideau. Slow relaxation and compaction of granular systems. *Nat. Mater.*, 4:121–128, 2005.

[29] C. Y. Wu and A. C. F. Cocks. Flow behaviour of powders during die filling. *Powder Metall.*, 47(2):127–136, 2004.

[30] R. M. German. *Sintering Theory and Practice*. Wiley-VCH, 1996.

[31] S. F. Burch, A. C. F. Cocks, J. M. Prado, and J. H. Tweed. *Modelling of Powder Die Compaction*, chapter 9 — Die Fill and Powder Transfer. Springer, 2007.

[32] D. Korachkin, D. T. Gethin, R. W. Lewis, and J. H. Tweed. Effect of Die Filling on Powder Compaction. *Int. J. Powder Metall.*, 44(1):22–34, 2008.

[33] X. Xie and V. M. Puri. Uniformity of Powder Die Filling Using a Feed Shoe: A Review. *Part. Sci. Technol.*, 24(4):411–426, 2006.

[34] P. A. Cundall and O. D. L. Strack. A discrete numerical model for granular assemblies. *Geotechnique*, 29(1):47–65, 1979.

[35] C. S. Campbell and C. E. Brennen. Computer simulation of granular shear flows. *J. Fluid Mech.*, 151:167–188, 1985.

[36] O. R. Walton and R. L. Braun. Stress calculations for assemblies of inelastic speres in uniform shear. *Acta Mech.*, 63(1):73–86, 1986.

[37] P. K. Haff and B. T. Werner. Computer simulation of the mechanical sorting of grains. *Powder Technol.*, 48(3):239–245, 1986.

[38] J. A. C. Gallas, H. J. Herrmann, and S. Sokołowski. Convection cells in vibrating granular media. *Phys. Rev. Lett.*, 69(9):1371–1374, 1992.

[39] R. García-Rojo, H. J. Herrmann, and S. McNamara, editors. *Powders and Grains 2005*, Leiden, 2005. Balkema.

[40] T. Pöschel and V. Buchholtz. Static Friction Phenomena in Granular Materials: Coulomb Law versus Particle Geometry. *Phys. Rev. Lett.*, 71(24):3963–3966, 1993.

[41] P. W. Cleary and M. L. Sawley. DEM modelling of industrial granular flows: 3D case studies and the effect of particle shape on hopper discharge. *Appl. Math. Model.*, 26(2):89–111, 2002.

[42] J.-P. Latham and A. Munjiza. The modelling of particle systems with real shapes. *Philos. Trans. R. Soc. London, Ser. A*, 362(1822):1953–1972, 2004.

[43] R. M. Nedderman and U. Tüzün. A Kinematic Model for the Flow of Granular Materials. *Powder Technol.*, 22(2):243–253, 1979.

[44] P. J. Hoogerbrugge and J. M. V. A. Koelman. Simulating microscopic hydrodynamic phenomena with dissipative particle dynamics. *Europhys. Lett.*, 19(3):155–160, 1992.

[45] M. P. Allen and D. J. Tildesley. *Computer Simulation of Liquids*. Oxford University Press, 1987.

[46] D. C. Rapaport. *The Art of Molecular Dynamics Simulation*. Cambridge University Press, 2004.

[47] B. D. Lubachevsky. How to Simulate Billiards and Similar Systems. *J. Comput. Phys.*, 94(2):255–283, 1991.

[48] B. Bernu and R. Mazighi. One-dimensional bounce of inelastically colliding marbles on a wall. *J. Phys. A*, 23:5745–5754, 1990.

[49] J. Schäfer, S. Dippel, and D. E. Wolf. Force schemes in simulations of granular materials. *J. Phys. I*, 6:5–20, 1996.

[50] S. Luding. About contact force-laws for cohesive frictional materials in 2D and 3D. In *Behavior of Granular Media*, pages 137–147. Shaker Verlag, 2006.

[51] H. Kruggel-Emden, E. Simsek, S. Rickelt, S. Wirtz, and V. Scherer. Review and extension of normal force models for the Discrete Element Method. *Powder Technol.*, 171(3):157–173, 2007.

[52] H. P. Zhu, Z. Y. Zhou, R. Y. Yang, and A. B. Yu. Discrete particle simulation of particulate systems: Theoretical developments. *Chem. Eng. Sci.*, 62(13):3378–3396, 2007.

[53] H. Hertz. Über die Berührung fester elastischer Körper. *J. reine angew. Math.*, 92:156–171, 1881.

[54] K. L. Johnson, K. Kendall, and A. D. Roberts. Surface energy and the contact of elastic solids. *Proc. R. Soc. London, Ser. A*, 324(1558):301–313, 1971.

[55] J. N. Israelachvili. The calculation of can der Waals dispersion forces between macroscopic bodies. *Proc. R. Soc. London, Ser. A*, 331(1584):39–55, 1972.

[56] C. V. Raman. The Photographic Study of Impact at Minimal Velocities. *Phys. Rev.*, 12(6):442–447, 1918.

[57] E. D. Landau and E. M. Lifshitz. *Theory of Elasticity*. Pergamon Press, 1970.

[58] Y. C. Zhou, B. D. Wright, R. Y. Yang, B. H. Xu, and A. B. Yu. Rolling friction in the dynamic simulation of sandpile formation. *Physica A*, 269(2):536–553, 1999.

[59] I. P. Omelyan. On the numerical integration of motion for rigid polyatomics: The modified quaternion approach. *Comput. Phys.*, 12(1):97–103, 1998.

[60] H. Goldstein. *Classical Mechanics*. Addison-Wesley, 1950.

[61] D. J. Evans and S. Murad. Singularity free algorithm for molecular dynamics simulation of rigid polyatomics. *Mol. Phys.*, 34(2):327–331, 1977.

[62] B. Henrich, A. Wonisch, T. Kraft, M. Moseler, and H. Riedel. Simulations of the influence of rearrangement during sintering. *Acta Mater.*, 55(2):753–762, 2007.

[63] G. L. Dirichlet. Über die Reduction der positiven quadratischen Formen mit drei unbestimmten ganzen Zahlen. *J. reine angew. Math.*, 40:209–227, 1850.

[64] G. Voronoï. Nouvelles applications des paramètres continus à la théorie des formes quadratiques — Premier Mémoire. Sur quelques propriétés des formes quadratiques positives parfaites. *J. reine angew. Math.*, 133:97–178, 1907.

[65] G. Voronoï. Nouvelles applications des paramètres continus à la théorie des formes quadratiques — Deuxième Mémoire. Recherches sur les parallélloèdres primitifs. *J. reine angew. Math.*, 134:198–287, 1908.

[66] C. H. Rycroft, G. S. Grest, J. W. Landry, and M. Z. Bazant. Analysis of granular flow in a pebble-bed nuclear reactor. *Phys. Rev. E*, 74(2):021306, 2006.

[67] E. Buckingham. On Physically Similar Systems; Illustrations of the Use of Dimensional Equations. *Phys. Rev.*, 4(4):345–376, 1914.

[68] G. F. Bocchini. Influence of small die width on filling and compacting densities. *Powder Metall.*, 30(4):261–266, 1987.

[69] J. J. Alonso and H. J. Herrmann. Shape of the Tail of a Two-Dimensional Sandpile. *Phys. Rev. Lett.*, 76(26):4911–4914, 1996.

[70] D. Hirshfeld, Y. Radzyner, and D. C. Rapaport. Molecular dynamics studies of granular flow through an aperture. *Phys. Rev. E*, 56(4):4404–4415, 1997.

[71] L. E. Silbert, D. Ertaş, G. S. Grest, T. C. Halsey, D. Levine, and S. J. Plimpton. Granular flow down an inclined plane: Bagnold scaling and rheology. *Phys. Rev. E*, 64(5):051302, 2001.

[72] M. Lätzel, S. Luding, and H. J. Herrmann. Macroscopic material properties from quasi-static, microscopic simulations of a two-dimensional shear-cell. *Granular Matter*, 2(3):123–135, 2000.

[73] Y. C. Zhou, B. H. Xu, A. B. Yu, and P. Zulli. Numerical investigation of the angle of repose of monosized spheres. *Phys. Rev. E*, 64(2):021301, 2001.

[74] C. Y. Wu, L. Dihoru, and A. C. F. Cocks. The flow of powder into simple and stepped dies. *Powder Technol.*, 134(1–2):24–39, 2003.

[75] L. C. R. Schneider, A. C. F. Cocks, and A. Apostolopoulos. Comparison of filling behaviour of metallic, ceramic, hardmetal and magnetic powders. *Powder Metall.*, 48(1):77–84, 2005.

[76] C. Y. Wu and A. C. F. Cocks. Numerical and experimental investigations of the flow of powder into a confined space. *Mech. Mater.*, 38(4):304–324, 2006.

[77] W. H. Press, S. A. Teukolsky, W. T. Vetterling, and B. P. Flannery. *Numerical recipes in FORTRAN: The Art of Scientific Computing*. Cambridge University Press, 1992.

[78] Y. Grasselli and H. J. Herrmann. On the angles of dry granular heaps. *Physica A*, 246(3):301–312, 1997.

[79] A. Samadani and A. Kudrolli. Angle of repose and segregation in cohesive granular matter. *Phys. Rev. E*, 64(5):051301, 2001.

[80] G. D. Scott. Packing of Spheres: Packing of Equal Spheres. *Nature*, 188(4754):908–909, 1960.

[81] G. Y. Onoda and E. G. Liniger. Random Loose Packings of Uniform Spheres and the Dilatancy Onset. *Phys. Rev. Lett.*, 64(22):2727–2730, 1990.

[82] G. H. Ristow. Outflow rate and wall stress for two-dimensional hoppers. *Physica A*, 235(3):319–326, 1997.

[83] C. L. Martin and R. K. Bordia. Influence of adhesion and friction on the geometry of packings of spherical particles. *Phys. Rev. E*, 77(3):031307, 2008.

[84] L. E. Silbert, D. Ertaş, G. S. Grest, T. C. Halsey, and D. Levine. Geometry of frictionless and frictional sphere packings. *Phys. Rev. E*, 65(3):031304, 2002.

[85] H. Kruggel-Emden, S. Rickelt, S. Wirtz, and V. Scherer. A study on the validity of the multi-sphere Discrete Element Method. *Powder Technol.*, 188(2):153–165, 2008.

[86] D. Korachkin, D. T. Gethin, and J. H. Tweed. Friction Measurement Using a Die Shear Plate Equipment. In *Proceedings of the EURO PM 2005, Volume 3, Prague, Czech Republic*, pages 369–375, Shrewsbury, UK, 2005. European Powder Metallurgy Association.

[87] R. Freeman. Measuring the flow properties of consolidated, conditioned and aerated powders — A comparative study using a powder rheometer and a rotational shear cell. *Powder Technol.*, 174(1–2):25–33, 2007.

[88] P.-A. Lemieux and D. J. Durian. From Avalanches to Fluid Flow: A Continuous Picture of Grain Dynamics Down a Heap. *Phys. Rev. Lett.*, 85(20):4273–4276, 2000.

[89] I. S. Aranson and L. S. Tsimring. Continuum theory of partially fluidized granular flows. *Phys. Rev. E*, 65(6):061303, 2002.

[90] L. E. Silbert, J. W. Landry, and G. S. Grest. Granular flow down a rough inclined plane: Transition between thin and thick piles. *Phys. Fluids*, 15:1–10, 2003.

[91] W. Bi, R. Delannay, P. Richard, N. Taberlet, and A. Valance. Two- and three-dimensional confined granular chute flows: experimental and numerical results. *J. Phys.: Condens. Matter*, 17(24):S2457–S2480, 2005.

[92] P. Jop, Y. Forterre, and O. Pouliquen. Crucial role of sidewalls in granular surface flows: consequences for the rheology. *J. Fluid Mech.*, 541:167–192, 2005.

[93] R. Delannay, M. Louge, P. Richard, N. Taberlet, and A. Valance. Towards a theoretical picture of dense granular flows down inclines. *Nat. Mater.*, 6(2):99–108, 2007.

[94] P. Richard, A. Valance, J.-F. Métayer, P. Sanchez, J. Crassous, M. Louge, and R. Delannay. Rheology of Confined Granular Flows: Scale Invariance, Glass Transition, and Friction Weakening. *Phys. Rev. Lett.*, 101:248002, 2008.

[95] R. M. Horne and R. M. Nedderman. Stress distribution in hoppers. *Powder Technol.*, 19(2):243–254, 1978.

[96] J. Choi, A. Kudrolli, and M. Z. Bazant. Velocity profile of granular flows inside silos and hoppers. *J. Phys.: Condens. Matter*, 17(24):S2533–S2548, 2005.

[97] I. Sielamowicz, S. Blonski, and T. A. Kowalewski. Optical technique DPIV in measurements of granular material flows, Part 1 of 3 — plane hoppers. *Chem. Eng. Sci.*, 60:589–598, 2005.

[98] J. Litwiniszyn. Statistical Methods in the Mechanics of Granular Bodies. *Rheol. Acta*, 1(2–3):146–150, 1958.

[99] W. W. Mullins. Stochastic Theory of Particle Flow under Gravity. *J. Appl. Phys.*, 43(2):665–678, 1972.

[100] A. Medina, J. A. Córdova, E. Luna, and C. Treviño. Velocity field measurements in granular gravity flow in a near 2D silo. *Phys. Lett. A*, 250(1–3):111–116, 1998.

[101] M. Z. Bazant. The Spot Model for random-packing dynamics. *Mech. Mater.*, 38(8–10):717–731, 2006.

[102] K. Kamrin and M. Z. Bazant. Stochastic flow rule for granular materials. *Phys. Rev. E*, 75(4):041301, 2007.

[103] C. H. Rycroft, M. Z. Bazant, G. S. Grest, and J. W. Landry. Dynamics of random packings in granular flow. *Phys. Rev. E*, 73(5):051306, 2006.

[104] L. C. R. Schneider, I. C. Sinka, and A. C. F. Cocks. Characterisation of the flow behaviour of pharmaceutical powders using a model die–shoe filling system. *Powder Technol.*, 173(1):59–71, 2007.

[105] W. W. Mullins. Experimental Evidence for the Stochastic Theory of Particle Flow Under Gravity. *Powder Technol.*, 9(1):29–37, 1974.

[106] U. Tüzün and R. M. Nedderman. Experimental Evidence Supporting Kinematic Modelling of the Flow of Granular Media in the Absence of Air Drag. *Powder Technol.*, 24(2):257–266, 1979.

[107] A. Samadani, A. Pradhan, and A. Kudrolli. Size segregation of granular matter in silo discharges. *Phys. Rev. E*, 60(6):7203–7209, 1999.

[108] J. Choi, A. Kudrolli, R. R. Rosales, and M. Z. Bazant. Diffusion and Mixing in Gravity-Driven Dense Granular Flows. *Phys. Rev. Lett.*, 92(17):174301, 2004.

[109] R. M. Nedderman, U. Tüzün, S. B. Savage, and G. T. Houlsby. The flow of granular materials - I: Discharge rates from hoppers. *Chem. Eng. Sci.*, 37:1597–1609, 1982.

[110] T. M. Verghese and R. M. Nedderman. The discharge of fine sands from conical hoppers. *Chem. Eng. Sci.*, 50(19):3143–3153, 1995.

[111] S. Humby, U. Tüzün, and A. B. Yu. Prediction of hopper discharge rates of binary granular mixtures. *Chem. Eng. Sci.*, 53(3):483–494, 1998.

[112] K. Chen, M. B. Stone, R. Barry, M. Lohr, W. McConville, K. Klein, B. L. Sheu, A. J. Morss, T. Scheidemantel, and P. Schiffer. Flux through a hole from a shaken granular medium. *Phys. Rev. E*, 74(1):011306, 2006.

[113] D. Huang, G. Sun, and K. Lu. Relationship between the flow rate and the packing fraction in the choke area of the two-dimensional granular flow. *Phys. Rev. E*, 74(6):061306, 2006.

[114] C. Mankoc, A. Janda, R. Arévalo, J. M. Pastor, I. Zuriguel, A. Garcimartín, and D. Maza. The flow rate of granular materials through an orifice. *Granular Matter*, 9(6):407–414, 2007.

[115] H. Pacheco-Martinez, H. J. van Gerner, and J. C. Ruiz-Suárez. Storage and discharge of a granular fluid. *Phys. Rev. E*, 77(2):021303, 2008.

[116] P. A. Langston, U. Tüzün, and D. M. Heyes. Continuous potential discrete particle simulations of stress and velocity fields in hoppers: Transition from fluid to granular flow. *Chem. Eng. Sci.*, 49(8):1259–1275, 1994.

[117] P. A. Langston, U. Tüzün, and D. M. Heyes. Discrete element simulation of granular flow in 2D and 3D hoppers: Dependence of discharge rate and wall stress on particle interactions. *Chem. Eng. Sci.*, 50(6):967–987, 1995.

[118] P. A. Langston, U. Tüzün, and D. M. Heyes. Distinct element simulation of interstitial air effects in axially symmetric granular flows in hoppers. *Chem. Eng. Sci.*, 51(6):873–891, 1996.

[119] R. Arévalo, A. Garcimartín, and D. Maza. A non-standard statistical approach to the silo discharge. *Eur. Phys. J. ST*, 143:191–197, 2007.

[120] C. Y. Wu, A. C. F. Cocks, and O. T. Gillia. Die filling and power transfer. *Int. J. Powder Metall.*, 39(4):51–64, 2003.

[121] Y. Guo, K. D. Kafui, C. Thornton, and C. Y. Wu. A Numerical Study of Die Filling Using a Coupled Discrete Element Method and Computational Fluid Dynamics. In *Proceedings of the EURO PM 2007, Volume 3, Toulouse, France*, pages 317–322, Shrewsbury, UK, 2007. European Powder Metallurgy Association.

[122] M. D. Riera, A. Istúriz, J. M. Prado, J. C. Cante, J. Oliver, and C. González. Experimental and Numerical Study of the Die Filling Stage in Powder Metallurgy. In *Proceedings of the EURO PM 2005, Volume 3, Prague, Czech Republic*, pages 339–344, Shrewsbury, UK, 2005. European Powder Metallurgy Association.

[123] G. Gustafsson and H.-Å. Häggblad. Simulation of Metal Powder Die Filling Processes Using Smoothed Particle Hydrodynamics Method. In *Proceedings of the EURO PM 2007, Volume 3, Toulouse, France*, pages 311–316, Shrewsbury, UK, 2007. European Powder Metallurgy Association.

[124] E. R. Rice and J. Tengzelius. Die filling characteristics of metal powders. *Powder Metall.*, 29(3):183–194, 1986.

[125] E. Hjortsberg and B. Bergquist. Filling induced density variations in metal powder. *Powder Metall.*, 45(2):146–153, 2002.

[126] I. C. Sinka, L. C. R. Schneider, and A. C. F. Cocks. Measurement of the flow properties of powders with special reference to die fill. *Int. J. Pharm.*, 280(1–2):27–38, 2004.

[127] C. Liu and S. R. Nagel. Sound in sand. *Phys. Rev. Lett.*, 68(15):2301–2304, 1992.

[128] L. R. Lawrence and J. K. Beddow. Some Effects of Vibration upon Powder Segregation during Die Filling. *Powder Technol.*, 2(2):125–130, 1968.

[129] P. M. Reis and T. Mullin. Granular Segregation as a Critical Phenomenon. *Phys. Rev. Lett.*, 89(24):244301, 2002.

[130] S. Merabia and I. Pagonabarraga. A mesoscopic model for (de)wetting. *Eur. Phys. J. E*, 20(2):209–214, 2006.

[131] B. Henrich, C. Cupelli, M. Moseler, and M. Santer. An adhesive DPD wall model for dynamic wetting. *Europhys. Lett.*, 80:60004, 2007.

[132] B. Weber, C. Bierwisch, R. Kübler, and G. Kleer. Investigation of the Sawing of Solar Silicon by Application of Wires of 100 μm Diameter. In *Proceedings of the 23rd European Photovoltaic Solar Energy Conference, Valencia, Spain*, pages 1285–1288, Munich, Germany, 2008. WIP-Renewable Energies.

Danksagung

Mein Dank gilt Prof. Dr. Michael Moseler, meinem Doktorvater, für die Aufnahme in seine Gruppe, seine exzellente fachliche Betreuung sowie für viele freundliche und motivierende Worte.
Dr. Torsten Kraft danke ich für die Einbindung in spannende Projekte und die sehr gute Zusammenarbeit im Bereich der Pulvertechnologie.
Prof. Dr. Hermann Riedel und Prof. Dr. Peter Gumbsch möchte ich für vielfältige Anregungen und Hinweise auf wissenschaftlich hohem Niveau danken.
Lars Pastewka und Dr. Andreas Wonisch danke ich für unzählige fachliche Diskussionen und eine ausgesprochen angenehme Bürogemeinschaft in unserem Elfenbeinturmzimmer.
Dank an Emeline Bessard und Yakiv Brontfeyn für ihre unentbehrliche Unterstützung bei den experimentellen Arbeiten.
Bei Bianca Lang, Dr. Manfred Nebelung, Bernd Weber, Dr. Rainer Kübler, Dr. Günter Kleer, Dr. Mark Santer, Dr. Björn Henrich und Thomas Steinert möchte ich mich für die bereichernde Zusammenarbeit in verschiedenen Projekten bedanken.
Mein Dank gilt allen Mitarbeitern am Fraunhofer-Institut für Werkstoffmechanik für die inspirierende Arbeitsatmosphäre. Insbesondere möchte ich Nadine Kuder und Helgard Nisalke für die reibungslose Administration, Jan Hülsberg und Franz Doll für den engagierten IT-Support und den lieben Kollegen aus der M8 für eine schöne Zeit in vielerlei Hinsicht danken.
Von ganzem Herzen danke ich meiner Familie für ihre Liebe und Unterstützung.